8-10-2021

Exploring Interferometric Realms: Modeling and Imaging of Stars, and Optical Test Bench Simulations

Arturo Omar Martinez
Georgia State University

Exploring Interferometric Realms: Modeling and Imaging of Stars, and Optical Test Bench Simulations

by

Arturo Omar Martinez

Under the Direction of Fabien R. Baron, PhD

A Dissertation Submitted in Partial Fulfillment of the Requirements of

Doctor of Philosophy

in the College of Arts and Sciences

Georgia State University

2021

ABSTRACT

High-resolution interferometric imaging is currently the most accurate technique to image the surfaces of stars. However, optical interferometric imaging is a difficult ill-posed problem where a handful of imaging codes are able to find a solution, especially in three dimensions. We present the development of a 3D interferometric image reconstruction code, which has the capabilities to model/image the surfaces of spherical, spheroid, and Roche objects. We apply our open source code to two different data sets. The first application is for the RS CVn variable, λ Andromedae, using archival interferometric data from the CHARA Array obtained with the MIRC instrument at two different epochs to better understand the evolution of its surface features. We are able to obtain precise measurements of its physical parameters as well as images of its surface detailing large-scale magnetic spots. Our results show that the reconstructed images of λ Andromedae have starspots that seem to favor certain northern latitudes with very minimal to no spot activity in the southern latitudes, indicative of a non-solar dynamo. The second application is for the rapidly rotating star, Alderamin, with data obtained from CHARA with the MIRC-X instrument to continue unveiling the complexities of the internal mechanisms of rapid rotation. We present our preliminary imaging results, which show a slightly lower angular velocity compared to previous works along with a weak limb-darkening. These new results provide a quantitative result for limb-darkening for rapid rotators, which has not been explored before. In addition to our rapid rotator imaging, we integrate new a gravity darkening law, which will serve as improved initial parameter estimates for future imaging campaigns. To complement future imaging campaigns, we present preliminary results for a novel multi-beam atmospheric turbulence simulator that can be used to study free-space beam propagation. This latter project will serve as the groundwork for having movable telescopes at interferometric arrays, such as the CHARA Array, which will provide more (u,v) coverage and ultimately improve the quality of interferometric

imaging. We use our simulator to investigate beam combination under severe ground layer turbulence conditions.

INDEX WORDS: Aperture synthesis, Astronomy software, High angular resolution, Long baseline interferometry, Oblate stars, Observational astronomy, Optical interferometry, RS Canum Venaticorum variable stars, Starspots

Exploring Interferometric Realms: Modeling and Imaging of Stars, and Optical Test Bench Simulations

by

Arturo Omar Martinez

Committee Chair:	Fabien R. Baron
Committee:	Stuart M. Jefferies
	Russel White
	Gerard van Belle

Electronic Version Approved:

Office of Graduate Studies

College of Arts and Sciences

Georgia State University

August 2021

DEDICATION

To my loving mother Octaviana Rodriguez and my caring sister Patricia Villanueva.

ACKNOWLEDGEMENTS

I believe that in life, you should always put effort into any given task. However, there are times where you may end up at roadblocks, and no matter how hard you try, you may not be able to get past them; it is in these times where you should ask for assistance, regardless of how enormous or minuscule it should be. For these reasons, I would like to thank many people that have guided me throughout the years leading up to my PhD (my undergraduate years) and the PhD itself. If it were not for those individuals assisting me during those undergraduate years, I don't think I would have been where I am today.

First and foremost, I would like to give my deepest gratitude to my primary advisor Prof. Fabien Baron for his assistance and support throughout all of my graduate studies. He encouraged me to tackle problems that others would find intimidatingly difficult and offered interesting avenues for research projects. I would also like to thank my secondary advisor Prof. Stuart Jefferies who offered the same assistance and support while contemporaneously offering challenging perspectives. Throughout my PhD, Fabien and Stuart's constructive criticisms encouraged me to keep moving forward, compelled me to continue refining my skills, and fix any of my weaknesses as a graduate student. I also thank Prof. Russel White for his insightful comments regarding both the λ Andromedae and rapid rotator work. I thank my outside committee member Dr. Gerard van Belle for his assistance in rapid rotator work and collaboration with contemporaneous imaging at NPOI.

I want to thank my research group for making our group a welcoming place for discussions and debates. I have to thank Dr. Ryan Norris for all of the assistance he has given me throughout his time at Georgia State University (GSU). I remember his patience when teaching me how to use the MIRC-X instrument at the CHARA Array, which was critical for this work. I also thank Matt Anderson for the countless times he assisted me on trips to CHARA and provided encouraging advice during observations. Another thank you goes to Caleb Abbott, who made the optics lab an entertaining and fantastic place to work.

Parts of this dissertation work would not be remotely possible if it were not for the CHARA Array staff. I am grateful for telescope operators Dr. Chris Farrington, Olli Majoinen, and Norm Vargas, who assisted in obtaining data that would be used for scientific analysis within this manuscript. I am also thankful to Dr. Gail Schaefer for her assistance in operating MIRC-X. I am grateful to the rest of the CHARA staff (Dr. Theo ten Brummelaar, Steve Golden, Drs. Judit and Laszlo Sturmann, Dr. Nils Turner, Larry Webster, and Craig Woods) and their efforts to keep the Array up and running. I would also like to thank the entire MIRC-X team, especially Profs. John Monnier and Stefan Kraus, for their assistance in maintaining and upgrading the MIRC-X instrument, which made this work possible.

A special thank you goes to my former research advisor Prof. Eric Sandquist from San Diego State University (SDSU). When I initially started my undergraduate studies at SDSU, I was unsure how to become an astronomer or what it meant to be a scientist. I often struggled with asking questions, whether it would be in class or during office hours; this problem stemmed from my childhood since my father never liked questions being asked in his household. Prof. Sandquist taught me that critiquing one's work and understanding the fundamentals was beneficial for progress. His assistance and encouragement throughout my time at SDSU have helped me improve as a student and person. He was always attentive whenever I had personal issues that barred me from progressing in my academic life.

I thank the Cal-Bridge community, especially the director of Cal-Bridge Prof. Alexander Rudolph, for their assistance during my last year as an undergraduate student and one year as a graduate student at SDSU. Cal-Bridge gave me the academic support to learn how to become a better graduate student and the financial support not to have to work grueling hours, which allowed me to focus on my classes. Cal-Bridge also provided me with two academic advisors, Profs. Eric Sandquist and Adam Burgasser, who often offered advice on how I could improve academically. Without the support and resources of the Cal-Bridge program, getting accepted into a PhD program would have been extremely difficult.

A thank you goes out to my CAMPARE mentor, Prof. Ian Crossfield, who provided me with an exciting summer research project. He offered countless opportunities to present my summer research and, in turn, allowed me to investigate any future research projects (which eventually led to my current research at GSU).

I especially cherish my close family and friends since they have always offered words of encouragement and hope that I would accomplish my goals. I thank my mom, who has always been by my side, and has provided the assistance and push I needed to continue moving forward despite all of the hardships we went through. I must also thank my sister Patricia, who has been extremely supportive of my goals and always offered me a warm welcome whenever I went back home. I thank my close childhood friends (Matthew Daum, Karl Fulgencio, Sebastian Madrid, Kevin Sahagun, Ninveh Shamoon, Traviaun Simpson, and Ivan Suarez) who not only been encouraging but have constantly made some of those tough days just a little bit better. I also acknowledge my former high school calculus teacher, Mr. Clint McDonald, who has offered me academic and personal advice throughout my high school and undergraduate years.

I thank my friends and colleagues at SDSU (especially Alexis Ceja, Daniel Lapuz, David Jaimes, Eric McLaughlin, and Hannah Rotter) who made my time there a pleasant experience, despite some of the struggles we went through.

I finally would like to thank my karate martial arts instructor Mark R. Moeller Shihan. Training with him has allowed me to view life from a different perspective. I have learned from Moeller Shihan that karate-do can be an integral part of one's life and is not limited to self-defense. Both my PhD studies and karate-do training have complemented each other in a few ways. The constant mistakes and "failures" throughout my PhD has made it easier to continue my countless hours of repetition in karate, thus improving my form. On the other hand, my karate-do training has further emphasized that through hard work and patience, I can get closer to achieving my goals (whether it is a martial art, personal life, or academic goal). I also thank all the senior karate instructors (Chip Abernathy, Mark Snepp, Mark

Taylor, and Kent Watkins) and my Internal Power/Aikido instructor Larry Feldman Sensei who helped me improve as a martial artist.

I thank GSU's Second Century Initiative (2CI) Doctoral Fellowship for their financial support throughout my PhD. We acknowledge support from NSF Grant No. AST-1616483 and AST-1814777. The Air Force Office of Scientific Research funded this work through contracts FA9550-18-1-0411 and FA9550-14-1-0178. This work is based upon observations obtained with the Georgia State University Center for High Angular Resolution Astronomy Array at Mount Wilson Observatory. The CHARA Array is supported by the National Science Foundation under Grant No. AST-1636624 and AST-1715788. Institutional support has been provided from the GSU College of Arts and Sciences and the GSU Office of the Vice President for Research and Economic Development. MIRC-X received funding from the European Research Council (ERC) under the European Union's Horizon 2020 research and innovation program (Grant No. 639889).

I found that living my life by the following quote has made any struggle or problem, no matter how big or small, just a little more manageable. I have applied it to my studies as a graduate student and will continue applying it for the rest of my life.

> *Start each day with a task completed. Find someone to help you through life. Respect everyone. Know that life is not fair and that you will fail often. But if take you take some risks, step up when the times are the toughest, face down the bullies, lift up the downtrodden and never, ever give up - if you do these things, the next generation and the generations that follow will live in a world far better than the one we have today.*
>
> -Naval Admiral William H. McRaven

Table of Contents

List of Tables

List of Figures

List of Abbreviations

ADMM	Alternating Direction Method of Multipliers
AU	Astronomical Unit
Ca	calcium
CHARA	Center for High Angular Resolution Astronomy
cm	centimeter
dec	declination
DM	deformable mirror
ESTER	Evolution STEllaire en Rotation
GPU	graphics processing unit
Mg	magnesium
MCMC	Markov chain Monte Carlo
MIRC	Michigan InfraRed Combiner
MIRC-X	Michigan InfraRed Combiner, Exeter
μm	micron
mas	milliarcsecond
mm	millimeter
NLopt	nonlinear optimization
nm	nanometers
NPOI	Navy Precision Optical Interferometer
OITOOLS	Optical Interferometry Tools
PoP	Pipes of Pan
PSF	point spread function
RA	right ascension
ROTIR	ROTational Image Reconstruction
RMS	root mean square
RS CVn	RS Canum Venaticorum

SIMTOI SImulation and Modeling Tool for Optical Inteferometry

SLM spatial light modulator

SURFING SURFace imagING

VMLMB Variable Metric Limited Memory with Bounds

VLTI Very Large Telescope Interferometer

WFS wavefront sensor

Chapter 1
INTRODUCTION

1.1 The Beginnings of Interferometry

The beginning of interferometry can be traced back to the origin of wave theory in the 17th century and the eventual introduction of interference of waves in the 19th century. The concept of a wavelength began with experiments done by Robert Hooke (among others, such as Francesco M. Grimaldi and Ignace-Gaston Pardies). Hooke speculated that light traveled in waves akin to that of water when perturbed and published these thoughts in his book *Micrographia* in 1665. He was the first to discover thin-film interference and its diffraction properties, and in 1672 noted that these vibrations of light are perpendicular to the direction of propagation.

A few years later, Christiaan Huygens wrote a mathematical interpretation of these vibrations in his book *Treatise on Light* in 1690. Additionally, he proposed that these light waves traveled through a medium called an "aether" that filled the void of space. The Huygens' principle was contrived and described that light consisted of an aggregate of spherical wavelets. As light is propagated, the secondary waves can then be made up of an aggregate of these individual first wavelets. While this theory formed the basis for understanding wave propagation, diffraction, and reflection, it was not widely accepted at the time. The most dominantly accepted and recognized theory during the late 17th century and early 18th century was the corpuscular theory of light and was backed by famous scientists like Isaac Newton. Newton explained within his book *Opticks* in 1704 that light was comprised of particles with internal vibrations instead of spherical wavelets, and Newton's reverence within the natural sciences led to the corpuscular theory being the leading view until the experiments of Thomas Young proved otherwise.

1.1.1 *The First Experiments Obtaining Interference Patterns*

In 1803, Young presented the first evidence of wave interference by passing sunlight through a pinhole and splitting the light coming from that pinhole with a narrow card (around 0.85 mm wide). The split beams of light landed on a screen and started overlapping against one another, creating bands of bright and dark patches of light or interference fringes. Young noted that when one beam of light was blocked, the places where the dark bands used to be disappeared, and the intensity on the screen was completely uniform. When he slowly added in the intensity of the second beam, the intensity of the dark bands was reduced while the intensity of the bright bands increased, thus increasing the contrast of the fringes. Young later updated his experiment to the now-famous double-slit experiment that was published in 1807 (where two pinholes or slits were used to split light and obtain fringes), which laid the groundwork for the acceptance of light wave theory.

Young's experiment was followed by many other interferometric experiments, such as Augustin-Jean Fresnel, who further refined the nature of light diffraction effects in 1818. The application of modern interferometers first started with Armand Hippolyte L. Fizeau and his proposition to test the aether theory. In 1851, Fizeau measured the speed of light and while doing so he concluded that there was indeed a drag across this aether (Fizeau 1868). In addition, Fizeau was the first to suggest that interferometers could be the instruments that could one day measure the angular diameters of stellar objects (Vaughan 1967). In 1881, Albert A. Michelson constructed his own interferometer to prove the movement of the aether drag. While his first instrument failed to make any discernible measurements of aether drag, the Michelson interferometer design proved to be useful for getting more accurate measurements of the speed of light. Later in 1887, Michelson, in collaboration with Edward W. Morley, improved upon Michelson's original 1881 interferometric design and found no evidence of the aether. While Michelson's interferometric experiments tested the aether theory while consequently obtaining accurate measurements for the speed of light, it also laid the foundation for obtaining stellar interferometric measurements.

In Michelson's 1891 paper, perhaps following the idea proposed by Fizeau a few decades before, Michelson explained that one could obtain the angular diameter of a single star or the angular separation of binary systems. The concept for obtaining such measurements was that if one had a large objective, two smaller portions of the objective at opposite sides would be used as apertures, and the light would combine at the focus. By increasing the distance between the two apertures until the fringes disappeared, one could then measure the angular diameter or separation of the source(s) since these aperture separations are directly related to the minimum fringe visibility (Michelson 1891a, 1920).

Michelson tested the method he proposed in 1891 of using slits as apertures to successfully measure the diameter of the Galilean moons (Michelson 1891b,c). While the method Michelson proposed turned out to be quite accurate, the angular diameters of stars are much smaller than that of the Galilean moons, and thus a different approach was needed. Michelson decided to make a new interferometer by using mirrors, instead of slits, at the 100 inch Hooker telescope at Mount Wilson Observatory. This new interferometer consisted of four mirrors on a 20-foot steel plate placed above the telescope. Michelson and Francis G. Pease used this new design to measure the angular diameter of Betelgeuse and calculated it to be 47 mas (Michelson & Pease 1921), and thus recorded the first angular diameter measurement of a star.

1.1.2 *The Diffraction Limit of Telescopes and Interferometers*

Without the use of interferometry, Michelson would have had a difficult time building a single mirror telescope to resolve the angular diameter of Betelgeuse, especially with the technology of the early 1920s. A telescope's two limiting factors to measure the angular diameter of an object are to collect enough light into your capturing device and resolve the source. Taking a step back from interferometry, the requirements to resolve an object with a single telescope comes from the Rayleigh criterion. This criterion is derived from an Airy disk, where the intensity of the light distribution for an Airy disk is in the form of

$$I(\theta) = I_0 \left(\frac{2J_1(\frac{2\pi}{\lambda} R \sin\theta)}{\frac{2\pi}{\lambda} R \sin\theta} \right)^2 = I_0 \left(\frac{2J_1(x)}{x} \right)^2 \tag{1.1}$$

where I_0 is the maximum intensity of the pattern at the Airy disk center, J_1 is the Bessel function of the first kind of order one, λ is the observed wavelength, R is the radius of the observing aperture, θ is the angle of the observed object (i.e., the angle made from a line between the circular aperture center and the observed object's outer most radius, and the line between aperture center and the object's center), and $x = \frac{2\pi R}{\lambda} \sin\theta$. If we look at the first zero of the $J_1(x)$, then $x \approx 3.8317$ and we get

$$\frac{2\pi R}{\lambda} \sin\theta \approx 3.8317. \tag{1.2}$$

Given that astronomical objects small angular sizes in the sky, we can apply the small angle approximation to Equation 1.2 to ultimately get the Rayleigh criterion of

$$\theta_{\text{rad}} \approx 1.22 \frac{\lambda}{D} \tag{1.3}$$

where θ_{rad} is the angular diameter of the object in radians, λ is the wavelength of the light being collected in meters, and D is the diameter of the mirror or lens in meters.

Let us look back at Michelson and his studies from Betelgeuse. We can deduce that if interferometry were not used at that time, Michelson would have needed to build a telescope with an aperture of approximately 3 meters in diameter (assuming the middle of the visible spectrum of 550 nm). If we take Equation 1.1 and modify it such that we use the distance between two apertures for an interferometer instead of the radius of one observing aperture for a single telescope, then it becomes

$$I(\theta) = I_0 \left(\frac{2J_1(\frac{2\pi}{\lambda} B \sin\theta)}{\frac{2\pi}{\lambda} B \sin\theta} \right)^2 \tag{1.4}$$

where B is the baseline or the distance between two apertures. The resolution of an interferometer is ultimately

$$\theta_{\rm rad} \approx 1.22 \frac{\lambda}{2B}. \tag{1.5}$$

Instead, Michelson did his calculations with a 20-foot (∼6 meter) baseline interferometer to be able and resolve Betelgeuse.

1.1.3 *Theory of Interferometry*

Interferometric experiments would not have been possible if it were not for the nature of each respective light source. Regarding the discussion of light propagation and its observed properties, a few terms must be defined for the discussion of wavelengths. A wavelength is defined as the length between an arbitrary origin in a wave and the point where the slope and concavity of the wave is the same as the origin (e.g., the length from one peak to the next peak of a wave). The amplitude of each wavelength is characterized by the height of each wave from the rest position, the phase is a quantity that defines the behavior of a wave where the origin is any arbitrary point in time (usually the midpoint between the peak and the trough), and the frequency is defined as the number of times that the wave oscillates within a given unit time.

Light must ideally be coherent in order to interfere; however, that may not always be possible. In order for light to be coherent to each other, it must have the same phase in respect to each wave in the same wavefront. Astronomical objects originate as incoherent sources, even when light is coming from the same object, but their large distances from Earth turn them partially coherent. This idea of partial coherence originates from the van Cittert-Zernike theorem (van Cittert 1934; Zernike 1938) named after Pieter H. van Cittert and Frits Zernike, which states that the Fourier transform of the intensity distribution of a distant, incoherent object is equivalent to the angular intensity distribution of the same object (Labeyrie et al. 2006).

How exactly did van Cittert and Zernike prove that incoherent sources such as astronomical objects could provide information about objects' angular size? We will follow the proof written in Labeyrie et al. (2006) in order to derive the van Cittert-Zernike theorem. Let us consider light arriving from a distant astronomical object to a given telescope as presented in Figure 1.1 (which is adapted from a similar design within Labeyrie et al. 2006). The telescope observing the object has its own z-axis which is defined along its optical axis with object located within a close region to this z-axis. The intensity of the incoming light from the source can be defined as $I = \langle |A(l,m,n)|^2 \rangle_t$, where A is the amplitude of the optical field which originates from the source and $\vec{l} \equiv (l,m,n)$ are the sky coordinates of the source. Taking advantage of the fact that the source is close to the z-axis, then we can approximate that $l = \sin\theta_x \approx \theta_x$ and $m = \sin\theta_y \approx \theta_y$ (based on small angle approximations) where the (x,y,z) are the coordinates of the telescope's optical axis. When $z = 0$, the optical field is $A(l,m)e^{i(\omega t + k_0 \vec{l}\cdot\mathbf{r})}\mathrm{d}l\mathrm{d}m$ where $\omega = 2\pi c/\lambda$ is the circular frequency (and c is the speed of light), t is time, $-\vec{l}$ is the direction of light travel from the source with its corresponding wavevector $-k_0\vec{l}$ (being that $k_0 = 2\pi/\lambda$ is a wavenumber), and $\mathbf{r} = (x,y,z)$.

If we integrate the optical field, then we get

$$E(k_0 x, k_0 y) = e^{i\omega t} \iint A(l,m) e^{i(k_0 x + k_0 y)} \mathrm{d}l\mathrm{d}m \tag{1.6}$$

and if we do the two-dimensional Fourier integral of Equation 1.6, we arrive at

$$E(k_0 x, k_0 y) = e^{i\omega t} a(-k_0 x, -k_0 y). \tag{1.7}$$

If we define the spatial coherence function in the ground plane (x,y) as the time-averaged cross correlation of the optical field

$$\gamma(k_0\mathbf{r}) = \langle E(k_0\mathbf{r}) \star E^*(-k_0\mathbf{r}) \rangle_t = \langle a(-k_0\mathbf{r}) \star a^*(k_0\mathbf{r}) \rangle_t \tag{1.8}$$

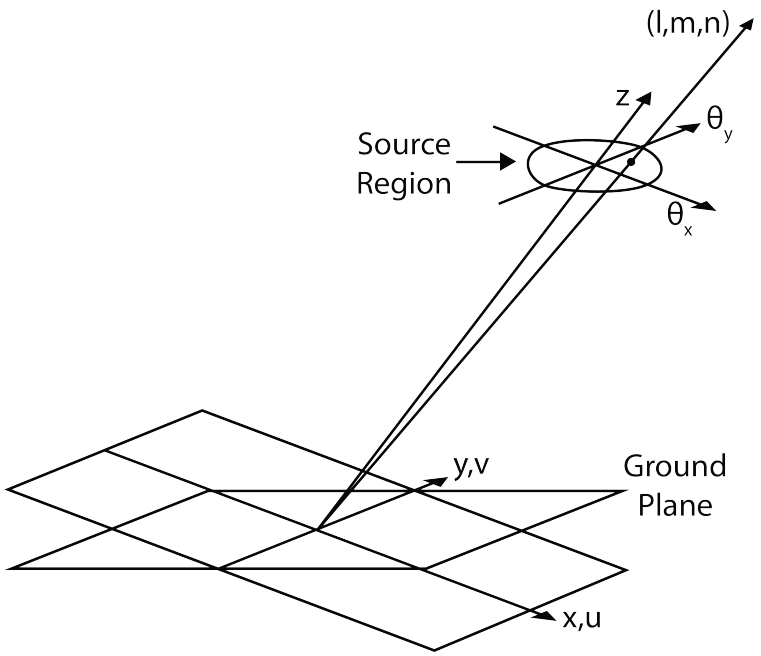

Figure 1.1 Geometry used in the proof of the Van Cittert-Zernike theorem. This figure has a similar design and was originally adapted from Labeyrie et al. (2006).

where the $e^{i\omega t}$ term cancels out because of the multiplication with the complex conjugate. We finally arrive at the Fourier transform of Equation 1.8 as

$$\Gamma(l,m) = \langle A(l,m) \cdot A^*(l,m) \rangle_t = \langle |A(l,m)|^2 \rangle_t = I(l,m). \tag{1.9}$$

thus proving the van Cittert-Zernike theorem (Labeyrie et al. 2006).

If we apply this theorem to Michelson's experiment, we can directly compare that the visibility of an interference fringe is directly related to the spatial coherence function (following another proof within Labeyrie et al. 2006). Let's start with light coming from two pinholes (similar to that of Young's experiment) where the corresponding mean intensities of each pinhole are A_1^2 and A_2^2 and the optical wave fields $E(\mathbf{r})$ are normalized. The coherence function now becomes

$$\gamma(\mathbf{r}_1, \mathbf{r_2}) = \frac{\langle A_1 E(\mathbf{r}_1) \cdot A_2 E(\mathbf{r}_2) \rangle}{A_1 A_2} = \langle E(\mathbf{r}_1) E(\mathbf{r}_2) \rangle. \tag{1.10}$$

These interference patterns result from the superposition between the optical fields coming from each respective pinhole with a given phase difference δ. Therefore, the instantaneous intensity of the interference pattern is

$$I(\delta) = |A_1 E(\mathbf{r}_1) + A_2 E(\mathbf{r}_2) e^{i\delta}|^2 \tag{1.11}$$

$$= A_1^2 |E(\mathbf{r}_1)|^2 + A_2^2 |E(\mathbf{r}_2)|^2 + A_1 A_2 \left[|E(\mathbf{r}_1) E^*(\mathbf{r}_2)| e^{i\delta} + |E^*(\mathbf{r}_1) E(\mathbf{r}_2)| e^{-i\delta} \right] \tag{1.12}$$

and by taking the time averages, the intensity becomes

$$I(\delta) = A_1^2 + A_2^2 + A_1 A_2 \left[\gamma e^{i\delta} + \gamma^* e^{-i\delta} \right] \tag{1.13}$$

$$= A_1^2 + A_2^2 + 2A_1 A_2 |\gamma(\mathbf{r}_1, \mathbf{r}_2)| \cos(\delta + \Delta) \tag{1.14}$$

where Δ is the position of the central fringe (Labeyrie et al. 2006).

In Michelson's experiments (Michelson 1891a), he defined that the visibility V as a function of the relative intensities from the contrast of the fringes as

$$V = \frac{I_{\max} - I_{\min}}{I_{\max} + I_{\min}} = \frac{\text{Fringe amplitude}}{\text{Average intensity}}. \tag{1.15}$$

If we now substitute in Equation 1.14 in Michelson's definition of a visibility, this would become

$$V = \frac{2A_1 A_2}{A_1^2 + A_2^2} \cdot |\gamma(\mathbf{r}_1, \mathbf{r}_2)|. \tag{1.16}$$

This states that by measuring the visibility and the phase of the fringes, one can understand the degree of coherence, which in turn will provide information about the angular size of the source for astronomical objects (Labeyrie et al. 2006).

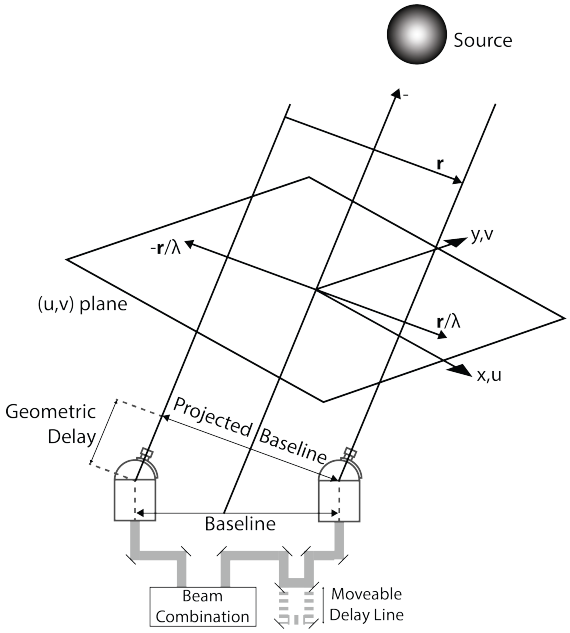

Figure 1.2 A model of a simple interferometer depicting only two telescopes measuring the intensity from a source. This figure was adapted from and has similar designs to that in Monnier (2003) and Labeyrie et al. (2006).

1.1.4 *Modern Observables in Interferometry*

Modern interferometers are no longer restricted to the technology from Michelson's era. Instead of mounting two mirrors on a single large telescope, astronomers are now able to construct facilities containing multiple telescopes with baselines ranging from a few meters to kilometers. Specifically for optical interferometry (here, optical means the use of optics within homodyne interferometry, not the optical wavelength regime), there are delay lines to compensate for the fact that light may not get to each telescope at exactly the same time, as shown in Figure 1.2. Since the light distribution of the source is measured by the coherence function, which is in Fourier space, the separation of the telescopes in the plane orthogonal to the direction of the source $\mathbf{r} = (l, m)$ is typically written in Fourier space as $\mathbf{u} = (u, v) = r/\lambda$, where λ is the wavelength and is the normalization term. Therefore, an interferometer samples part of this (u, v) plane.

While obtaining visibility measurements is useful for measuring angular sizes of objects, reconstructing an image of an object requires more information than just visibilities. To make an image requires knowledge of the atmosphere to correct for any corruption caused by atmospheric turbulence. The turbulence in Earth's atmosphere presents a large source of issues with imaging. If one were to observe a single star, its light would reach the top of Earth's atmosphere as a plane wave. This light gets refracted by different temperature cells within the atmosphere. By the time the star light reaches the ground layer, it will be refracted numerous times by this turbulence, dispersing the light and causing it to no longer travel as a plane wave. This will degrade the image quality and result in resolutions worse than the diffraction limit. A measure of how much atmospheric turbulence there is in a given image can be defined by the Fried coherence length (designated by r_0; Fried 1965, 1966). In the case of binary systems that are relatively close to each other in terms of angular distance, the light from both stars reaches the top of Earth's atmosphere as a plane wave. However, these plane waves may be too close together such that each wave will go through the same atmospheric patch and, by the time the light reaches a telescope, the binary system will seem like light is coming from a single source (Roddier 1988).

The Fried parameter can vary based on the nature of the atmosphere and is often represented by the Kolmogorov theory of turbulence (Kolmogorov 1961; Tatarskii 1961). The main two dependencies of how r_0 is calculated are based on the turbulence strength, the viewing angle of the target with respect to zenith, and wavelength. These astronomical seeing conditions, or the amount of turbulent airflow in the atmosphere, can be described by generating a profile of the turbulence strength as a function of altitude (or height) in the atmosphere at a given observing site, otherwise known as the C_n^2 profile. The Hufnagel-Valley model (Mohr et al. 2010) is often used to describe the C_n^2 profile, given by the following

$$C_n^2(h) = A \exp\left(-\frac{h}{H_A}\right) + B \exp\left(-\frac{h}{H_B}\right) + h^{10} C \exp\left(-\frac{h}{H_C}\right) \tag{1.17}$$

where h is the height above the ground. A represents the strength of the ground layer of the atmosphere and H_A is the height of its $1/e$ decay. B and H_B are similarly defined for the turbulence in the troposphere, while C and H_C are related to the turbulence peak located at the tropopause. Once a C_n^2 profile has been measured or estimated, then we can finally determine how the coherence length is calculated by using

$$r_0(\lambda) = \left[0.423\ k^2(\cos\zeta)^{-1} \int_0^\infty C_n^2(h)\mathrm{d}h\right]^{-3/5} \tag{1.18}$$

where $k = 2\pi/\lambda$ and ζ is the viewing angle with respect to zenith. Therefore, the coherence length has a $r_0 \propto \lambda^{6/5}$ dependence on wavelength.

Besides the Fried parameter r_0, another important parameter for obtaining valuable interferometric data is the coherence time, τ_0. Using the coherence time essentially assumes a frozen atmosphere (known as Taylor's hypothesis; Taylor 1938). This frozen atmospheric model assumes that the atmospheric density perturbations are constant over a given time that it would take for the pocket of air to travel along a given aperture with the local wind. The coherence time along with the Greenwood time constant can be calculated by using the following

$$\tau_0(\lambda) = 0.314\ r_0/\overline{V} \tag{1.19}$$

where $\overline{V}$ is the mean wind speed given by

$$\overline{V} = \left[\frac{\int C_n^2(h)\ |V(h)|^{5/3}\mathrm{d}h}{\int C_n^2(h)\mathrm{d}h}\right]^{3/5} \tag{1.20}$$

where $V(h)$ is the wind velocity at a specific height in the atmosphere. Both the coherence length and coherence time are crucial since they limit the size of the apertures and integration time for an interferometer, respectively (Monnier 2003).

However, you can negate the atmospheric effects by observing a quantity called the triple product or the bispectrum. By combining the complex visibilities from two different

telescopes, one can express the observed visibility as

$$\widetilde{V}_{12}^{\rm obs} = |G_1||G_2|\widetilde{V}_{12}^{\rm true} \exp\left[i(\Phi_{12}^{\rm obs})\right] \tag{1.21}$$

where 1 and 2 is telescope one and two (respectively), G is the complex gain and is used as a scale factor based on telescope degradation effects (e.g., mirror reflectivity, detector sensitivity, local scintillation) for any given telescope, $\widetilde{V}^{\rm true}$ is the true visibility from the object, Φ is the phase that holds all of the information about the phase shifts from the telescope pair, the beam, the atmosphere (e.g., changing optical path lengths based from a thermal expansion or contraction, atmospheric turbulence conditions above the telescope, or the beam path), and the object itself (Monnier et al. 2007). The phase can be further expanded into

$$\Phi_{12}^{\rm obs} = \Phi_{12}^{\rm true} + \epsilon_1 - \epsilon_2 \tag{1.22}$$

where $\Phi_{12}^{\rm true}$ is the intrinsic phase from the astronomical source measured by two telescopes, and the $\epsilon_1 - \epsilon_2$ are the phase shift errors that come from telescope, beam, or atmosphere (Monnier 2003; Labeyrie et al. 2006; Monnier et al. 2007; Buscher & Longair 2015).

One can negate atmospheric, beam, and telescope effects by introducing a concept first bought to interferometry in the radio by Jennison (1958) called closure phase. This was done to compensate for inadequate phase stability for early VLBI radio work. The idea to apply the use of closure phases to shorter wavelengths was first thought up by Rogstad (1968) but it took a few years before this could be applied in practice (Baldwin et al. 1986; Haniff et al. 1987; Readhead et al. 1988). By adding the phases between three different telescopes on a closed triangle, one is left with just the sum of the intrinsic phases of the source (i.e., the closure phase) shown by

$$\Phi_{12}^{\rm obs} + \Phi_{23}^{\rm obs} + \Phi_{31}^{\rm obs} = \Phi_{12}^{\rm true} + \epsilon_1 - \epsilon_2 + \Phi_{23}^{\rm true} + \epsilon_2 - \epsilon_3 + \Phi_{31}^{\rm true} + \epsilon_3 - \epsilon_1 \tag{1.23}$$

$$= \Phi_{12}^{\rm true} + \Phi_{23}^{\rm true} + \Phi_{31}^{\rm true}. \tag{1.24}$$

Hence, the atmospheric phase contributions have canceled out, so the measured closure phase it equivalent to the true closure phase. However, the closure phase is only part of the quantity that can be obtained from a closed triangle. By taking Equation 1.21 and multiplying them by each baseline pair within the triangle, we arrive at

$$\widetilde{V}_{12}^{\rm obs}\widetilde{V}_{23}^{\rm obs}\widetilde{V}_{31}^{\rm obs} = |G_1||G_2|\widetilde{V}_{12}^{\rm true}e^{i(\Phi_{12}^{\rm obs})}|G_2||G_3|\widetilde{V}_{23}^{\rm true}e^{i(\Phi_{23}^{\rm obs})}|G_3||G_1|\widetilde{V}_{31}^{\rm true}e^{i(\Phi_{31}^{\rm obs})} \tag{1.25}$$

$$= |G_1|^2|G_2|^2|G_3|^2\widetilde{V}_{12}^{\rm true}\widetilde{V}_{23}^{\rm true}\widetilde{V}_{31}^{\rm true}\exp\left[i(\Phi_{12}^{\rm obs}+\Phi_{23}^{\rm obs}+\Phi_{31}^{\rm obs})\right] \tag{1.26}$$

and using Equation 1.24, we can define the so-called triple product or bispectrum (Monnier et al. 2007) as

$$\widetilde{B}_{123} = \widetilde{V}_{12}^{\rm obs}\widetilde{V}_{23}^{\rm obs}\widetilde{V}_{31}^{\rm obs} \tag{1.27}$$

$$= |G_1|^2|G_2|^2|G_3|^2\widetilde{V}_{12}^{\rm true}\widetilde{V}_{23}^{\rm true}\widetilde{V}_{31}^{\rm true}\exp\left[i(\Phi_{12}^{\rm true}+\Phi_{23}^{\rm true}+\Phi_{31}^{\rm true})\right]. \tag{1.28}$$

Another quantity called the closure amplitude can be used to correct for the gain from each telescope; however other calibrations in optical interferometry are usually employed as closure amplitudes require at least four telescopes for accurate measurements (e.g., see Chael et al. 2018).

The bispectrum provides two important quantities for imaging: bispectrum phase and bispectrum amplitude, or as it is more commonly known as the (previously mentioned) closure phase and triple amplitude. To extract the closure phase or the triple amplitude from the bispectrum, one can simply take the phase and modulus of the bispectrum to get the respective quantities. While phase information is recovered using the bispectrum, the total coherence function (Equation 1.8) cannot be fully recovered since interferometers only sample part of the (u, v) plane. Unless a large aperture is constructed to fill the area made by a baseline pair of telescopes, the phase information will only be partially recovered depending on the number of telescopes, N. The number of independent closure phases is also dependent

on N and can be given by $\frac{(N-1)(N-2)}{2}$, with the fraction of the phase information recovered being $\frac{N-2}{2}$ (Monnier et al. 2007).

The closure phases calculated from the bispectrum provide information about the brightness distribution of the source. For an object that has symmetric intensity, the corresponding closure phases would be either 0 or ± 180 degrees. Therefore, any deviation from 0 or ± 180 degrees is an indication that the brightness distribution from the source is not completely uniform. Even though the visibility is measured, the squared visibility $|V|^2$, which is the square modulus of the visibility, is usually used for analysis. For a star, the first lobe of the squared visibility gives information about the angular size of the star, the second lobe gives information about the limb-darkening (i.e., the intensity distribution from the center to the limb of the star), while the third and subsequent lobes provide information about smaller surface features. The combination of all three (squared visibilities, closure phases, triple amplitudes) is crucial for accurate interferometric imaging.

1.2 Interferometric Modeling and Imaging

In an ideal situation, all the spatial frequencies would be recovered in order to obtain an image since it would simply take an inverse Fourier transform to reconstruct the true image. However, this is not the case for interferometric observations since an interferometer only samples part of the (u, v) plane (Fourier plane). There are two major reasons why this cannot be done: the number of telescopes used during an observation limits the number of Fourier frequencies that can be obtained, and the data are corrupted by numerous factors (as described in Section 1.1.4). For adequate imaging, one would also need to sample low and high spatial frequencies as low frequencies detail the large scale structures of an image (e.g., the size of a star) while the high frequencies detail the finer details of an image (e.g., limb-darkening, starspots, oblateness). While imaging is a difficult problem as it is ill-posed, interferometric modeling of the source may be a slightly less daunting task.

1.2.1 *Interferometric Modeling*

In order to solve for a model of the source, we can use Bayesian statistics and follow the *maximum a posteriori* paradigm. There are various global and local minimization algorithms that are employed to solve for the best model that fits the data. The simplest method in determining the best fit model is by applying a grid search. While a grid search allows for a global search, this may require a large amount of computation time depending on the number of parameters that need solving. There are various modeling codes that are available for modeling (Baron 2020), however we will discuss one particular modeling code that is used in this work, SIMTOI (Kloppenborg & Baron 2012a,b; Kloppenborg et al. 2015).

The SImulation and Modeling Tool for Optical Interferometry (SIMTOI) is an interferometric modeling code that uses a GPU to render stars and their environments in a three-dimensional framework. In SIMTOI, the stellar intensity maps are represented as two-dimensional textures applied on top of orbiting/rotating three-dimensional stars. Once the scene is rendered, the GPU also powers the fast computation of interferometric observables. SIMTOI offers a large choice of global and local optimizers to solve *maximum a posteriori* or model selection problems. We ultimately use the MultiNest optimizer (Feroz & Hobson 2008; Feroz et al. 2009, 2019) to acquire the best models.

As a first approach to finding a solution from a global standpoint, the MultiNest optimizer can be seen one of the best methods to find a solution. While a wide variety of codes use Markov chain Monte Carlo (MCMC), it is limited by the fact that it does not sample the tail ends of distributions and does not provide an easy way to determine of the convergence of the algorithm. MultiNest has been shown to outperform other global optimization techniques, such as MCMC, by applying the Nested Sampling method (Skilling 2004, 2006; Sivia & Skilling 2006). In order to explain the nested sampling within MultiNest, we must first start with Bayes' theorem as written in Feroz et al. (2019):

$$\Pr\left(\Theta|\mathrm{D}, M\right) = \frac{\Pr\left(\mathrm{D}|\Theta, M\right)\Pr\left(\Theta|M\right)}{\Pr\left(\mathrm{D}|M\right)} \tag{1.29}$$

where Θ are a set of parameters, M is the model, D is the data, $\Pr(\Theta|\mathrm{D}, M) \equiv P(\Theta|\mathrm{D})$ is the posterior probability density of the model parameters, $\Pr(\mathrm{D}|\Theta, M) \equiv \mathcal{L}(\Theta)$ is the likelihood of the data, $\Pr(\Theta|M) \equiv \pi(\Theta)$ is the prior, and $\Pr(\mathrm{D}|M) \equiv \mathcal{Z}$ is the Bayesian evidence and the normalizing factor of the posterior. The Bayesian evidence can also be defined as

$$\mathcal{Z} = \int_{\Omega_\Theta} \mathcal{L}(\Theta)\pi(\Theta)\mathrm{d}\Theta. \tag{1.30}$$

Following the equations and explanation of the algorithm in Feroz et al. (2019), we can then turn the multidimensional integral from Equation 1.30, to a one dimensional integral. This one dimensional integral is represented as the survival function or otherwise known as the prior volume $X(\lambda)$, for $\mathcal{L}(\Theta)$, is

$$X(\lambda) = \int_{\{\Omega:\mathcal{L}(\Theta)>\lambda\}} \pi(\Theta)\mathrm{d}\Theta \tag{1.31}$$

where the integral spans over the region in parameter space within a given iso-likelihood contour, $\mathcal{L}(\Theta) = \lambda$. You can then rearrange the Bayesian evidence as

$$\mathcal{Z} = \int_0^\infty X(\lambda)\mathrm{d}\lambda \tag{1.32}$$

or if the likelihood is a continuous function, it can be further rearranged as (Chopin & Robert 2010)

$$\mathcal{Z} = \int_0^1 \mathcal{L}(X)\mathrm{d}X \tag{1.33}$$

$$\approx \hat{\mathcal{Z}} = \sum_{i=1}^{N} \mathcal{L}_i w_i \tag{1.34}$$

where $\mathcal{L}(X)$ is the inverse of $X(\lambda)$, w_i is the weight (for known $\mathcal{L}(X)$, the weight can be estimated as $w_i = \frac{1}{2}(X_i + X_{i+1})$ through the trapezoidal rule), and a given number of points N. The nested sampling algorithm is initialized by taking N live points from the prior and

the initial prior volume. At every successive iteration the point where the likelihood is the lowest $\mathcal{L}_i$ is then removed from the set and replaced with another point from the prior with the condition that the new likelihood point is higher than $\mathcal{L}_i$. The nested sampling algorithm is completed when the estimated evidence contribution $\Delta Z_i = \mathcal{L}_{\max} X_i$ (where $\mathcal{L}_{\max}$ is the maximum likelihood among the current set of live points) is less than a user-defined tolerance level (Feroz et al. 2019). One major problem with some nested sampling algorithms is that there is an exponential reduction in the sampling for increasing dimensionality.

The MultiNest algorithm built by Feroz & Hobson (2008) solves the higher dimensionality sampling issue by taking unbiased samples from a likelihood-constrained prior through an ellipsoidal rejection scheme. The live points are split within ellipsoids that could possibly be overlapping at certain points. At a given iteration, an ellipsoid l is chosen given a probability $p_l = V_l / V_{\text{tot}}$ where V_l is the volume of a particular ellipsoid and $V_{\text{tot}} = \sum_{l=1}^{L} V_l$ is the total volume of all the ellipsoids. A point is then selected from the ellipsoid, checked against the nested sampling constraint $\mathcal{L} > \mathcal{L}_i$ and if it's accepted, then the point is given a probability $1/q$ where q is the number of ellipsoids that the particular point belongs to. If the point is otherwise rejected, then the point is discarded from the ellipsoid (yet still saved for later calculations).

In order to make MultiNest fully efficient, Feroz et al. (2019) has also implemented the importance nested sampling algorithm (Cameron & Pettitt 2014). Importance nested sampling takes all points from MultiNest, regardless of whether it is rejected from the nested sampling constraint or not. A pseudo-importance sampling density can be formed as

$$g(\Theta) = \frac{1}{N_{\text{tot}}} \sum_{i=1}^{N_{\text{iter}}} \frac{n_i E_i(\Theta)}{V_{\text{tot,i}}} \tag{1.35}$$

where N_{iter} are the total number of iterations from MultiNest, n_i is the number of points collected at a specific i^{th} iteration, $N_{\text{tot}} = \sum_{i=1}^{N_{\text{iter}}} n_i$ is the total number of points from the start to the i^{th} iteration, $V_{\text{tot,i}}$ is the total volume of all the ellipsoids at the i^{th} iteration,

and $E_i(\Theta)$ is an indicator function that returns either 1 when Θ is within the ellipsoids or 0 if it is outside. The total volume of the ellipsoids for importance nested sampling can be estimated by

$$V_{\rm tot} \approx \hat{V}_{\rm tot} = \frac{M}{\sum_{m=1}^{M} q_m} \sum_{l=1}^{L} V_l \tag{1.36}$$

where M is a number of points taken from a specific ellipsoid given a probability of $V_l / \sum_{l=1}^{L} V_l$ and with q_m being the number of ellipsoids from given selected $m^{\rm th}$ point from the drawn M points. The Bayesian evidence can finally be estimated as

$$\hat{\mathcal{Z}} = \frac{1}{N_{\rm tot}} \sum_{k=1}^{N_{\rm tot}} \frac{\mathcal{L}(\Theta_k)\pi(\Theta_k)}{g(\Theta_k)} \tag{1.37}$$

with the estimation of the posterior probability density as

$$P(\Theta) = \frac{\mathcal{L}(\Theta)\pi(\Theta)}{N_{\rm tot} g(\Theta)}. \tag{1.38}$$

Ultimately, the estimation of the Bayesian evidence, otherwise known as the marginal likelihood (or the marginal loglikelihood, $\ln \mathcal{Z}$, as used within this manuscript) indicates how trustworthy any one specific model is compared to other models. Within SIMTOI, once the difference between nested sampling and importance nested sampling are within a given tolerance, a solution to a model is formed given an interferometric data set.

1.2.2 *Image Reconstruction*

To determine a unique solution for imaging, we need to apply prior information to constrain an image. We can describe an imaging problem in terms of *maximum a posteriori*, which contains two penalty terms: a likelihood and a prior. The likelihood constrains the image to data while the prior constrains the image to a known boundary (Baron 2016). The optimum

image is obtained when the sum of the likelihood and the prior are minimized, given by

$$\boldsymbol{x}_{\text{opt}} = \underset{x \in \mathbb{R}^n}{\arg\min} \left\{ \chi^2(\boldsymbol{x}) + \mu R(\boldsymbol{x}) \right\} \tag{1.39}$$

where $\chi^2(\boldsymbol{x})$ is the likelihood and $\mu R(\boldsymbol{x})$ is the prior. The μ within the prior term is the hyperparameter (or the weighting term) which determines how much of an influence the prior will have against the likelihood when finding an optimum image, and the $R(\boldsymbol{x})$ term is the regularization. The difficulty of obtaining an adequate image arises from balancing the likelihood against the prior. Using a low hyperparameter value results in an image riddled with artifacts (χ^2 dominate regime), while using a high hyperparameter value results in an over-regularized image that sticks very closely to the prior ($\mu R(\boldsymbol{x})$ dominate regime).

Most image reconstruction techniques consist in the application of Equation 1.39. One of the most important priors to implement in image reconstruction is enforcing positivity. Whether the intensity or the temperature of an image are being optimized, both need to be positive since they are a physical feature of the source. Other regularizations, such as maximum entropy or the l_2 norm, are also used within imaging codes; however, total variation has been the most widely employed recently, and especially in interferometric imaging (Renard et al. 2011). The total variation regularization looks at neighboring pixels within an image and computes the spatial gradient between these neighboring pixels, therefore, penalizing large temperature fluctuations between neighboring pixels. This technique allows for global intensity or temperature variations (if the hyperparameter value is small enough) while having a smoother intensity or temperature distributions on a local scale.

Optimization of Equation 1.39 has been historically done through various means such as using stochastic methods (simulated annealing or parallel tempering), Alternating Direction Method of Multipliers (ADMM), or gradient-based methods (see Baron 2020, and references therein). For this work, we focus on two specific optimizers for imaging: the Nelder-Mead Simplex method (commonly known as the amoeba or downhill simplex method; Nelder &

Mead 1965; Box 1965; Richardson & Kuester 1973) within the NLopt package (Johnson 2007) and the quasi-Newtonian method Variable Metric Limited Memory with Bounds (VMLMB) within the OptimPack package (Thiebaut 2002).

The Nelder-Mead Simplex method does not require a gradient and solves for a solution on a local scale. In order to come to a solution, the method starts by selecting $n + 1$ points on a grid depending on the dimensionality n of the problem. For example, if there are three dimensions, four points are chosen randomly on the grid, making a pyramid. The algorithm takes a series of steps depending on the nature of the shape of the simplex (i.e., reflection, expansion, and contraction of the shape base on each point). Multiple contractions of the n-dimensional will eventually lead to a solution to the problem. VMLMB is similar to Newton's method in that the gradient is only needed and is also used to approximate the Hessian. The combination is used to examine the direction of the criterion gradient and the curvature of the overall grid. A solution is found for VMLMB when the gradient becomes close to a certain threshold.

1.3 RS Canum Venaticorum Variables

Perhaps the first written observations about magnetic spots on the Sun were noted by the ancient Greeks around the 4th century BCE (Vaquero 2007), while around the same time in imperial China, similar observations of the Sun were noted by the astronomer Gan De (Temple 1986). Many other civilizations also took note of these sunspots and continued recording these observations. However, it took around two millennia until any notice of spot activity would be detected on a star beyond our Sun. Kron (1947) obtained photometric observations of four eclipsing binary systems and hypothesized that the photometric variability could not be explained through ordinary means but through spots. These observations turned out to be the first detection of magnetic spot activity on other stars.

We now know that stars ranging from pre-main sequence to giants exhibit magnetic spot activity of their surfaces (Strassmeier 2009). Since the advent of space missions, such as

CoRoT (Baglin et al. 2006a,b) and *Kepler* (Borucki et al. 2010; Koch et al. 2010), many more stars have been observed to exhibit magnetic activity (Frasca et al. 2011; Fröhlich et al. 2012; Roettenbacher et al. 2013, 2016a; Nielsen et al. 2019; Santos et al. 2019). These stellar features constitute major sources of uncertainty trying to calculate accurate stellar physical parameters (e.g., $T_{\rm eff}$ and $R_\star$; Somers & Pinsonneault 2015). Starspots have other astrophysical significance tying them to accurately determining exoplanetary parameters. Any uncertainties found in the host star's physical parameters are amplified to any of their planetary parameters, as deriving exoplanetary parameters are dependent on the parent star. Magnetic properties of spots can also affect their surrounding environment including close-in planets, and in some cases these planets can back-react onto the host star (e.g., Shkolnik et al. 2003; Catala et al. 2007; Kashyap et al. 2008; Lanza 2008).

RS Canum Venaticorum (RS CVn) variables, named after the prototype of its class, are known to show large magnetic starspots (Hall 1976; Kővári et al. 2015; Roettenbacher et al. 2016b, 2017). These variables are often found in a binary system, and the pair often consists of an evolved giant primary with the secondary being a smaller main-sequence companion (Berdyugina 2005; Strassmeier 2009). Magnetic spots in these systems are often easier to observe because of their larger relative size to the star, thus making RS CVn variables ideal observing targets. Hall (1976) classified these RS CVn variables to have the following features (as noted in Berdyugina 2005):

i. photometric variability;

ii. Ca II emission lines;

iii. subgiant component well within its Roche lobe;

iv. fast rotation (i.e., almost synchronized binaries with orbital periods of a few days) and;

v. orbital period variations.

Hall (1976) further categorizes RS CVn variables into subgroups with similar features as the standard RS CVn. The more important of the two groups are the short and long-period binary systems. The short-period binary subgroup constitutes of binaries that fulfill all the RS CVn requirements but have binary orbital periods of less than one day and are non-contact binaries. The long-period binary subgroup has similar features to the ordinary RS CVn variables but has binary orbital periods greater than two weeks and may be semi-detached or completely detached.

1.3.1 *Starspot Properties*

Arguably, two of the most important observational features of these RS CVns spots can be driven down to their starspot lifetimes and spot temperature differences with a star's photosphere. In general, starspot lifetimes can be tied down to several factors (Hussain 2002):

i. spots on tidally locked binary systems can live longer (a few months) compared to single main-sequence stars (a few weeks);

ii. polar spots may have a different lifetimes compared to other observed starspots;

iii. starspot lifetimes may live, on average, to around a year (based on time-series photometry) and;

iv. starspot longitude reversal could eliminate a spot's signature in a light-curve and conceal its decay rate.

In the study by Hall & Henry (1994), it has been found that small starspots seemed to have lifetimes proportional to their sizes while large starspots, like those on RS CVns, can survive for many years and live on certain active longitudes. Strassmeier et al. (1994) observed the RS CVn variable HR 7275 with the intention of following 20 different spots, or spot groups, and found that individual spots can live up to 4.5 years with an average lifetime of 2.2 years (based on starspot lifetime laws from Hall & Henry 1994).

Amplitude light-curve variations are a direct indication of stellar photosphere temperature variations. Cool starspots on RS CVns can cause these variations by quite a noticeable amount, with the largest variations observed on the two RS CVn variables HD 12545 and II Pegasi reaching a $\Delta V = 0.63$ mag (Strassmeier 1999; Tas & Evren 2000). In cases like these, these spots are shown to cover up to 20% of the total surface of the star. These can correspond to temperature differences between the photosphere and the cool spot of 500 K to 1900 K (Berdyugina 2005, and references therein). In order to directly observe these spots on the surfaces of RS CVns, three main techniques are routinely employed to image these systems: light-curve inversion, Doppler imaging, and interferometric imaging.

1.3.2 *Imaging of RS CVn Variables*

Photometric monitoring of RS CVns provides straightforward evidence for stellar spots, as shown in many other systems observed by the *Kepler* spacecraft (e.g., Frasca et al. 2011; Fröhlich et al. 2012; Roettenbacher et al. 2013, 2016a). The inverse problem of imaging the stellar surface from photometry is light-curve inversion (Wild 1989; Roettenbacher et al. 2013). The main drawback of broadband light-curve inversion is that photometry only provides relative information about the latitude of starspots (Harmon & Crews 2000) and relies on prior knowledge of the stellar limb-darkening. Light-curve inversion from multiband photometry alleviates the latitude ambiguities, resulting in more accurate solutions (Harmon & Crews 2000).

Regardless of the few drawbacks, the large area of spot coverage from RS CVns compared to our Sun has allowed light-curve inversion maps of a handful of RS CVn systems (e.g., Roettenbacher et al. 2011, 2016a, 2017). While pure photometric studies had given evidence of surface differential rotation (e.g., Henry et al. 1995), light-curve inversion serves a more direct method for differential rotation detection. One of the more recent methods for light-curve inversion applied to RS CVns is the algorithm by Harmon & Crews (2000). In short, the algorithm is based on a similar minimization from Equation 1.39, except that

the regularization also has a bias term. This bias term weights the regularization such that patches on the star would favor lower temperatures or intensities. Since RS CVns are riddled with cool spots, this updated method seems optimal for these types of stars.

Doppler imaging (Goncharskii et al. 1977; Rice et al. 1981) is another class of inverse methods for imaging stellar surfaces from spectroscopic data. This technique uses perturbations of absorption features on a star to better estimate the spot's latitude and longitude. However, there are still uncertainties in determining spot location for stars near edge-on rotation. High-resolution spectra are needed in Doppler imaging to distinguish the features due to the starspots in the absorption lines and to be able to detect their locations accurately. High rotational velocities rotationally broaden absorption lines and are required to ensure that the spectroscopic impact of a spot moving across the surface is shorter than the spot's evolution timescale. Piskunov & Wehlau (1990) determined lower bounds enabling Doppler imaging to be from 6 km/s to 15 km/s, which corresponds to spectrograph resolving powers of at least 20,000 to 50,000.

Various RS CVn variables have been observed through this method to obtain Doppler images (Strassmeier 2009, and references therein) which as proven successful at displaying spot motion. Several methods have been proposed to solving the inverse problems within Doppler imaging, including using maximum entropy (Vogt et al. 1987) and the Occamian approach (Berdyugina 1998). The difference in solutions between each method diminishes when the data quality is of good quality (Berdyugina 2005).

Contrary to Doppler imaging or light-curve inversion, interferometry provides unambiguous evidence that a spot is being shown without any assumptions on latitude. Interferometric modeling allows the determination of angular parameters, such as the inclination or position angle of a spotted star. However, interferometric observations can only be managed on a limited number of targets (i.e., relatively bright targets) compared to photometric and spectroscopic targets. Furthermore, only targets of sufficient angular size can be resolved from Earth. To date, three RS CVn variable stars have been interferometrically imaged: λ An-

dromedae (Parks et al. 2021), ζ Andromedae (Roettenbacher et al. 2016b), and σ Geminorum (Roettenbacher et al. 2017). It was only in 2007 that interferometric synthesis imaging became possible (Monnier et al. 2007) thanks to longer baselines and the combination of light from four (and now up to six) different telescopes.

1.3.3 *The RS CVn Variable λ Andromedae*

This work will focus on the RS CVn variable λ Andromedae (HD 222107; hereafter λ And). The primary star in λ And is a bright G8III-IV long-period RS CVn variable ($V = 3.82$, $H = 1.40$) with spots and is included in the third edition of the Catalog of Chromospherically Active Binary Stars (Eker et al. 2008). The system is a single-lined spectroscopic binary system with a rotation period of 54.07 days for the primary (Henry et al. 1995) in asynchronous rotation with its companion. It is in a nearly circular orbit for the system with an eccentricity of $e = 0.084 \pm 0.014$ and an orbital period of 20.5212 ± 0.0003 days (Walker 1944). The most recent estimate of the effective temperature and mass for the primary star of λ And is 4800 ± 100 K and $1.3^{+1.0}_{-0.6}$ $M_{\odot}$ (Drake et al. 2011). The companion is most likely a low mass main sequence star or a massive brown dwarf based on its mass ratio of $q = 0.12^{+0.07}_{-0.04}$ (Donati et al. 1995).

As most studies focus on the primary star in the λ And system since the secondary difficult to observe, any reference to λ And throughout the rest of this manuscript will be in reference to the primary unless specifically referenced otherwise. λ And has been shown to have very strong Ca II H & K emission (Gratton 1950) and it has been found that strength of these lines was correlated with the photometric period (Baliunas & Dupree 1982). Further spectroscopic studies have also found λ And to show Mg II h & k emission lines (Linsky et al. 1978; Baliunas & Dupree 1979; Basri & Linsky 1979) as well as Hα emission (Elston et al. 1982). Since it remains to be one of the brighter RS CVn variables in the sky, it has been the subject of numerous photometric studies (e.g., Bopp & Noah 1980; Boyd et al. 1983; Henry et al. 1995) since the discovery of its variability (Calder 1938). A study by

Bopp & Noah (1980) estimated that the large amplitude variations in photometry caused by λ And's spots corresponded to temperature differences between the spot and the photosphere of $\sim$800 K while another study found a spot to photosphere difference of 1050 K (Poe & Eaton 1985). Over 14.8 years, Hall et al. (1991) obtained and collected photometry from various observatories to establish an 11.4 ± 0.4 year spot cycle.

While tracking spot migration and location can prove challenging, a handful of attempts have been made at producing light-curve inversion maps or models of the surface of λ And. Using B and V photometry, Donati et al. (1995) reconstructed light-curve inversion maps over two to three months in two different epochs. Their light-curves showed one large spot for each epoch using the maximum entropy method with a surface filling factor of approximately $50 - 60\%$. While these images may be seemingly unrealistic, they roughly represent the activity on the surface, corresponding to a calculated spot to a photosphere temperature difference of 800 K, consistent with previous works. One issue that arises from the production of these light-curve inversion maps stems from the calculation of the inclination, $i = 60^{\circ}{}^{+30}_{-15}$. Later on, Frasca et al. (2008) compiled surface models based on V photometry and spectra, which produced spots and plagues that more accurately represented the surface of λ And. Similar to previous works, the spot to photosphere temperature difference in Frasca et al. (2008) was also calculated to be around 880 K.

Various attempts have been made to estimate the angular diameter of λ And using direct and indirect methods. The first angular measurements using long-baseline interferometry of λ And were made by Nordgren et al. (1999), who calculated a limb-darkened angular diameter of 2.66 ± 0.08 mas with a corresponding physical radius 7.4 ± 0.2 $R_{\odot}$. Using indirect methods such as intrinsic brightness and color can often yield a larger range of imprecise results, and in the case of λ And can yield angular diameter results ranging from $2.7 - 3.4$ mas or $3.9 - 7.8$ $R_{\odot}$ (Pasinetti Fracassini et al. 2001, and references therein).

Since long baseline interferometry obtains accurate and precise angular diameter measurements, and with the advent of aperture synthesis imaging providing accurate surface

features, λ And became one of the newest targets for imaging. The new 2D snapshot interferometric images of λ And from Parks et al. (2021) were produced with data obtained at the Center for High Angular Resolution Astronomy (CHARA) Array. Their study estimated that the angular diameter for the primary of λ And is 2.759 ± 0.050 mas, which corresponds to a physical radius of $7.831^{+0.067}_{-0.065}$ $R_{\odot}$ based on the *Hipparcos* distance of 26.41 ± 0.15 pc (van Leeuwen 2007). The modeling and imaging presented in Parks et al. (2021) more clearly defined the location and sizes of each spot as well as the corresponding temperature ratio between each spot and the photosphere.

1.4 Rapidly Rotating Stars

One of the often overlooked stellar parameters is usually stellar oblateness. Usually, main sequence stars are assumed to be mostly spherical if the star does not have any unusual properties (e.g., the star in a close binary system with Roche lobe overflow or the star is so massive that it starts shedding its outer layers). Even our own Sun, which rotates around its own axis on average every 28 days, has a small amount of oblateness ($b/a-1$) around 8×10^{-6} given that the solar radius is approximately $959.89''$ (Meftah et al. 2015). This oblateness, while very minuscule, gives a pole to equator difference of 7.84 ± 0.29 mas (Meftah et al. 2015) and is therefore safe to assume a spherical shape. However, there are many other stars for which you can no longer assume a spherical shape as the degree of oblateness for some start reaching levels of $20\% - 30\%$ (van Belle 2012).

Rapid rotators are of high interest because these stars have equatorial speeds that can reach up to 95% of their escape velocity. The fast rotation makes the photosphere bulge at the equator due to the centrifugal force. As a consequence, the surface brightness and effective temperature vary with latitude (brighter poles and darker equator), a phenomenon known as gravity darkening. Gravity darkening was first predicted by the von Zeipel law (von Zeipel 1924a), who first derived that the local surface flux from a star can be related to the local surface gravity, $F \propto g$. Using the Stefan-Boltzmann law, $F = \sigma T_{\rm eff}^4$ (σ is the

Stefan-Boltzmann constant), this relates the effective temperature of the star to the local surface gravity $T_{\rm eff} \propto g^{0.25}$. While this approximation can be applied to stars with radiative envelopes, it does not hold for all types of stars. With stars with convective envelopes, Lucy (1967) found that there is a weaker dependency between the local surface temperature and local surface gravity, $T_{\rm eff} \propto g^{0.08}$. Therefore, a general relationship for rapid rotators can be made as

$$T_{\rm eff} \propto g^{\beta} \tag{1.40}$$

where β is a variable between 0.08 and 0.25.

Studying these rapid rotators is not limited to understanding the nature of gravity darkening but has more physical implications in stellar astronomy. Rotation in stars promote chemical mixing, and rapid rotation in high-mass stars, compared to their non-rapidly rotating counterparts, show higher chemical mixing (Pinsonneault 1997). Rotation in higher mass stars also creates different evolutionary tracks on the HR diagram depending on their rotation rate (see Figure 1.3; Meynet & Maeder 2000). Not only is rapid rotation important for understanding massive stars, since they are the progenitors of Wolf–Rayet stars, supernovae, and gamma ray bursts, but it also influences galactic astronomy (Maeder & Meynet 2010) because they contribute to the galactic metallicity.

Most theoretical codes are one-dimensional and either do not take into account rapid rotation or have a simplistic estimate of rotation and difficulties reproducing results from observational data (Rieutord et al. 2016, and references therein). However, a two-dimensional code called Evolution STEllaire en Rotation (ESTER; Rieutord 2006) has shown realistic models of rapidly rotating stars with differential rotation and meridional circulation (Espinosa Lara & Rieutord 2013). As described in Espinosa Lara & Rieutord (2013), ESTER uses Poisson's equation, the equation of entropy, the momentum equation in an inertial frame, and the equation of mass conservation in order to make up the state of a radiative star. The equation of state, opacity, and nuclear generation are defined in the code as well to evolve any rapid rotators. ESTER has also been able to produce models with physical

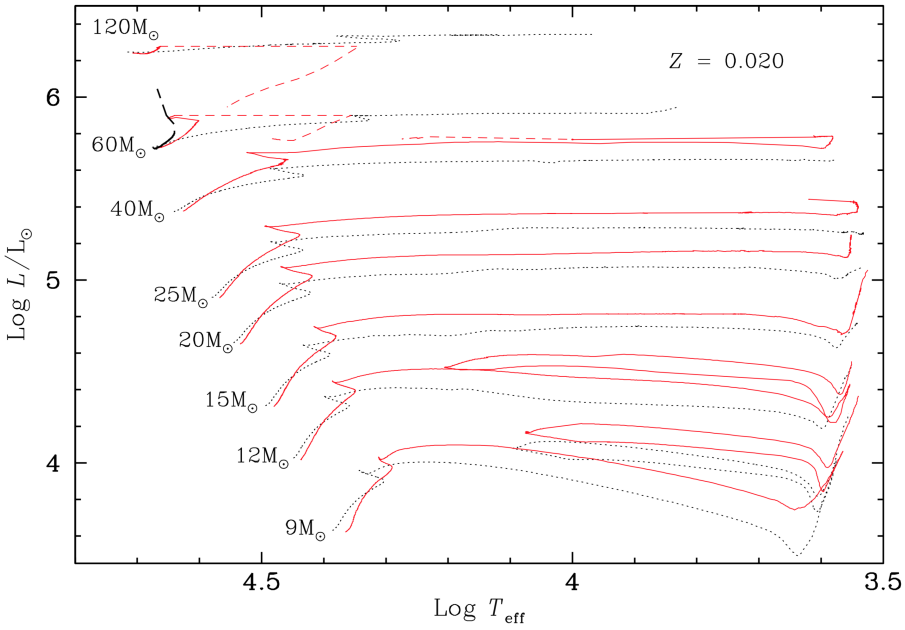

Figure 1.3 We show the evolutionary tracks of different mass stars ranging from 9 $M_\odot$ to 120 $M_\odot$ for a given metallicity of Z = 0.020. The non-rotating stars are denoted by the dotted black lines and the rapid rotating stars (∼300 km/s) by the solid red lines. This figure is adopted from Meynet & Maeder (2000) reproduced with permission © ESO.

parameters consistent with some interferometric observations (see Che et al. 2011; Monnier et al. 2012; Espinosa Lara & Rieutord 2013).

1.4.1 *Historical Spectroscopic and Interferometric Observations*

The first mention of tying stellar rotation to spectroscopic observations of stars began with Abney (1877) who suggested that stellar rotation could be observed from spectral line broadening. While that was the idea was quickly cast off by Vogel (1877) because they noted that the broadened hydrogen lines mentioned in Abney (1877) were also accompanied by narrow lines, the first observations tying stellar rotation to spectroscopic observations started with Schlesinger (1909, 1911). Schlesinger's observations focused on two eclipsing binaries, λ Tauri and δ Librae, and used what was later known as the Rossiter–McLaughlin effect (Rossiter 1924; McLaughlin 1924) to measure the variations in the apparent radial velocity from the rapidly rotating primary star. It was not until the work by Shajn & Struve (1929)

that predicted how the spectral lines were shaped from rotation Doppler broadening in stars, even though the effect was mostly accentuated for binary systems. Elvey (1930) soon used these spectral line shapes to obtain the first list of rotational velocities of stars, which were then followed by many other catalogs and studies that investigated stars between the O and F spectral types (e.g., Struve & Elvey 1931; Westgate 1933a,b, 1934; Slettebak 1949).

While the spectroscopic observations of rapid rotators had quick progression after the first Doppler broadening measurements, it took about 80 years after the first angular measurements of Betelgeuse by Michelson and Pease for there to be interferometric measurements of stellar oblateness. These first observations of oblateness were taken with the Palomar Testbed Interferometer by observing Altair (van Belle et al. 2001) using two different baselines (even though the diameter of Altair was measured by the Intensity Interferometer at Narrabri by Hanbury Brown et al. 1974, and could only solve for a uniform disk model). Many interferometric observations of rapid rotators soon followed within the next decade. Domiciano de Souza et al. (2003) observed another rapid rotator, Achernar, at the Very Large Telescope Interferometer (VLTI) to find a large amount of oblateness. Ohishi et al. (2004) revisited Altair using the Navy Prototype Optical Interferometer (later renamed to the Navy Precision Optical Interferometer, NPOI) and not only confirmed its oblateness, but the closure phases showed an indication of a bright pole, consistent with gravity darkening. Eventually, Monnier et al. (2007) observed Altair with the CHARA Array to produce the first image of a rapid rotator. The rapid progress of imaging soon followed as four other rapid rotators were imaged with CHARA within the subsequent five years (Zhao et al. 2009; Che et al. 2011). For this work, we will focus on one rapidly rotating star Alderamin.

1.4.2 *Alderamin*

Alderamin (α Cephei, HD 203280) is a bright A8V (Gray et al. 2003) rapidly rotating main sequence star ($V = 2.46$, $H = 2.13$) which was first spectroscopically identified as such by Slettebak (1955). Spectroscopic measurements of this star show that the rotation velocity

values have a large extent, ranging from $v \sin i = 180 - 265$ km s^{-1} (Abt & Morrell 1995; Abt & Moyd 1973). Alderamin was first interferometrically observed as the second commissioning target for the CHARA Array by van Belle et al. (2006) and later revisited by Zhao et al. (2009) in order to fully characterized.

The work by van Belle et al. (2006) used the K_s band CLASSIC beam combiner with two different baselines to ultimately fit a Roche model for Alderamin. The resulting angular diameter measurements confirmed Alderamin's oblateness given a polar angular radius of $0.6753^{+0.0119}_{-0.0135}$ mas and equatorial angular radius of $0.8767^{+0.0293}_{-0.0183}$ mas with a corresponding fractional angular velocity of $\omega_c = 0.9585$. As β was left as a free parameter ($\beta = 0.084^{+0.026}_{-0.049}$), the temperature distribution across the surface ranged from 8440 K at its pole to 7490 K at its equator, indicating that Alderamin has a more convective envelope as opposed to a radiative one. Given these parameters, van Belle et al. (2006) saw that Alderamin almost made two full rotations per day and calculated it to be $2.0 \pm 0.15\ M_\odot$.

The follow-up observations by Zhao et al. (2009) saw some disparity between their results and those by van Belle et al. (2006). Zhao et al. (2009) used the Michigan Infrared Beam Combiner (MIRC) combining four telescopes together which provided six non-redundant baselines with the addition of closure phases. The latter's work seemed to be more reliable as there was larger (u, v) coverage and the closure phases showed direct indication of the asymmetric brightness distribution, and so the work provided a completely different temperature distribution across Alderamin's surface. The combination of a larger (u, v) coverage allowed for surface imaging of the star as well as the fitting of two difference Roche models, a standard von Ziepel model and a β-free model. The adopted β-free model of $\beta = 0.216 \pm 0.021$ completely changed the nature of understanding of Alderamin as this showed that the temperature difference between the pole and equator was ~ 2000 K, a much larger temperature distribution than that from van Belle et al. (2006).

1.5 The Future of Interferometry

Long baseline optical interferometry has allowed for observations in the milliarcsecond regime. Current long-baseline interferometers propagate light from their telescopes to a lab via vacuum tubes. There are currently three active optical interferometers in the world. The CHARA Array uses vacuum pipes, and adaptive optics (AO) for compensating aberrations in the lab in the near-infrared. NPOI has vacuum pipes to transfer light in the visible and VLTI transfers light through pipes in the infrared. As this work focuses on data obtained with the CHARA Array, we will describe the faculty in more detail compared to NPOI or VLTI.

The CHARA Array is an interferometric array with six 1 meter telescopes, in a Y-shaped configuration, and has the world's longest operational baseline (at 330 meters) in optical interferometry (McAlister et al. 2005; ten Brummelaar et al. 2005). CHARA uses these large baselines to observe in both the visible to near-infrared, thus providing broad wavelength coverage. The facility has provided angular size measurements of many stellar disks (e.g., Boyajian et al. 2012) and has imaged a wide variety of objects including: rapid rotators (e.g., Monnier et al. 2007; Zhao et al. 2009; Che et al. 2011), binary systems (Zhao et al. 2008), triple systems (Baron et al. 2012), nova eruptions (Schaefer et al. 2014), and RS CVn variables (Roettenbacher et al. 2016b).

NPOI and VLTI can configure their telescopes to extend the (u, v) coverage; however, there are limitations. NPOI is able to combine light from six different siderostats at a given time, and each of those siderostats can be placed at any of the several different stations (Armstrong et al. 1998). VLTI has two different types of telescopes available for beam combining but only allows four telescopes to be combined at a time (Schöller 2007). The large 8.2 meter Unit Telescopes at VLTI are at fixed locations, while their 1.8 meter Auxiliary Telescopes are smaller and can be positioned at up to 30 different stations. CHARA is the only facility out of the active facilities that does not have the ability to move telescopes to

different stations, but it is the only facility that can combine light from six telescopes at once.

CHARA, NPOI, and VLTI all have their telescopes at fixed positions during a night, although that the latter two can re-position their telescopes during the day. Having movable telescopes throughout the night would increase (u, v) coverage for better imaging. However, using vacuum pipes is not a practical solution for active movable telescopes due to the rigidity of the vacuum pipes. One viable solution would be to use fiber optics to propagate light from the telescopes to the lab. Fiber optics, though, have some disadvantages in that they are limited to monochromatic light in bandpass, and are open to wear from weathering effects and temperature changes. Open-air beam propagation is an attractive alternative solution for propagating light if facilities have moving telescopes, and is what we endeavor to explore here. One immediate application for open-air beam propagation is CHARA's newest project with the installation of a seventh, potentially mobile, telescope.

Horizontal beam propagation is a fascinating subject for astronomy since we are interested in understanding the ground layer turbulence; it also has military applications. Recent lab work by Corley has done some work by simulating horizontal propagation through deep turbulence by studying phase modulations using spatial light modulators, and amplitude variations through extended beam paths (Corley et al. 2011). Bos has done some theoretical work to simulate horizontal beam propagation only using phase but with anisoplanatic patches within the images (Bos & Roggemann 2012). Hernandez has done some work in the lab by testing phase perturbations through the use of fans to create "atmospheric turbulence" instead of using spatial light modulators like some of the previous works mentioned here (Hernandez et al. 2020). There have also been attempts at estimating beam propagation tests in the field in a study made by Vorontsov (Vorontsov et al. 2010). Vorontsov's work showed that there are different intensity scintillation patterns based on the specific wavelength that is propagated horizontally.

1.6 Summary of Projects

In this manuscript, we will cover a range of topics that are centered around optical interferometry. Imaging stellar surfaces provides a description of their physical characteristics and out of the three main imaging techniques, interferometric imaging provides an unambiguous interpretation of surface temperature variations. There is one other 3D code able to interferometrically image spheroids but is limited by its use of stochastic methods to solve for the imaging and unavailable for public use. Our main goal for our work is to demonstrate the capabilities of our new imaging code and its application for interferometric imaging of two different astronomical objects as there are no other open-source 3D imaging codes available. Our secondary goal is directly tied to interferometric imaging as we build a novel optical setup that will set the basis for improved imaging quality of future interferometric targets. This work will lay the groundwork for complete dynamical imaging and make it available for large-scale use.

In Chapter 2, we will describe our 3D imaging algorithm ROTIR and how we develop it to image stellar surfaces. In Chapter 3, we use the RS CVn variable λ Andromedae as a test case for ROTIR. We will use the archival data used using the MIRC instrument at the CHARA Array and compare our imaging algorithm to previous imaging codes. In Chapter 4, we will describe how we obtained interferometric data of the rapid rotator Alderamin using the upgraded Michigan InfraRed Combiner, Exeter (MIRC-X) instrument. We will also describe how we apply ROTIR to obtain a new image of Alderamin, and compare that to the 2D theoretical radiation transfer model, ESTER. In Chapter 5, we describe a novel free-space beam propagation project and how that will lay the groundwork for future optical interferometric facilities. Finally, we conclude with a review of our results and describe any future work in Chapter 6.

Chapter 2
3D INTERFEROMETRIC MODELING AND IMAGING WITH ROTIR

Our code ROTational Image Reconstruction (ROTIR) is a three-dimensional open-source Julia code (Baron & Martinez 2018; Martinez et al. 2021; Baron & Martinez in prep) which models the stellar surface temperatures of single stars or binary systems as two-dimensional arrays on top of a stellar geometry. The stellar geometry itself is defined either by analytic formulas (ellipsoids, fast rotators) or by solving Roche equations. In imaging and model-fitting problems, ROTIR makes use of the optimization packages OptimPack (Thiebaut 2002) and NLopt (Johnson 2007) to maximize the posterior probability of the model. Since our aim is to develop and provide a robust imaging code, we describe which models our code is dependent on, how we convert our objects' visibilities to compare them to interferometric observables, and which algorithms we use to make surface maps.

2.1 Geometrical Setup

Our code is dependent on the package, OITOOLS (Baron et al. 2019), which is able to read, plot, and model interferometric data. We use OITOOLS as a way to read in our data, split up or combine our data temporally, and plot any squared visibilities or closure phase data featured in this work.

Once the interferometric data are read, we define the stellar parameters and orientation of our star. Our code requires several parameters: the angular size at the pole in milliarcseconds, the surface temperature, the fractional critical angular velocity if the star is rapidly rotating, the limb-darkening law and its corresponding coefficient(s), the exponent needed if there is any gravity darkening (von Zeipel 1924a), the difference in angular velocity between the equator and the pole, the inclination, position angle, and rotation period of the star. Our code allows the user to choose between three different limb-darkening laws: a quadratic law, logarithmic law, or Hestroffer law (commonly known as the power law; Hestroffer 1997).

Our geometrical setup starts with selecting a tessellation scheme, or groups tiles of a 3D grid with no overlaps or gaps between each tile. Two schemes have been implemented so far: the HEALPix tessellation (Górski et al. 2005) and the latitude/longitudinal scheme. HEALPix presents the advantage of equal area tessels, provided the star does not depart too much from a spherical shape (approximately 1%). The latitude/longitudinal scheme allows for simulating differential rotation but requires more tessels to represent the surface. As part of this work, we tested both tessellation schemes, which result in qualitatively identical maps. Most results presented in this manuscript were obtained with the latitude/longitude scheme. The number of pixels per angular diameter was chosen based on the estimated angular diameter size divided by the imaging resolution limit. Therefore, the minimum total number of pixels required across the surface of a star would simply be the number of latitude pixels times the number of longitude pixels. Here, each latitude band would have the same number of pixels, and higher latitude surface elements are smaller in area than those near the equator.

For the latitude/longitude scheme, the number of latitude pixels is based on the number of pixels per angular diameter since the latitude range spans from -90° to 90° and the number of longitude pixels is twice the number of pixels per angular diameter since the longitude ranges from 0° to 360°. We number the vertices of the polygon by $1, 2, 3, 4$ in a counterclockwise direction when viewed along the direction of the normal. A fifth element is also included for each pixel and defined to be at the center of each pixel.

Once the user has chosen a tessellation scheme and calculated the number of pixels needed, the user then has the choice of choosing between three different geometries: a scaled unit-sphere, an oblate spheroid, or a Roche object. Technically, the model of the star is a polyhedron since the surface is made up of many different pixels and not one solid surface. In order to describe the overall shape of the star, we choose to name them as 3D objects instead of polyhedrons. A scaled unit-sphere is based on the radius that is input by the user. We first develop the coordinates on a spherical grid and then convert them to Cartesian

coordinates by using the following

$$\begin{aligned} x &= R_{\rm p} \sin(\theta) \cos(\phi) \\ y &= R_{\rm p} \sin(\theta) \sin(\phi) \\ z &= R_{\rm p} \cos(\theta) \end{aligned} \tag{2.1}$$

where $R_{\rm p}$ is the radius of the star at the pole, θ is the colatitude ranging from 0° to 180°, and ϕ is the longitude spanning the range of 0° to 360°. The colatitude here is later converted to the astronomical convention of a latitude later in the code and will range from −90° to 90°. We also slightly modify Equation 2.1 to make an ellipsoid with the user's choice of length for each Cartesian direction with the following

$$\begin{aligned} x &= a \sin(\theta) \cos(\phi) \\ y &= b \sin(\theta) \sin(\phi) \\ z &= c \cos(\theta) \end{aligned} \tag{2.2}$$

where a, b, and c are the axial lengths in the respective x, y, z directions. Examples of a spherical model in HEALPix and latitude/longitude tessellation schemes as well as an ellipsoid are shown in Figure 2.1.

2.1.1 *Making Oblate Spheroids*

From Equation 2.2, one can approximate the geometry of an oblate spheroid. However, it is much easier to depend on a Roche model (Roche 1837) in order to describe the nature of rapidly rotating stars. For our models describing rapid rotators that will be used to set up for imaging, we use the following expression to define the stellar radius (Collins 1963; Collins & Harrington 1966): (Collins 1963; Collins & Harrington 1966):

$$R(\omega_c, \theta) = \frac{3R_{\rm p}}{\omega_c \sin(\theta)} \cos\left[\frac{\pi + \cos^{-1}(\omega_c \sin\theta)}{3}\right] \tag{2.3}$$

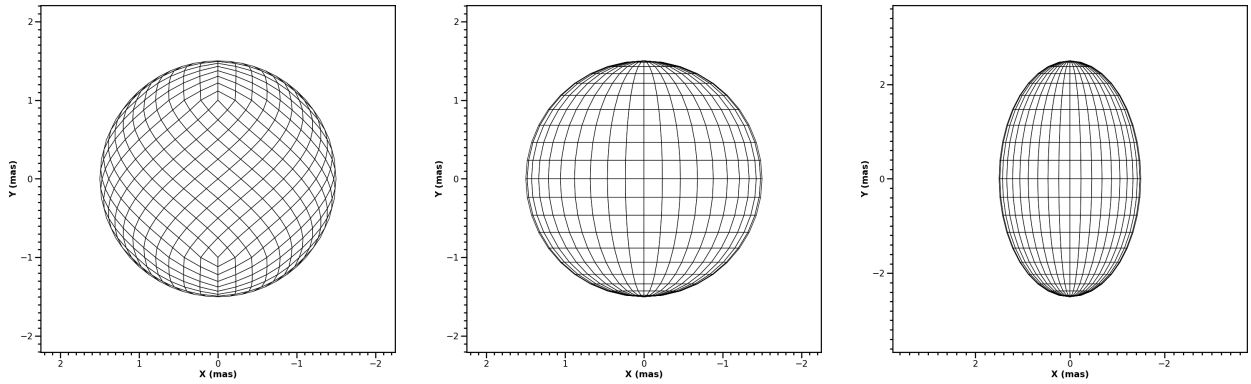

Figure 2.1 Left: An example of the HEALpix tessellation for a scaled unit-sphere with a radius of 1.5 mas. Middle: An example of the latitude/longitude tessellation for a scaled unit-sphere with a radius of 1.5 mas. Right: An example of the latitude/longitude tessellation for a spheroid with axial lengths of $a = 1.5$, $b = 2$, and $c = 2.5$.

where ω_c is the fraction of the critical angular velocity and θ is the same colatitude from Equation 2.1. The fraction of the critical angular velocity is defined as

$$\omega_c \equiv \frac{\Omega}{\Omega_{\rm crit}} \tag{2.4}$$

where Ω is the rotational velocity of the star and $\Omega_{\rm crit}$ is the critical angular velocity. The critical angular velocity here is a point where the centrifugal acceleration is equivalent to the gravitational acceleration and can be derived as

$$\Omega_{\rm crit} = \sqrt{\frac{8}{27}\frac{GM_\star}{R_{\rm p}^3}} \tag{2.5}$$

where G is Newton's gravitational constant and $M_\star$ is the mass of the star. For rapid rotators, the point at which the oblateness of the star reaches its greatest point is when the equatorial radius ($R_{\rm e}$) is $R_{\rm e,crit} = 3/2R_{\rm p}$.

While interferometric observations usually use Equation 2.4 as the reference for angular velocities, the theoretical model ESTER uses a different definition within their work. The fraction of Keplerian angular velocity as used in ESTER and ESTER related works (Rieutord

2006; Espinosa Lara & Rieutord 2011, 2013; Rieutord et al. 2016) is defined as the following

$$\omega_k = \Omega \sqrt{\frac{R_{\rm e}^3}{GM_\star}} = \frac{\Omega}{\Omega_k} \tag{2.6}$$

where Ω_k is the Keplerian angular velocity at the equator. A relation between the fraction of the critical angular velocity and the Keplerian angular velocity can be written as

$$\frac{\omega_k}{\omega_c} = \sqrt{\frac{8}{27}\left(\frac{R_{\rm e}}{R_{\rm p}}\right)^3}. \tag{2.7}$$

ROTIR uses the fraction of the critical angular velocity and converts between the two internally whenever dealing with models from ESTER. Examples of the Roche geometry for rapid rotators is shown in Figure 2.2.

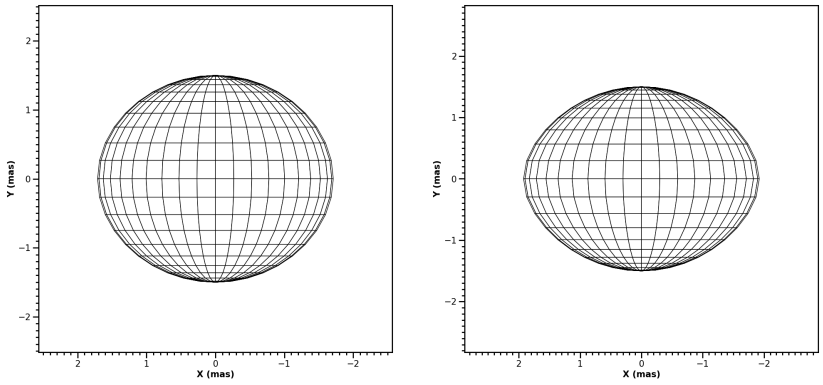

Figure 2.2 Left: An example of a rapid rotator with a polar radius of 1.5 mas and $\omega_c = 0.8$. Right: An example of a rapid rotator with a polar radius of 1.5 mas and $\omega_c = 0.95$.

2.1.2 *Roche Binaries*

There have been a handful of systems that have been imaged by CHARA (e.g., Zhao et al. 2008; Baron et al. 2012) or other interferometers that are either in binary or triple systems. Therefore, we are motivated to include the geometry of binaries with in ROTIR for future 3D binary imaging and incorporate the Roche lobe calculator by Leahy & Leahy (2015). Following their work, we start with a dimensionless form of the Roche potential (i.e., potential

energy per unit mass) obtained by dividing the potential energy by GM_1/a where M_1 is the mass of primary star within the binary and a here is the binary separation. The equation can then be shown as (Kopal 1959; Pathania & Medupe 2012)

$$\Upsilon(\breve{r},\theta,\phi) = \frac{1}{\breve{r}} + q\left(\frac{1}{\sqrt{1-2\breve{r}\sin\theta\cos\phi+\breve{r}^2}} - \breve{r}\sin\theta\cos\phi\right) + \frac{q+1}{2}p^2\breve{r}^2\sin^2\theta \tag{2.8}$$

where $\breve{r}$ is the physical (or angular) radius measurement normalized by the binary separation, $q = M_2/M_1$ here is the mass ratio between the secondary and primary star, and $p = \Omega_{\rm star}/\Omega_{\rm binary}$ is used for a system that is in asynchronous rotation (Limber 1963). For elliptical orbits, (Sepinsky et al. 2007) has adopted a further correction where one can replace p^2 by the following

$$A(p,e,\nu) = \frac{p^2(1+e)^4}{(1+e\cos\nu)^3} \tag{2.9}$$

where e is the eccentricity and ν is the true anomaly for the binary system. This alters Equation 2.8 so it now becomes

$$\Upsilon(\breve{r},\theta,\phi) = \frac{1}{\breve{r}} + q\left(\frac{1}{\sqrt{1-2\breve{r}\sin\theta\cos\phi+\breve{r}^2}} - \breve{r}\sin\theta\cos\phi\right) + \frac{p^2(q+1)(1+e)^4}{2(1+e\cos\nu)^3}\breve{r}^2\sin^2\theta. \tag{2.10}$$

While Equation 2.10 lists all of the potential energy at every given point, we must further define potentials at two more points in order to calculate the physical (or angular) radius of the system. The first potential required is the potential energy at the L_1 Lagrangian point. Out of the five total Lagrangian points, the L_1 point lies in between the two stars in the binary system. A good approximation of the radius of the star at the L_1 point is typically estimated using the Eggleton formula (Eggleton 1983). However, we use the slight modification in the Leahy & Leahy (2015) Fortran code for our starting approximation in the form of

$$R_{\rm L_1} = \frac{0.49}{0.6 + q^{2/3}\ln(1+q^{-1/3})}. \tag{2.11}$$

After using the modified Eggleton formula, we use Newton's method to get the true value for radius of the star at the L_1 point. Once we arrive at a solution for Equation 2.11, we use Equation 2.8 to find the potential energy at the L_1 point. We can finally calculate the potential energy at the surface given a fill-out factor F (a value of how much of the Roche lobe in a binary is filled) in the following

$$\Upsilon_F = \frac{\Upsilon_{L_1} + \frac{q^2}{2(1+q)}}{F} - \frac{q^2}{2(1+q)}. \tag{2.12}$$

Using the mass ratio of the system, fill-out factor, asynchronous rotation ratio, Equations 2.11 and 2.12, we use Brent's method (Brent 1973) just as it was used in Leahy & Leahy (2015) to solve for the physical (or angular) radius at every point within the star. Since Leahy & Leahy (2015) notes that there are certain variables that are restricted to make their calculator accurate, we also apply the same restrictions and limit the mass ratio between $0.01 < q < 100$, the asynchronous rotation ratio between $0.01 < p < 2$, and fill-out factor between $0.1 < F < 1$. Examples of the binary star setup with different fill-out factors are shown in Figure 2.3.

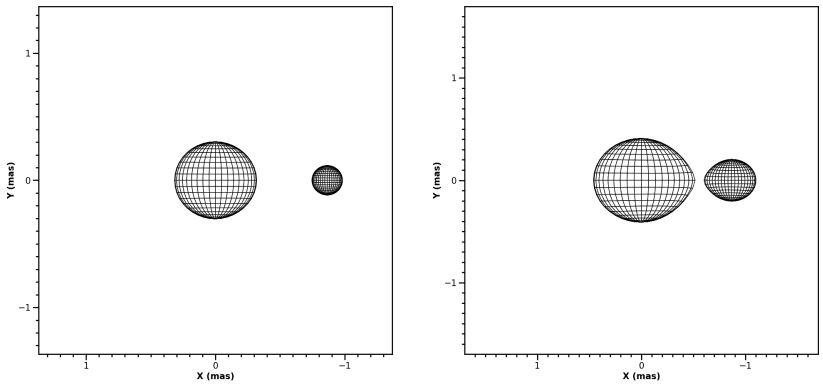

Figure 2.3 Left: An example of a binary system with a fill-out factor of $F = 0.75$. Right: An example of a binary system with a fill-out factor of $F = 0.99$.

2.2 Differential Rotation Option

The user can select whether or not to turn on the option to simulate differential rotation. While the simulation can be done using both tessellation schemes, it is much easier using the latitude/longitude scheme since edges of these neighboring pixels are directly north, south, east, and west of each other (with the exception of the poles). The equation for differential rotation (Henry et al. 1995) used in our code is in the form

$$\Omega(\theta) = \Omega_{\rm e} - \Delta\Omega \sin^2 \theta \tag{2.13}$$

where θ is the colatitude, $\Omega(\theta)$ is the rotation rate at a specific latitude, $\Omega_{\rm e}$ is the rotation rate at the equator, and $\Delta\Omega$ is the difference in angular velocity between the equator and the pole. This difference between angular velocity in the equator and the pole is related to the differential rotation coefficient, k, or the surface shear parameter, α, commonly found in the literature (e.g., Henry et al. 1995; Davenport et al. 2015; Kővári et al. 2015) and is defined through the following equation

$$k = \frac{\Omega_{\rm e} - \Omega_{\rm p}}{\Omega_{\rm e}}, \tag{2.14}$$

or in terms of the polar and equatorial rotational periods as

$$k = \frac{P_{\rm p} - P_{\rm e}}{P_{\rm p}} \tag{2.15}$$

where $\Omega_{\rm p}$ is the rotation rate at the pole, $P_{\rm p}$ is the rotation period at the pole, and $P_{\rm e}$ is the rotation period at the equator.

2.3 Going from a 3D Geometry to a Visibility

Once the user selects the desired geometry of the source, we then move onto converting the three-dimensional object to interferometric visibilities (once a three-dimensional rotational matrix has been applied based on the position angle, inclination, and rotation period of the object). Since the pixels are mapped on a (x, y, z) plane, they are ordered on the surface of the star counterclockwise when viewed along normal of the positive z direction. The surface area $\mathbf{A}_n$ of n pixels are then calculated in order to find the flux coming from the star with the following

$$\mathbf{A}_n = \frac{1}{2}\sum_{j=1}^{m}(\mathbf{v}_j \wedge \mathbf{v}_{j+1}) \cdot \hat{\mathbf{z}} \tag{2.16}$$

where $\mathbf{v}$ is the vector of (x, y) projected positions of the n^{th} pixel in a 2-dimensional (x, y) plane at the j^{th} corner, and m number of corners in the polygon of choice, $\cdot$ is the scalar product, and $\wedge$ the vector cross product operator. The $m+1$ corner here points back to the first corner of the pixel.

Once the surface area of the pixels are calculated with the desired limb-darkening law, the Fourier transform $\mathbf{S}$ is done on every pixel for a 3-dimensional object (Lee & Mittra 1983; Chu & Huang 1989; McInturff & Simon 1991) in order to compare the frequencies of our data on the (u, v) plane by using the following equation

$$\mathbf{S}(\mathbf{k}) = \sum_{j=1}^{m} \hat{\mathbf{z}} \cdot [(\mathbf{v}_{j+1} - \mathbf{v}_j) \wedge \mathbf{k}] \, \frac{\text{sinc}[\mathbf{k} \cdot (\mathbf{v}_{j+1} + \mathbf{v}_j)]}{i2\pi|\mathbf{k}|^2} \exp[-i\pi\mathbf{k} \cdot (\mathbf{v}_{j+1} + \mathbf{v}_j)] \tag{2.17}$$

where $\mathbf{k}$ is a vector containing each u and v frequency on the (u, v) Fourier plane. We use the flux to visibility matrix $\mathbf{S}$ to compute the model visibilities using:

$$\mathbf{V} = \frac{\mathbf{S}(\mathbf{L} \circ \mathbf{T})}{\mathbf{A}^{\top}(\mathbf{L} \circ \mathbf{T})} \tag{2.18}$$

where $\mathbf{V}$ is the model complex visibility vector, $\mathbf{T}$ is the temperature map vector, $\mathbf{L}$ is the limb-darkening map, $\circ$ is the Hadamard (element by element) vector product, and the division is the Hadamard division.

2.4 Temperature Priors and Image Optimization

ROTIR uses a combination of two different image optimization techniques in order to find the stellar parameters, the best temperature maps, and images. While it is possible to have a uniform temperature for a spheroid as a prior, an optimizer may converge faster if a model temperature map was used as a prior. In order to make surface temperature maps for rapidly rotating stars and binary systems, we rely on two models for the prior: the von Zeipel law (see Section 1.4) and what we designate as the Espinosa Lara-Rieutord law.

In Espinosa Lara & Rieutord (2011), a new model was proposed in order to better explain the nature of latitudinal variations for stars at any rotation rate as an improvement over the von Zeipel law. This new model has been compared to ESTER, and there has been an overall good agreement between the two models. Therefore, we apply this newly dubbed Espinosa Lara-Rieutord law into ROTIR. Espinosa Lara and Rieutord ultimately define a temperature distribution of a rotating star as

$$\begin{aligned} T_{\rm eff}(\widetilde{r},\theta) &= \left(\frac{F_\star}{\sigma}\right)^{1/4} = \left(\frac{L_\star}{4\pi\sigma G M_\star}\right)^{1/4} \sqrt{\frac{\tan\vartheta}{\tan\theta}}\, g_{\rm eff}^{1/4} \\ &= \left(\frac{L_\star}{4\pi\sigma R_{\rm e}^2}\right)^{1/4} \left(\frac{1}{\widetilde{r}^4} + \omega_k^4 \widetilde{r}^2 \sin^2\theta - \frac{2\omega_k^2 \sin^2\theta}{\widetilde{r}}\right)^{1/8} \sqrt{\frac{\tan\vartheta}{\tan\theta}} \end{aligned} \tag{2.19}$$

where $F_\star$ is the flux of the star, σ is the Stefan-Boltzmann constant, $L_\star$ is the luminosity of the star, G is the gravitational constant, $g_{\rm eff}$ is the local gravity for any given point on a star, $\widetilde{r} = R(\theta)/R_{\rm e}$ is the radius of the star normalized by the equatorial radius, and ϑ is an arbitrary variable.

Before we can derive a colatitude-dependent temperature, we first need to calculate the effective temperature at the pole. We first start with the following solution for $\widetilde{r}$

$$\frac{1}{\omega_k^2 \widetilde{r}} + \frac{1}{2}\widetilde{r}^2 \sin^2\theta = \frac{1}{\omega_k^2} + \frac{1}{2} \tag{2.20}$$

and the flux as defined in Espinosa Lara & Rieutord (2011)

$$F_{\omega_k}(\theta) = \frac{\tan^2\vartheta}{\tan^2\theta}. \tag{2.21}$$

Furthermore, two boundary conditions for Equation 2.21 are defined in Espinosa Lara & Rieutord (2011) as

$$F_{\mathrm{p},\omega_k}(\theta = 0) = \exp\left(\frac{2}{3}\omega_k^2 \widetilde{r}^3\right) \tag{2.22}$$

and

$$F_{\mathrm{e},\omega_k}(\theta = \pi/2) = \left(1 - \omega_k^2 \widetilde{r}^3\right)^{-2/3}. \tag{2.23}$$

Now, we can finally arrive at a solution for the polar temperature given that Equation 2.20 becomes $\widetilde{r}_\mathrm{p} = 2/\left(2 + \omega_k^2\right)$ and Equation 2.19 becomes

$$T_{\mathrm{eff,p}} = \left(\frac{L_\star}{4\pi\sigma R_\mathrm{e}^2}\right)^{1/4} \left(\frac{2}{2+\omega_k^2}\right)^{-1/2} \exp\left(\frac{4}{3}\frac{\omega_k^2}{\left(2+\omega_k^2\right)^3}\right). \tag{2.24}$$

We can make a general solution for the colatitude-dependent temperature in terms of the polar temperature using both Equations 2.19 and 2.24 as

$$\frac{T_\mathrm{eff}(\widetilde{r},\theta)}{T_{\mathrm{eff,p}}} = \left(\frac{1}{\widetilde{r}^4} + \omega_k^4 \widetilde{r}^2 \sin^2\theta - \frac{2\omega_k^2 \sin^2\theta}{\widetilde{r}}\right)^{1/8} \sqrt{\left(\frac{\tan\vartheta}{\tan\theta}\right)\left(\frac{2}{2+\omega_k^2}\right)} \exp\left(-\frac{4}{3}\frac{\omega_k^2}{\left(2+\omega_k^2\right)^3}\right). \tag{2.25}$$

However, there is still an issue in solving for this arbitrary variable ϑ in Equation 2.25. In order to solve for ϑ, we use the equation from Espinosa Lara & Rieutord (2011) written

out as

$$\cos\vartheta + \ln\left(\tan\frac{\vartheta}{2}\right) = \frac{1}{3}\omega_k^2\widetilde{r}^3\cos^3\theta + \cos\theta + \ln\left(\tan\frac{\theta}{2}\right). \tag{2.26}$$

and use a combination of Broyden's method (Broyden 1965) and the bisection method. We note that this quasi-Newtonian method is used for radii $\widetilde{r}$ between $0^\circ < \theta \leq 71.25^\circ$ (and its symmetric counterpart in the southern hemisphere of the star). There are issues in root solving between $71.25^\circ < \theta \leq 90^\circ$ using Broyden's method, thus we rely on the bisection method for accurate calculations of ϑ.

We implemented three different regularizations for use in ROTIR: positivity, l_2 norm, and total variation. After the user chooses a hyperparameter value with a regularization, the geometric square visibilities, closure phases, and triple amplitudes are compared to the data using OptimPack to obtain the optimal temperature map under the assumption that the user has obtained the correct physical characteristics of the star. However, OptimPack does not produce any errors of the star, therefore we rely the NLopt algorithm, specifically the Nelder-Mead Simplex method (Nelder & Mead 1965; Box 1965; Richardson & Kuester 1973) within NLopt, for bootstrapping in order to incorporate for both statistical and systematic errors. For this work, the type of bootstrapping implemented here is a random re-sampling of the observation dates (or observing brackets). Within each Nelder-Mead search, an OptimPack optimization is calculated to produce the lowest criterion value ($\chi^2(\boldsymbol{x}) + \mu R(\boldsymbol{x})$ within Equation 1.39) for the given stellar parameters. In addition to producing temperature maps, we assume that any flux is linearly related to the temperature since observations from CHARA occur in the Rayleigh-Jeans tail of the spectral energy distribution.

Chapter 3
THE TEST CASE, λ ANDROMEDAE

We have several motivations for revisiting the RS CVn variable, λ And. The large spot structures make it easier to detect and would be a viable candidate for interferometric image reconstruction. Since it was previously imaged with a two-dimensional code, SQUEEZE (Baron et al. 2010, 2012), it did not have any time-dependent imaging analysis. Therefore, we aim to display the imaging capabilities of our code ROTIR and compare it with prior imaging results. From an astrophysical standpoint, we aim to examine the spot evolution of λ And over two different epochs, which will give a first direct indication of its stellar dynamo. We also attempt to find any evidence for differential rotation as it may provide any further insight into its stellar dynamo (Martinez et al. 2021).

3.1 Using Archival Data from the CHARA Array

We reuse the 2010 and 2011 data from Parks et al. (2021), shown in Table 3.1 and calibrators in Table 3.2 used for each respective year, for our analysis. These data were obtained using the CHARA Array (ten Brummelaar et al. 2005) with the MIRC instrument (Monnier et al. 2004, 2010) in H-band with the average wavelength of 1.61 μm. The observations were done in prism mode (R $\approx$ 50), which contains eight spectral channels with an average spectral bandwidth of 33.6 nm. The data taken in 2010 were taken with a combination of four out of six telescopes which provide six visibilities, three independent bispectrum amplitudes (triple amplitudes), and three independent bispectrum phases (closure phases). The 2011 data set benefited from MIRC having been upgraded earlier that year, allowing for simultaneous use of all six telescopes. These upgrades provided data sets to acquire up to 15 visibilities, 10 independent triple amplitudes, and 10 independent closure phases for each spectral channel.

Table 3.1. CHARA Array Observations for λ Andromedae

UT date	Average MJD	Baselines	Number of $\|V\|^2$ points	Number of Closure Phases	Rotation Phase of Primary	Calibrators
2010 Aug 02	55410.4	S1-E1-W1-W2	167	88	0.0	7 And, 37 And
		S2-E2-W1-W2				
2010 Aug 03	55411.3	S1-E1-W1-W2	454	264	0.012	σ Cyg, 7 And, 37 And
		S2-E2-W1-W2				
2010 Aug 10	55418.3	S1-E1-W1-W2	425	288	0.146	σ Cyg, 7 And, 37 And
		S2-E2-W1-W2				
2010 Aug 11	55419.3	S1-E1-W1-W2	215	136	0.164	σ Cyg, 7 And, 37 And
2010 Aug 18	55426.3	S1-E1-W1-W2	429	272	0.293	σ Cyg, 7 And, 37 And
		S2-E2-W1-W2				
2010 Aug 19	55427.3	S1-E1-W1-W2	406	264	0.312	σ Cyg, 7 And, 37 And
		S2-E2-W1-W2				
2010 Aug 24	55432.3	S1-E1-W1-W2	526	320	0.404	σ Cyg, 7 And, 37 And
		S2-E2-W1-W2				
2010 Aug 25	55433.3	S2-E2-W1-W2	120	72	0.423	σ Cyg, 7 And, 37 And
2010 Sep 02	55441.3	S1-E1-W1-W2	522	336	0.570	7 And, 37 And
		S2-E2-W1-W2				
2010 Sep 03	55442.3	S1-E1-W1-W2	588	352	0.589	7 And, 37 And

Table 3.1 (cont'd)

UT date	Average MJD	Baselines	Number of $\|V\|^2$ points	Number of Closure Phases	Rotation Phase of Primary	Calibrators
		S2-E2-W1-W2				
2010 Sep 10	55449.3	S2-E2-W1-W2	336	192	0.718	7 And, 37 And
2011 Sep 02	55806.5	W1-S2-S1-E1-E2-W2	360	432	0.310	σ Cyg, 7 And, 22 And, HR 653
2011 Sep 06	55810.5	W1-S2-S1-E1-E2-W2	392	376	0.384	σ Cyg, 7 And, 22 And, HR 653
2011 Sep 10	55814.5	W1-S2-S1-E1-E2-W2	360	432	0.458	7 And, 22 And
2011 Sep 14	55818.5	W1-S2-S1-E1-E2-W2	864	1104	0.532	7 And, 22 And, HR 653
2011 Sep 19	55823.5	W1-S2-S1-E1-E2-W2	808	1120	0.624	7 And, 22 And, HR 653
2011 Sep 24	55828.5	W1-S2-S1-E1-E2-W2	200	240	0.716	7 And, 22 And, HR 653, η Aur

Note. — Here we list the UT date, the average modified Julian date of the night of observation, the baselines used in their corresponding configuration, the number of useful squared visibility points obtained for the night, the number of useful closure phase points obtained for the night, the rotation phase for the primary star in λ And, and the calibrator stars that were used for each corresponding night. The rotation phase is derived by using the first observation in 2010 as the zero point.

Table 3.2. Calibrators for λ Andromedae

Calibrator Name	Calibrator Size (mas)	Source	Epoch Used
7 And (HD 219080)	0.65 ± 0.03	Mourard et al. (2015)	2010
37 And (HD 5448)	46.66 ± 0.06	Roettenbacher et al. (2016b)[a]	2010
σ Cyg (HD 202850)	0.542 ± 0.021	Zhao et al. (2008)	2010
7 And (HD 219080)	0.676 ± 0.047	SearchCal (Bonneau et al. 2006)	2011
σ Cyg (HD 202850)	0.54 ± 0.02	Barnes et al. (1978)	2011
22 And (HD 571)	0.591 ± 0.041	SearchCal (Bonneau et al. 2006)	2011
HR 653 (HD 13818)	0.646 ± 0.045	SearchCal (Bonneau et al. 2006)	2011
η Aur (HD 32630)	0.336 ± 0.023	SearchCal (Bonneau et al. 2006)	2011

[a]This is the semi-major axis angular separation of the binary calculated by Roettenbacher et al. (2016b).

Note. — The angular sizes for the 2011 epochs are based on what was reported from Parks et al. (2021) since we use their reduced and calibrated data. We use updated angular sizes for each calibrator star in the 2010 epoch since we do a new reduction and calibration.

3.1.1 *Data Reduction*

Parks et al. (2021) detail the reduction steps and error corrections, but we will briefly note some of their steps here. The data were reduced using the official IDL pipeline for reducing MIRC data (Monnier et al. 2007). Each block of raw fringe data contained coadded frames and was corrected for any instrumental effects by background subtraction to remove instrumental noise and foreground normalization to correct for any pixel-to-pixel variation. Raw square visibilities, closure phases, and triple amplitudes are output through the use of Fourier transforms and are photometrically calibrated. The data were corrected for the atmospheric coherence time and optical changes in the beam path with the use of calibrator stars that were taken either immediately before or after the target λ And.

In the 2010 data, one of the calibrators 37 And (HD 5448) was found to be a binary by Che et al. (2012) and had its orbit fully characterized by Roettenbacher et al. (2016b). Parks et al. (2021) formed a comparison of using 37 And as either a single star calibrator or as a binary calibrator. They found that these comparisons only incurred an error of

1.24% for the square visibilities, which is well below the multiplicative error correction, and a closure phase standard deviation of 1.14°. We execute a separate reduction and calibration for the 2010 data set using the official MIRC reduction pipeline to correct for the 37 And binary calibrator. We use the more recent calibrator diameter estimates, whose values differ from Parks et al. (2021), for this new reduction and calibration. The data uncertainties also go through a post-calibration process to account for known systematic errors of the MIRC instrument.

For the 2010 data, we kept the same systematic errors as Parks et al. (2021). These errors are different compared to the 2011 data set as the quality of the 2010 data are taken with a four telescope configuration and are of lower quality, while the higher quality 2011 data are taken with a six telescope configuration. A 15% multiplicative error correction was used in association with the transfer function, a 2×10^{-4} additive error correction was used in association with bias at low amplitudes for the square visibilities, and a 20% multiplicative error correction and a 1×10^{-5} additive error correction was used for the triple amplitudes. The same 1° error floor was used for the closure phases as was used in Zhao et al. (2011). We present the square visibilities and closure phases for the 2010 data set in Figure 3.1.

We use the same calibrator diameter estimates listed in Parks et al. (2021) since the 2011 data set has been reduced and calibrated. Even though different angular sizes were used for the calibration of the 2010 and 2011 data set for 7 And and σ Cyg, the differences between the two angular sizes reported in Table 3.2 are small and within their respective 1σ errors. Systematic errors were taken into account during calibration similar to that of Monnier et al. (2012). A 10% multiplicative error correction was used in association with the transfer function for the 2011 data, and a 2×10^{-4} additive error correction was used for the square visibilities. A 15% multiplicative error correction was used, and a 1×10^{-5} additive error correction was used for all the triple amplitude data. Lastly, the same 1° error floor was used for the closure phases just as it was presented in Zhao et al. (2011). We present the square visibilities and closure phases for all of the 2011 data set in Figure 3.2.

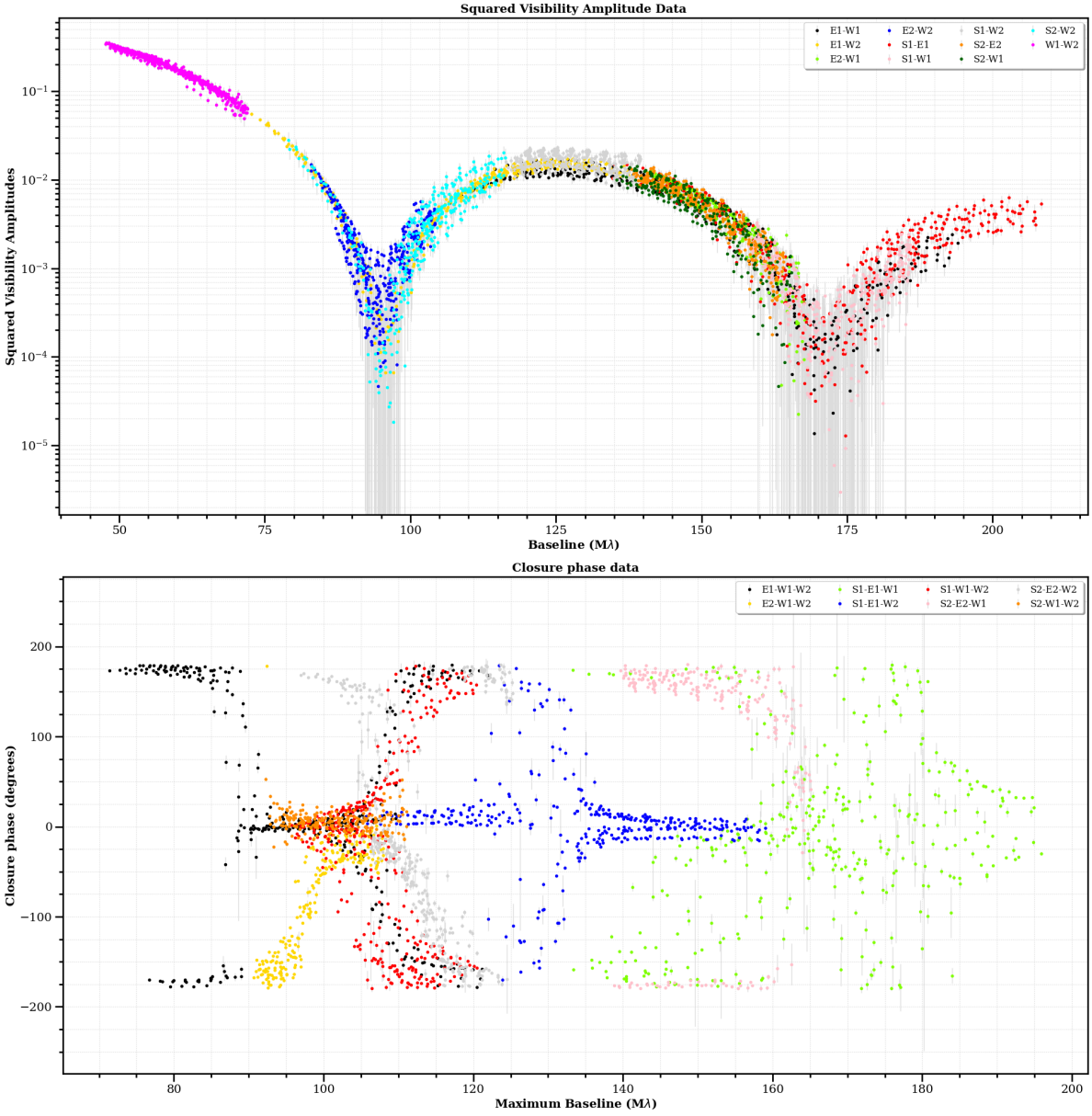

Figure 3.1 Top: $|V|^2$ points are plotted against the baseline length (in Mλ or B/λ) for a given baseline pair for all the data of λ And from the 2010 epoch. Bottom: Closure phase points are plotted against the baseline length (in Mλ) for the given baseline trio for the same 2010 data.

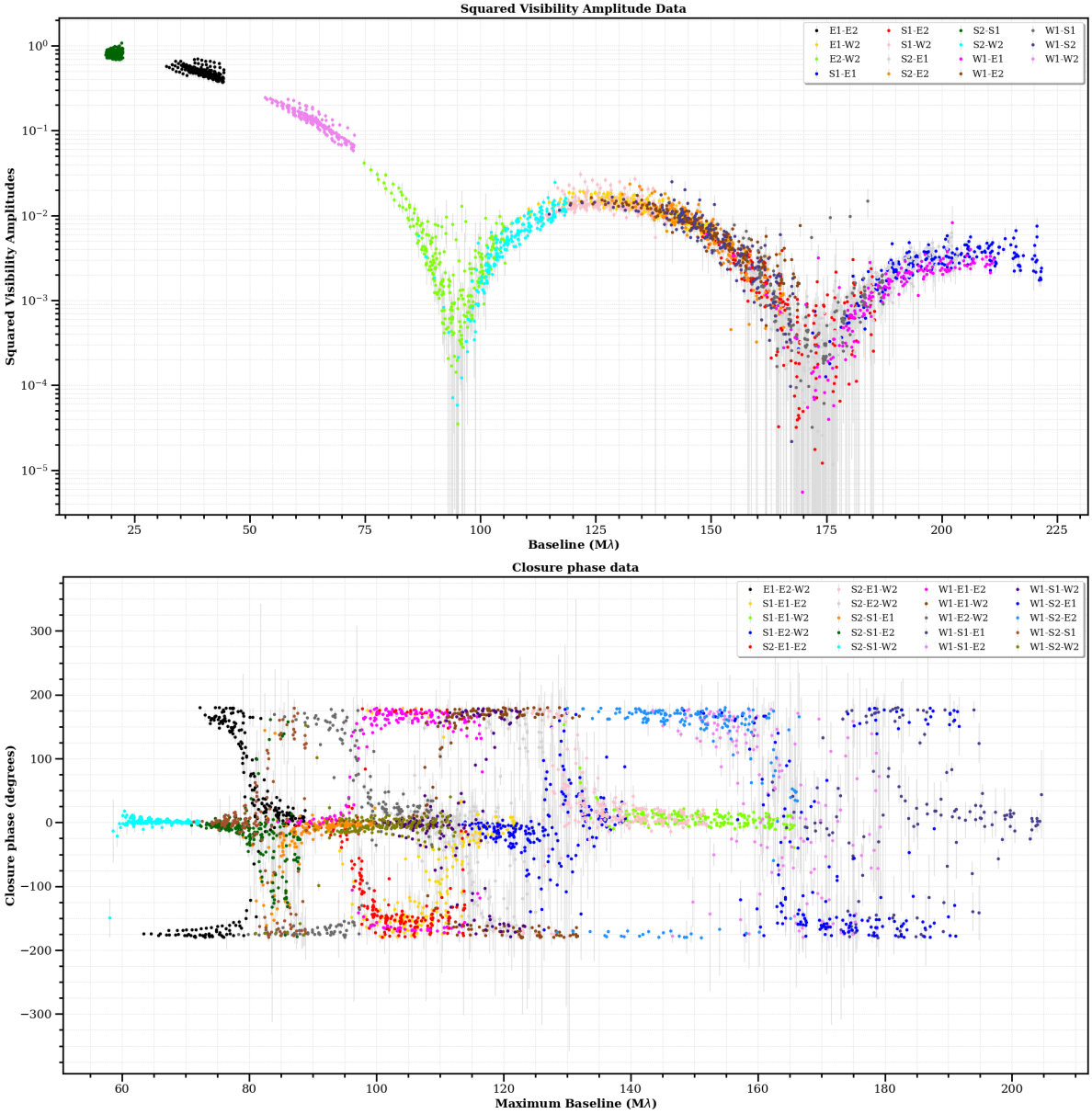

Figure 3.2 Top: $|V|^2$ points are plotted against the baseline length (in Mλ) for a given baseline pair for all the data of λ And from the 2011 epoch. Bottom: Closure phase points are plotted against the baseline length (in Mλ) for the given baseline trio for the same 2011 data.

3.2 Modeling λ Andromedae with SIMTOI

In order to get the first estimates of the physical parameters of λ And, we used the code SIMTOI and implemented the MultiNest algorithm (outlined in Section 1.2.1) to obtain global solutions to our multi-dimensional problem. We devised models of λ And with a different number of circular spots, from three to six spots. Six parameters were used to model the star itself: rotation period, rotation axis (inclination and position angles), temperature, angular diameter, and coefficient of the power limb-darkening law (Hestroffer 1997). The stellar parameters were given a uniform prior distributions within a wide range of values, based on the stellar parameters listed in Parks et al. (2021) as a starting point (e.g., $\pm 20^\circ$ for angular parameters). Four parameters were used per spot: longitude, latitude, diameter, and flux. These spot parameters were also given uniform distribution. In particular, their location was not constrained.

For each data set – 2010 or 2011 – SIMTOI renders an image per epoch (day). The rendering resolution was set to a 64×64 image with a 0.05 mas per pixel resolution. MultiNest was run for each model and converged after a few hours, providing *maximum a posteriori* parameter values, as well as the marginal likelihood values (the so-called $\log Z$).

3.2.1 *Modeling Results*

We report the χ^2 and $\log Z$ values for each spot model in Table 3.3. We also provide the approximate nominal values for the physical parameters. MultiNest does provide error bars, but since they do not account for systematic errors, they are vastly underestimated. While one could bootstrap the data before MultiNest runs, this would be too computationally intensive and yet still imprecise due to our approximate modeling of spots. Our model spots are circular, which may be an unrealistic assumption, but is sufficient to identify the main potential location of intensity peaks on the surface. The $\log Z$ values are maximal for the five spot model for the 2010 data and the four spot model for the 2011 data. The corresponding

Table 3.3. SIMTOI Results

Number of spots	Importance Nested Sampling value ($\ln Z$)		χ^2_ν	
	2010 data	2011 data	2010 data	2011 data
3	-67599.448761	10433.734767	56.855263	8.020829
4	-5968.401012	36157.820383	17.114268	3.102330
5	1420.128960	32785.721919	11.372939	3.710609
6	-45295.096429	30193.016672	38.679240	4.211333
Physical Parameters (4 spot model based on 2011 data)	Value			
$R_\star$ (mas)	1.37			
Limb-darkening coefficient	0.22			
Inclination (deg)	86.4			
Position Angle (deg)	26.7			
Rotation Period (days)	54.2			

Note. — Higher $\ln Z$ value is better, lower χ^2_ν is better. No error bars are calculated since the models from SIMTOI using Multinest does not currently generate reliable error bars. We rely on the imaging results for more precise measurements and calculation of errors.

reduced χ^2 values are low for the 2011 data and much higher for 2010. Setting aside the possible differences in error calibration between 2010 and 2011, this would indicate that the 2010 surface map is much more complex than the 2011 surface map (which we did confirm during imaging in Section 3.3.1).

We ultimately choose the 4 spot model for the 2011 data as the best representative model that produces the most accurate parameterization of λ And. The estimated 54.2 day rotation period of the primary from our model using the 2011 data set is consistent with other works. Henry et al. (1995) reports a rotation period 54.07 days from their photometric analysis while Parks et al. (2021) reports a 54.02 ± 0.88 day rotation period from their own photometric analysis and an average of a 56.9 ± 8.8 day rotation period from their interferometric analysis. While the 2010 data set had a larger rotation phase coverage than the 2011 data set, the rotation period based on the 2011 data is more reliable based on MultiNest results and the fitting of the model to the data. This is most likely due to the larger amount of (u, v) coverage, number (u, v) points, triple amplitudes, and closure phase points in the 2011 data

set compared to the 2010 data set. This calculated period from the four spot model using the 2011 data is consistent with previous works.

3.3 Applying ROTIR to λ Andromedae

For λ And, we use positivity and total variation as the two regularizers needed to determine the best image since Renard et al. (2011) determined that total variation outperforms other regularization methods. Using the l-curve method (Renard et al. 2011), we choose a weight of $\mu = 0.01$ that has a small amount of regularization before entering into a regularization dominated regime. We show examples of strong and weak regularization in Figure 3.3 for λ And on 2011-Sep-14 proving why we need a good balance between regularization and pure model fitting when finding an optimum image.

In order to determine of the number of tessels needed on the surface of the star, we use on the parameters we obtained from modeling λ And using SIMTOI. With the CHARA angular resolution limit being $\theta \approx 0.60$ mas at H-band ($\lambda = 1.61\mu$m), we estimate that we need 40 pixels across the whole equator to meet Nyquist sampling (imaging resolution limit is $\theta \approx 0.30$ mas in H-band). Therefore, we use 80 pixels around each latitude, including pixels behind the star, and 40 pixels across each longitude for a total of 3200 pixels on the surface of the star. Our sampling of pixels across the resulting images is solely based on the number of pixels on the surface on the star and not the overall field, as the field size can be arbitrarily chosen based on the plotting axes.

3.3.1 *A First Look at Imaging*

In order to find the best geometrical setup for the primary star in λ And, we test both a spherical star and a Roche lobe shape to see if there are any signs of major Roche lobe overflow. While Donati et al. (1995) and Parks et al. (2021) both suggest that there is no Roche lobe overflow, we decide to investigate this for λ And since slight oblateness was found in another RS CVn variable, ζ Andromedae (Roettenbacher et al. 2016b).

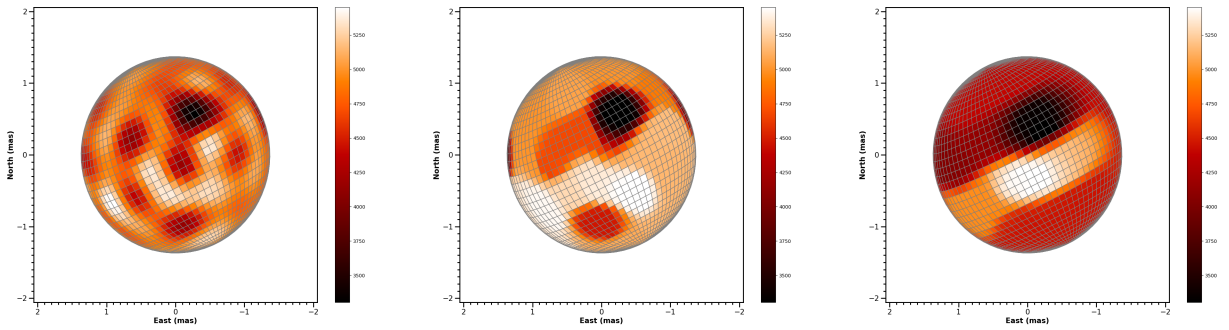

Figure 3.3 Left: Here we show an example of a reconstruction made with a very weak hyperparameter ($\mu = 0.0001$). This is close to the classic example of overfitting an image based on the data. Middle: Here we show where there is a good balance of fitting the data to a model and the use of a hyperparameter ($\mu = 0.01$). Right: Here we show an example where the hyperparameter is dominant ($\mu = 0.5$) and very loosely based on the data fitting the model.

We start with the parameters from SIMTOI to create our spherical geometrical star and, with the addition of several other orbital parameters such as the longitude of the ascending node, argument of periapsis, and eccentricity found in Walker (1944), create our Roche lobe geometry. Donati et al. (1995) states that λ And is coplanar, therefore we use the inclination rotation axis of the primary star as the inclination of the orbit for the latter case. We use the same hyperparameter and apply a uniform temperature map across the whole star as an initial condition for both geometries. Using a Julia package called OptimPack that solves for an optimum temperature map through a quasi-Newtonian method (Thiebaut 2002), we obtain for the best temperature map given all our data in a given year. This algorithm compares the Fourier transforms from Section 2.3 to the 2011 data to solve for the best temperature map.

The resulting criterion for the Roche lobe geometry is higher ($\chi^2(x)+\mu R(x) = 6288$) when directly comparing it to a spherical geometry (criterion = 4489). We also find that the pole-to-equator ratio at the L_1 Lagrangian point for the primary is 0.9967. With these two calculations, we consider to believe that a spherical geometrical shape for the primary for λ And is a good approximation for the true geometrical shape.

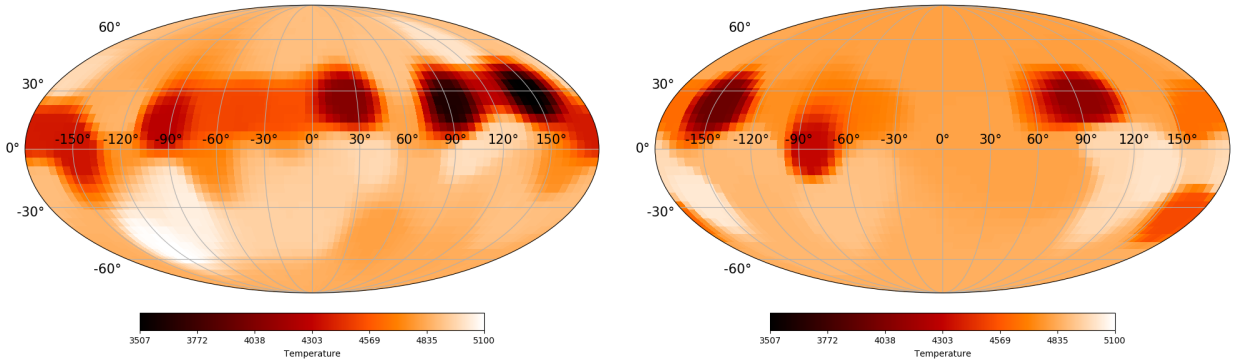

Figure 3.4 Here we show a Mollweide plot of λ Andromedae for the 2010 epoch (left) and 2011 epoch (right) using our ROTIR code. We combine our 11 nights of data in 2010 across 39 nights and 6 nights of data in 2011 across 22 nights to make the temperature map for the 2010 epoch and 2011 epoch, respectively. We note that the pixels not within the observing line-of-sight are calculated by starting at the effective temperature from Drake et al. (2011) and modified through OptimPack.

Once we have determined that the spherical geometrical setup is the most optimal for λ And and choose the most optimal regularization weight, we are now set for calculating the best fit for the temperature map. We present the resulting Mollweide maps of λ And for both epochs in Figure 3.4. However, these maps reflect no time variability and assume that λ And is undergoing solid-body rotation. A better representation of the temperature maps are shown in Figure 3.5 for each given night in 2010 and 2011.

A first look at the temperature maps between the 2010 and 2011 epochs shows a few interesting characteristics about λ And's surface. Comparing the two temperature maps show notable similarities for two spots in the northern hemisphere between the two epochs (i.e., the spot around 20° latitude and $\sim$ 100° longitude, and the spot around 0° latitude and 170° in both epochs). There are two other notable spots that either disappear or appear from one epoch to the next. The spot in the 2010 epoch around 30° latitude and 150° longitude seems to has disappeared within the 2011 epoch. A spot seems to be forming within the 2011 map in the southern hemisphere around $-40°$ latitude and 50° longitude with hints of its emergence with a similar place in the 2010 epoch. We note that the spot in the 2010

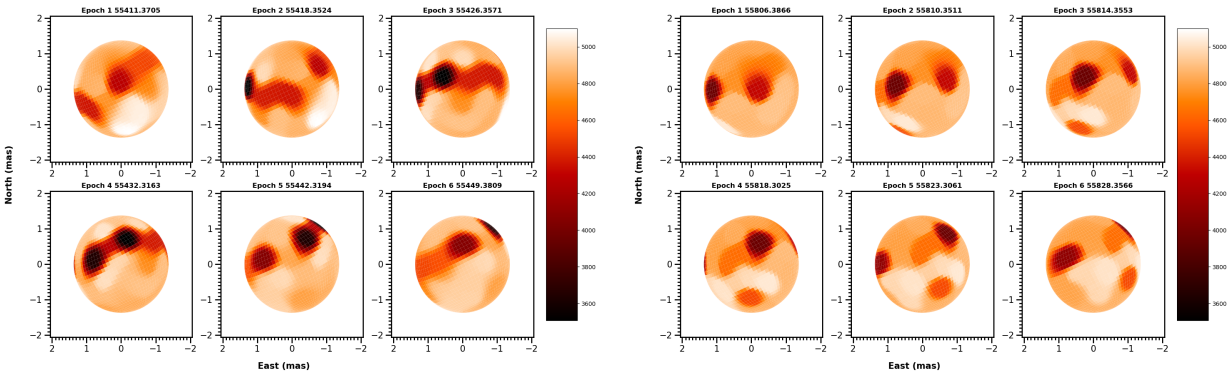

Figure 3.5 We show temperature maps of λ Andromedae for the 2010 epoch (left) and 2011 epoch (right) using our ROTIR code. Here, we note that our 2010 temperature map panels do not reflect all 11 nights of data but only show a subset of 6 nights. The nights for the 2010 temperature map panels are chosen by only selecting one of two consecutive observational nights and having the next temperature map panel be separated by at least 6 nights (i.e., 2010-Aug-03, 2010-Aug-10, 2010-Aug-18, 2010-Aug-24, 2010-Sep-03, 2010-Sep-10).

epoch around 15° latitude and −90° does not appear in the 2011 epoch. This is most likely due to missing rotational phase coverage in the 2011 data set.

3.3.2 *Refinement of Physical Parameters*

After finding the best model from SIMTOI, we use the parameters from the 4-spot model and use the bootstrap method to find the final parameters and errors for the primary component of λ And. We use 50 bootstrap iterations to solve for only four parameters: angular radius, the limb-darkening coefficient, inclination, and position angle. We choose to leave the rotation period of the primary fixed throughout this bootstrap because there is a degeneracy towards lower rotation periods. Our bootstrap is dependent on the NLopt package (Johnson 2007) and Nelder-Mead Simplex method (Nelder & Mead 1965; Box 1965; Richardson & Kuester 1973) within NLopt for obtaining our final parameters with their corresponding errors.

We restrict lower and upper bounds within NLopt for these four parameters as follows: [1.35, 1.39] mas for angular radius, [0.2, 0.3] for the limb-darkening coefficient, [70.0, 90.0] degrees for inclination, and [20.0, 30.0] degrees for position angle. The final values for each

variable parameter are chosen by averaging over all bootstraps and their associated errors are calculated through their standard deviation. While our 50 bootstraps do not fully show a Gaussian distribution and are restrained from doing a large amount of bootstraps due to computation time, we find that our results for each varying parameter do not deviate largely from the mean result. It is likely that doing more bootstraps will slightly increase the error bars but not in a significant manner. We show the results of our bootstrap values in Figure 3.6.

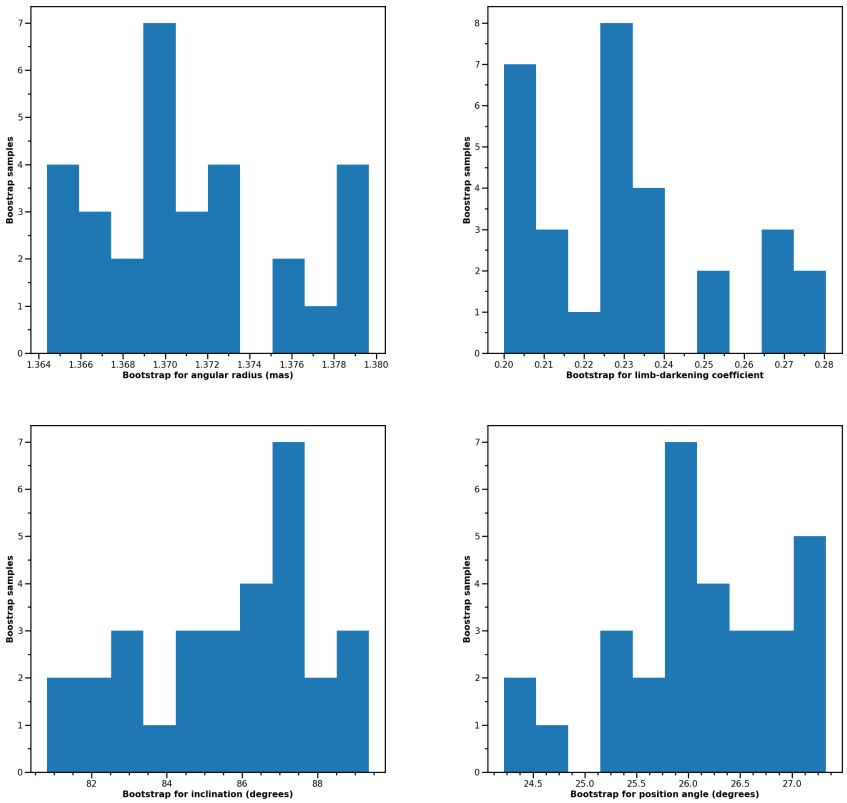

Figure 3.6 Here we show the results of using the bootstrap method varying angular radius, the limb-darkening coefficient, inclination, and position angle. We use 50 bootstraps in order to calculate the final parameters of λ Andromedae and bin them into 10 different bins. The x-axis here shows the range of the parameters from all the bootstraps and the y-axis show the number of bootstraps within each bin. While we plot calculated values for each bootstrap, we note that that the full range for each parameter are the following: [1.35, 1.39] mas for angular radius, [0.2, 0.3] for the limb-darkening coefficient, [70.0, 90.0] degrees for inclination, and [20.0, 30.0] degrees for position angle. The final parameters are calculated from taking the average of each respective parameter with their associated errors calculated from the standard deviation of the bootstrap results.

3.3.3 *Images of λ Andromedae*

Temperature maps are not indicative of what is actually represented from observations. In order to present an image, we include using a power law for limb-darkening (Hestroffer 1997) and multiply it by the cells of the temperature maps that are visible to the observer. We use the limb-darkening coefficient from our bootstrap to present the images in Figure 3.7 and present the physical parameters for the primary star in λ And using the parameters from our bootstrap in Table 3.4. The mass of λ And is calculated from our value of the physical radius and the $\log g$ from Drake et al. (2011), and luminosity was calculated from the effective temperature from Drake et al. (2011) and our value of the physical radius. These images are produced from these final parameters (in Table 3.4) and run through OptimPack.

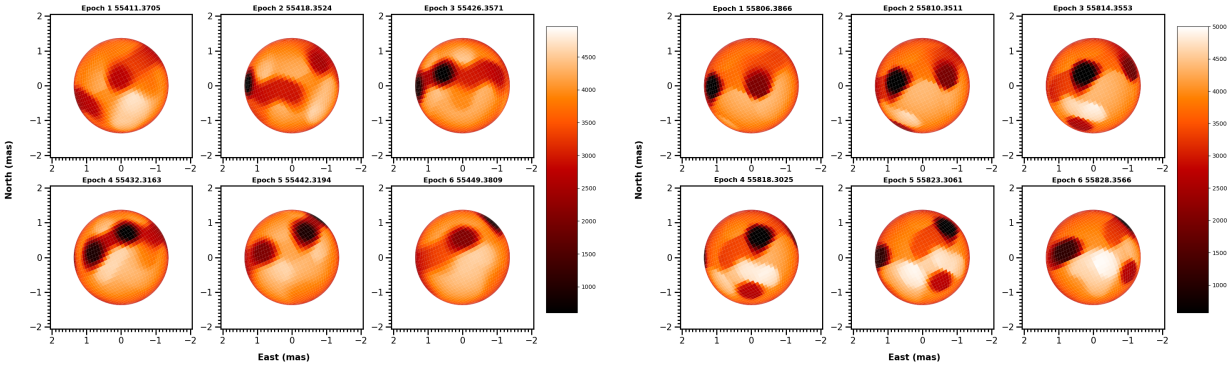

Figure 3.7 We show intensity maps of λ Andromedae for the 2010 epoch (left) and 2011 epoch (right) using our ROTIR code. Here, we note that our 2010 intensity map panels do not reflect all 11 nights of data but only show a subset of 6 nights. The nights for the 2010 intensity map panels are chosen by only selecting one of two consecutive observational nights and having the next intensity map panel be separated by at least 6 nights (i.e., 2010-Aug-03, 2010-Aug-10, 2010-Aug-18, 2010-Aug-24, 2010-Sep-03, 2010-Sep-10). All images here for both the 2010 and 2011 epochs reflect the same parameters that are listed in Table 3.4.

Table 3.4. Final λ Andromedae Parameters for the Primary

Observed Parameters	Value	Source	Values from Literature	Literature Reference
$R_\star$ (mas)	1.371 ± 0.005	This work	1.33 ± 0.04	Nordgren et al. (1999)
			1.379 ± 0.025	Parks et al. (2021)
Limb-darkening coefficient	0.231 ± 0.024	This work	0.229 ± 0.111	Parks et al. (2021)
Inclination (deg)	85.63 ± 2.32	This work	70.35 ± 6.7[a]	Parks et al. (2021)
Position Angle (deg)	26.09 ± 0.82	This work	21.6 ± 7.5[a]	Parks et al. (2021)
Rotation Period (days)	54.2	This work	56.9 ± 8.8[a]	Parks et al. (2021)
Physical parameters				
$R_\star$ ($R_\odot$)	7.787 ± 0.053	This work[b]	7.4 ± 0.2	Nordgren et al. (1999)
			7.0 ± 0.7	Drake et al. (2011)
			$7.831^{+0.067}_{-0.065}$	Parks et al. (2021)
$T_{\rm eff}$ (K)	4800 ± 100	Drake et al. (2011)	–	–
$\log g$	2.75 ± 0.25	Drake et al. (2011)	–	–
$M_\star$ ($M_\odot$)	1.24 ± 0.72	This work[c]	$1.3^{+1.0}_{-0.6}$	Drake et al. (2011)
$\log L_\star/L_\odot$	1.46 ± 0.04	This work[d]	1.37 ± 0.04	Drake et al. (2011)
distance (pc)	26.41 ± 0.15	van Leeuwen (2007)	–	–

[a]Since Parks et al. (2021) had multiple values reported for the same parameter, we show the averages of the respective parameter here.

[b]Based on the angular radius from this work and the distance from van Leeuwen (2007).

[c]Based on the physical radius from this work and the log g from Drake et al. (2011).

[d]Based on the physical radius from this work and the effective temperature from Drake et al. (2011).

Note. — The observed parameters were optimized through a bootstrap approach with the exception of the rotation period, which was fixed. We take our fixed rotation period parameter directly from the best model in SIMTOI.

3.4 Comparisons to Previous Work

3.4.1 *SURFING vs ROTIR Imaging*

We compare images made independently from ROTIR to another 3D image reconstruction code called SURFace imagING (SURFING) in Figure 3.8. SURFING is a Monte Carlo based 3D imaging code written in IDL specifically written for imaging spheroids (see Roettenbacher et al. 2016b). Overall, there is a good agreement between the two 3D imaging methods. Since we are only focusing on the imaging comparison aspect for these two codes, we see that the spot locations and contrast between the two are very similar, with a few minor differences, as shown in Figures 3.5 and 3.8.

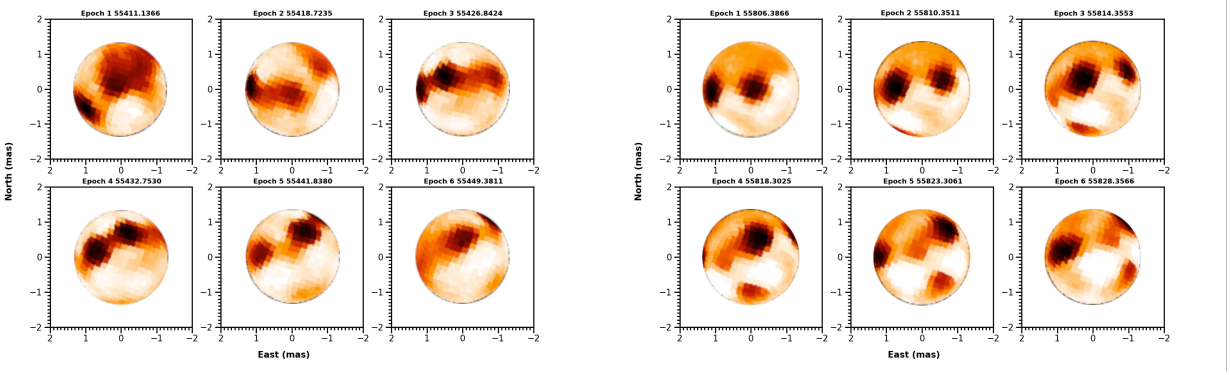

Figure 3.8 Temperature maps of λ Andromedae in 2010 (left) and 2011 (right) using SURFING code. The 2010 temperature maps were made by using two different consecutive nights and merging the data as one night. We find that this does not largely affect the results of the imaging since the rotation made from two consecutive nights only span $\sim$2% of the rotation period.

Images from both codes show that the spots on λ And from both epochs seem to favor certain latitudes and are mostly concentrated in the northern hemisphere. For both the 2010 and 2011 epochs, we find that most of the spots are centered around $+20^\circ$ latitude. These spot concentrations to a certain latitude are consistent with the interferometric images shown in Roettenbacher et al. (2016b) of ζ Andromedae, another RS CVn variable. The absence

of symmetrical spots on active latitudes as observed on the Sun is evidence that λ And may not have a solar-like dynamo.

3.4.2 *Inclination Disagreement*

Our results of this work largely agree to that of Parks et al. (2021) with the inclination of λ And being the only disagreement. Parks et al. (2021) used a combination of a genetic algorithm (Charbonneau 1995) and the Nelder-Mead Simplex method (Nelder & Mead 1965; Box 1965; Richardson & Kuester 1973), in order to make individual models for each night of data. Each surface model calculates an angular diameter, limb-darkening coefficient based on the power law, a starspot covering factor, starspot latitude, starspot longitude, and starspot intensity ratio for λ And. Once all the models were made, Parks et al. (2021) traced each starspot on the surface for each epoch. Ellipse fits to starspot positions were calculated, and an average computed position angle and inclination angle were made from these ellipse fits for each year.

Parks et al. (2021) reported that the inclination of primary from their 2010 and 2011 data is $75 \pm 5.0^\circ$ and $66.4 \pm 8.0^\circ$, for each respective year, giving an overall average of $70.35 \pm 6.7^\circ$ while we report an inclination of $85.63 \pm 2.32^\circ$. We believe that our calculations from this work are accurate for several reasons. The initial SIMTOI calculations were done with a global search with no restrictions in parameter space, including inclination. The resulting parameters obtain from SIMTOI were then used in ROTIR with a sufficient range that included the inclination value from Parks et al. (2021). If the value for our inclination were incorrect and actually leaned towards this previous value, the resulting bootstrap method would reflect it by converging on the lower bounds of our parameter space using our bootstraps. In addition, the work by Parks et al. (2021) relied on independent models for each night and tied them together to form an analysis while we use all the data of each epoch together to form one image.

3.5 Beyond Solid Rotation Imaging

3.5.1 *Simulating Differential Rotation*

In our Figures 3.4 - 3.8 using SIMTOI/ROTIR, SURFING, and in Parks et al. (2021), all imaging has been performed assuming that the star is rotating as a solid body; however, we attempt to estimate differential rotation through our data. Henry et al. (1995) studied photometry of λ And over 14 years and found evidence of shear across the surface. In order to see if we are able to detect any differential rotation with our interferometric data, we simulate starspots on a star with a low differential rotation coefficient and a low temperature gradient on the surface and have the spot move across a few days with the same period as λ And. Then we do a cross-correlation for each latitude on the star and see if there is any deviation from zero.

Our simulations show two different scenarios. The first simulation presents a highly unrealistic starspot that is two pixels wide in longitude and spanning throughout all latitudes from pole to pole. Our second simulation shows two circular starspots that are 5 pixels in radius at $+45°$ and $-45°$ latitude (with respect to the equator) and at $135°$ longitude. We presents our simulations of a simple star with similar parameters as λ And using differential rotation coefficient from Henry et al. (1995) of k = 0.04, which corresponds to differential angular velocity ($\Delta\Omega$) of 0.26, in Figure 3.9.

3.5.2 *Testing Differential Rotation on λ Andromedae*

We apply the same cross-correlation method for the 2011 data set and calculate the deviations. Since the goal is to detect any shear as evidence for differential rotation, we reconstruct an individual temperature map for each observation date from the 2011 epoch but initialize with the temperature map obtained from Figure 3.4 and show our results in Figure 3.10.

We find that we are unable to detect any differential rotation with our data due to three reasons. First, our data does not span an entire rotation, therefore we are not able to compare

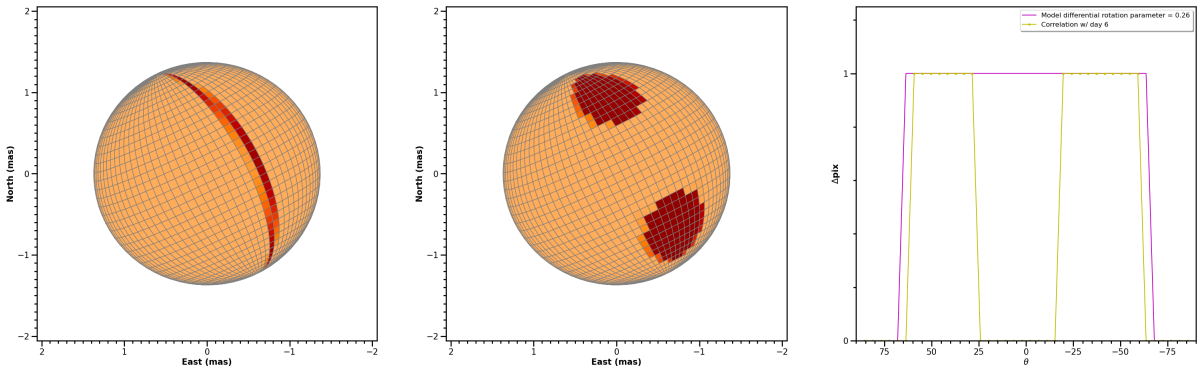

Figure 3.9 We show simulations of differential rotation by doing a correlation using the unrealistic latitudinal starspot (left) and two starspots (middle) of a fake star with the same parameters of λ Andromedae within the 2011 epoch (with the exception of the temperature map). The differential rotation coefficient we use here is $\Delta\Omega$ of 0.26 from Henry et al. (1995). The plot (right) shows the number of pixels that have shifted in respect to the longitude after subtracting off the total shift of a spot. The pink line at this coefficient represents the unrealistic starspot change in pixels, while the yellow line shows the two starspots change in pixels as a function of the longitude. We choose to compare the first and last observations within the 2011 epoch to show the maximum amount of correlation.

the same spots from the previous rotation. Second, λ And is a very slow rotator, so we do not have enough resolution to detect any small amounts of differential rotation if differential rotation truly exists on λ And. In fact, the large-scale magnetic spots on λ And may not be able to be used to measure any real surface differential rotation based on its dynamo. Korhonen & Elstner (2011) states that surface differential rotation can only be recovered by observing the spot motion of small spots, unlike λ And's large-scale magnetic spot structure. Third, the amount of square visibilities and closure phases for each observation are sparse for most observations.

3.6 Imaging Beyond the Primary

3.6.1 *Updated Orbital Parameters and Secondary Parameters*

Using the updated parameters from the primary star in λ And in this work, the mass ratio from Donati et al. (1995) and Kepler's Third Law, we are now able to calculate the mass of

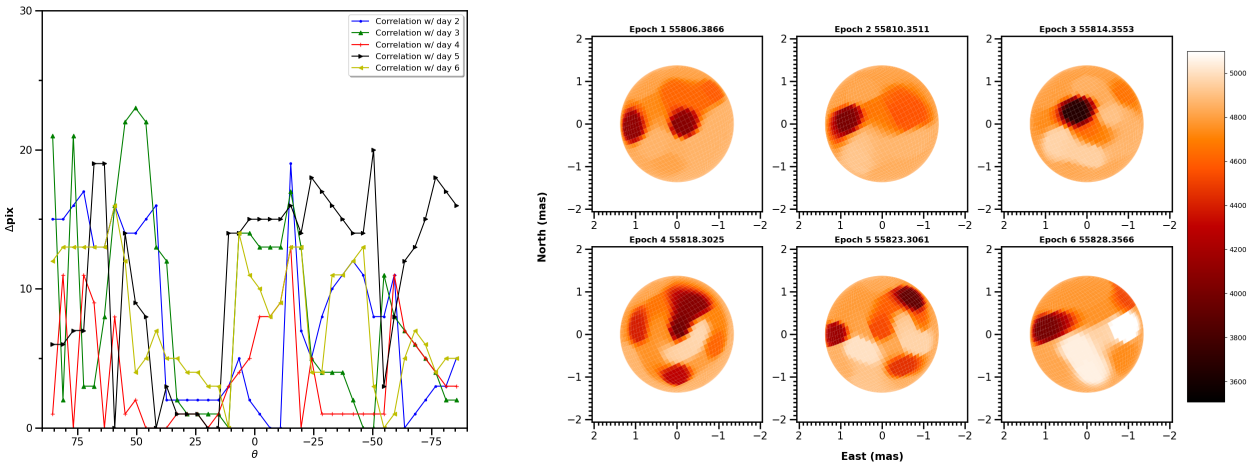

Figure 3.10 The plot shown here (left) is similar to that of Figure 3.9 but with the actual λ Andromedae data. The different symbols denote correlations of temperature maps compared to the first observation of λ Andromedae in the 2011 epoch. The individual temperature maps for each observation date in 2011 (right) were constructed using the original temperature map from Figure 3.4. These maps reflect the difficulty in searching for shear at the one pixel level since each map is slightly different compared to the previous observation and results in no visible correlation.

the secondary and the semi-major axis of the binary system. We calculate that the mass for the companion star is $0.15^{+0.09}_{-0.05}$ $M_{\odot}$ given that the calculated semi-major axis is 6.12 mas.

3.6.2 *The Search for the Secondary*

We begin our search for the companion by calculating estimates on the luminosity ratio and angular size of the secondary to narrow down our search. For the luminosity ratio, we used a mass-luminosity relation for each corresponding star in our system ($L_2/L_1 = 0.23(M_2^{2.3}/M_1^4)$) and calculated to be approximately $L_2/L_1 = 0.00121$. If we assume that the H-band flux ratio is the same as the luminosity ratio of the two stars and using the H-band magnitude of the primary 1.40 mag (Ducati 2002), this would correspond to an estimated H-band magnitude of 8.7 mag for the secondary. This is slightly beyond MIRC's magnitude limit and not likely to be detected. Furthermore, the magnitude difference between the primary and the secondary (ΔH = 7.3 mag) are past MIRC's magnitude contrast difference, as proven by the visibility and closure phase modulation method from the study in Gallenne et al. (2015). Regardless,

we still investigate the possibility of detection. In order to calculate the estimated angular size of the secondary, we first calculate the physical size by using the mass-radius relation ($R = 0.0753 + 0.7009M + 0.2356M^2$) developed by Maldonado et al. (2015) for low-mass stars. Given that the calculated physical radius is 0.19 $R_\odot$, we find that the estimated angular radius to be 0.03 mas.

Now that we have an estimation of the angular size and flux ratio, we do a grid search in right ascension and declination over a 10 mas distance from the primary star with a 0.1 mas step size for every night in the 2011 epoch. This approach is similar to that adopted in Baron et al. (2012) and CANDID (Gallenne et al. 2015) with the difference that the primary is using the model visibilities obtained during image reconstruction. We model binary visibilities and vary both the brightness ratio and the angular radius for the secondary using NLopt for each section of the grid. We restrict the parameter space for the angular radius to [0.0, 1.0] mas while restricting the flux ratio (secondary/primary flux) for the system from [0.0, 0.2].

While we do find that the average flux ratio using the 2011 data set of 0.00213 ± 0.00116 is within the theoretical estimated value, we find two major reasons for believing that we were not able to find the secondary companion. First, the average angular radius found by using the 2011 data is 0.602 ± 0.356 mas, largely inconsistent with our estimation using mass-radius relation for low-mass stars. Our errors for both the flux ratio of the system and the angular size of the secondary were calculated by taking the standard deviation from all the values from all the nights. The values of angular radius for an individual night were also seen to hit a boundary condition (either 0 mas or 1 mas), thus assessing that the calculated values are incorrect. Second, the best fit right ascension and declination positions for each night in the 2011 data set were positioned in a random assortment on the grid space with no clear indication of a circular or elliptical orbit (see Figure 3.11). This confirms our earlier assumption that the secondary would be undetectable as it is beyond MIRC's magnitude limit.

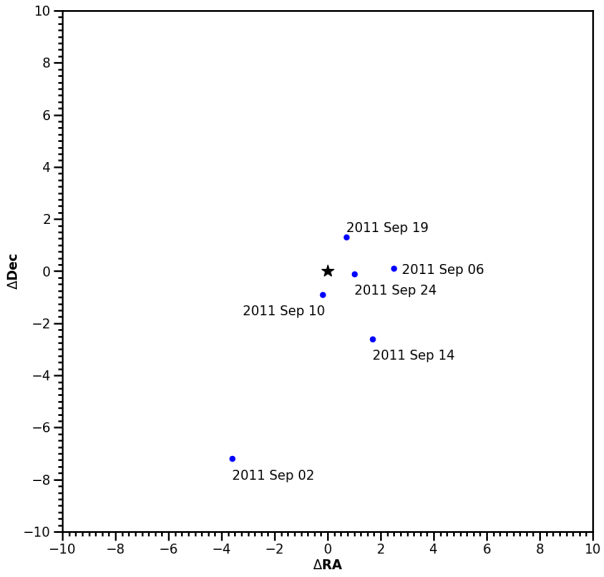

Figure 3.11 We show the results of the grid search in right ascension and declination for each night of data in the 2011 epoch. Each night is labeled with a blue dot and the primary is centered in the middle at (0,0) as a black star.

Another reason that we may not be able to find the secondary for λ And could be due to lack of (u, v) coverage for each individual night in the 2011 epoch data set. For this reason, we proceed to not use the 2010 data set to find the secondary as those observations were taken with two different sets of 4T observations in a given night and as a result do not in better (u, v) coverage compared to the 2011 data set.

3.7 Discussion of Imaging Results

Our imaging results compared to that of Parks et al. (2021) provides new insight to the evolution of spots on λ And. Since the spots for both epochs appear to favor the northern hemisphere, this is indicative that λ And has a non-solar dynamo. There is evidence on other stars that concentration of spots to certain latitudes or longitudes, most noticeably on the other interferometrically imaged RS CVn variable ζ Andromedae (Roettenbacher et al. 2016b). The formation of large spot formation also provides insight into its stellar cycle, which could potentially lead to confirming its 11.4 year cycle obtained from photometry.

Chapter 4
RAPID ROTATORS

Previous interferometric imaging campaigns obtained detailed surface images of several rapid rotators but suffered from limited analysis on limb-darkening or had limited (u, v) coverage. A better understanding of limb-darkening and gravity darkening would provide an improved understanding of the surface temperature distributions of rapid rotators. This ultimately provides a deeper understanding of the physical characteristics of the exterior and interior of rapidly rotating stars. The work here aims to present comparisons between the two-dimensional theoretical radiative transfer model ESTER, surface temperature distribution laws, and surface imaging. We further aim to display the robust imaging capabilities of ROTIR and apply it to the rapidly rotating star Alderamin.

4.1 Target Selection

The catalog within van Belle (2012) lists several rapid rotator candidates that can be observed and potentially imaged with optical interferometry. We impose several limitations for the next candidates to observe, specifically at the CHARA Array. Our selection criterion aims to find rapid rotators with an angular size of at least 1.5 mas (polar or equatorial angular size) and stars with $H < 6$ mag, limitations which are based on the imaging resolution limit of CHARA and the MIRC-X instrumental magnitude limit. Furthermore, we limit our selection to stars with a declination above $-10°$, based on CHARA's geographic location.

Table 4.1. CHARA Array Observations for Alderamin

UT date	Average MJD	Baselines	Number of $\|V\|^2$ points	Number of Closure Phases	Calibrators
2019 Aug 09	58704.52	E1-W2-W1-E2	720	464	16 Cep
2019 Aug 10 (bracket 1)	58705.35	E1-W2-W1-S2-E2	1202	1230	HD 195820, 16 Cep
2019 Aug 10 (bracket 2)	58705.35	E1-W2-W1-S2-E2	1227	1239	16 Cep
2019 Aug 10 (bracket 3)	58705.35	E1-W2-W1-S2-E2	1231	1237	16 Cep, HD 210855
2019 Aug 11	58706.34	E1-W2-W1-S2-E2	1191	1200	16 Cep, HD 210855
2019 Aug 12	58707.48	E1-W2-W1-E2	720	480	16 Cep, HD 210855

Note. — Here we list the UT date, the average modified Julian date of the night of observation, the baselines used in their corresponding configuration, the number of useful squared visibility points obtained for the night, the number of useful closure phase points obtained for the night, and the calibrator stars that were used for each corresponding night.

Table 4.2. Calibrators for Alderamin and Caph

HD Number	Calibrator Name	Calibrator Size (mas)	Source
HD 195820		0.751 ± 0.058	SearchCal (Bonneau et al. 2006)
HD 209369	16 Cep	0.621 ± 0.018	Ligi et al. (2016)
HD 210855		0.594 ± 0.058	SearchCal (Bonneau et al. 2006)

4.2 Observations, Data Reduction, and Calibration

We revisit the previously imaged rapid rotator Alderamin using the CHARA Array with the MIRC-X instrument. The MIRC-X instrument (Kraus et al. 2018; Anugu et al. 2018) is an upgraded version of the original MIRC instrument and provides data with better signal-to-noise thanks to an upgraded camera and optics upgrades. The observations were done in the grism mode (R = 190), which contains approximately 36 spectral channels. Alderamin only benefited from the simultaneous use of five telescopes due to its high declination. The data used in this manuscript are listed in Table 4.1.

The data were reduced using the official Python MIRC-X reduction pipeline (Le Bouquin 2020). The reduction pipeline is divided into three major steps: a pre-processing step, a real-time signal step, and a calibration step (as detailed in Anugu et al. 2020). During the pre-processing step, the pipeline first associates which data files are target data and shutters. It proceeds to do background subtraction to remove any instrumental noise and remove bad pixels, flat-fielding to correct for any pixel-to-pixel variation, and spectral calibration. During the real-time signal step, the flux of each beam is used in comparison with the fringes to ultimately extract the true flux of each fringe in order to compute raw visibilities. The final calibration uses calibrator stars to correct for the atmospheric coherence time and optical changes in the beam path, thus computing the observed visibilities. The stars used for the calibrating step are presented in Table 4.2.

We apply the same corrections as Monnier et al. (2012) after the MIRC-X pipeline reductions in order to better account for systematic errors. Two types of systematic error corrections were used for the squared visibilities: a 6.6% multiplicative error correction was used in association with the transfer function and a 2×10^{-4} additive error correction was used in association with correcting biases at low fringe or bispectrum amplitude. A 10% multiplicative error correction and 1×10^{-5} additive error correction was used for the triple amplitudes. Finally, a 1° error floor was used for the closure phases. We show the squared visibilities and closure phases from data obtained in August 2019 for Alderamin and Caph in Figure 4.1.

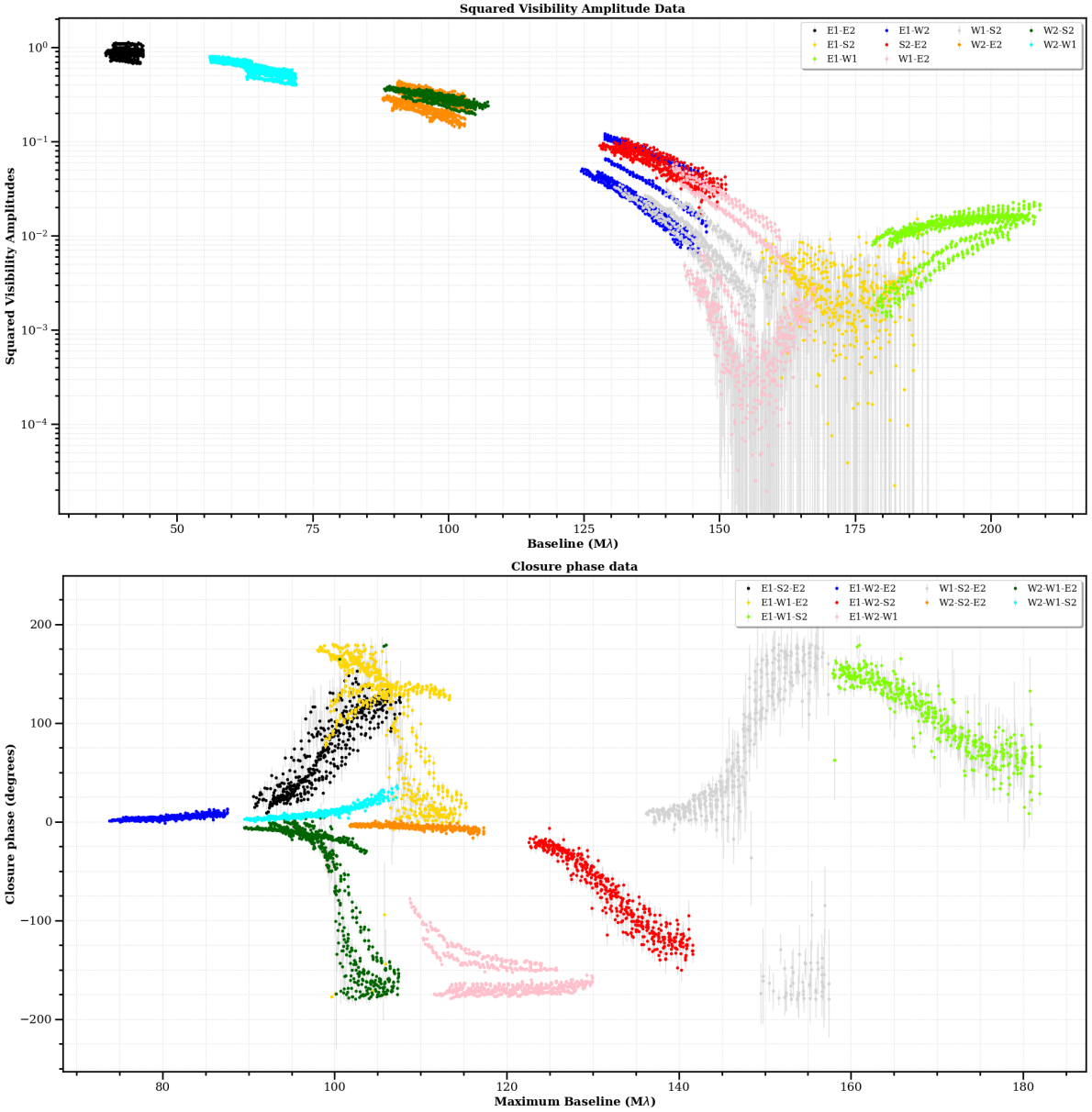

Figure 4.1 Top: $|V|^2$ points are plotted against the baseline length (in Mλ) for a given baseline pair for all the data of Alderamin taken in August 2019. Bottom: Closure phase points are plotted against the baseline length (in Mλ) for the given baseline trio for the same data.

4.3 SIMTOI Modeling of Alderamin

We follow a similar procedure to that outlined in Section 3.2. We use SIMTOI and the MultiNest algorithm to obtain a model that solves for the rotation axis (inclination and position angle), rotation period, polar angular radius, fraction of critical angular velocity, gravity darkening coefficient β (from Equation 1.40), and the coefficient of the power limb-darkening law. The priors used for each model were given a wider distribution for some parameters or a more constrained distribution for more established parameters and were based on prior interferometric studies on the systems.

We use our interferometric data from Alderamin and use it in SIMTOI by making a Roche model rendered on a 64 $\times$ 64 image with a 0.05 mas per pixel resolution. To account for the discrepancies between in van Belle et al. (2006) and Zhao et al. (2009) for Alderamin's analysis, we only allow a large range for the inclination (as other parameters seem to agree with each other). The priors used in MultiNest for Alderamin are restricted to a specific range and are as follows: [0.63, 0.69] mas for the polar angular radius, [0.8, 0.99] for the fraction of the critical angular velocity, [0.08, 0.25] for the gravity darkening coefficient, [0.0, 0.25] for the limb-darkening coefficient, [45.0, 90.0] degrees for inclination, [-180.0, -170.0] degrees for position angle, and [11, 13] hours for the rotation period. We show the results of each MultiNest run in Table 4.3.

4.4 Applying ROTIR to Alderamin

We apply the same general methodology of Section 3.3 to Alderamin. We start with the parameters obtained from SIMTOI to make temperature maps (using OptimPack) and apply the l-curve method, ultimately choosing a hyperparameter value of $\mu = 0.05$. We use 80 pixels around each latitude and 40 pixels across each longitude for a total of 3200 pixels on the surface of each star.

Table 4.3. SIMTOI Results for Alderamin

Object	Importance Nested Sampling ($\ln Z$)	χ^2_ν
Alderamin	50671.778799	2.774372
Physical parameters	**Solution**	
$R_{\star,\mathrm{p}}$ (mas)	0.666	
Limb-darkening coefficient	0.001	
ω_c	0.945	
β	0.179	
Inclination (deg)	76.55	
Position Angle (deg)	-176.91	
Rotation Period (hours)	11.76	

Note. — No error bars are calculated since the models from SIMTOI using Multinest does not currently generate reliable error bars. We rely on the imaging results for more precise measurements and calculation of errors.

4.4.1 *Alderamin Imaging*

We apply a Roche object geometry to Alderamin and use the bootstrap method in order to find its physical parameters and their corresponding errors. We apply 30 bootstrap iterations to solve for seven parameters: polar angular radius, the limb-darkening coefficient, fraction of the critical angular velocity, the gravity darkening coefficient, inclination, position angle, and rotation period. We use the Nelder-Mead Simplex method within NLopt and OptimPack to obtain these final parameters. We restrain NLopt within the following bounds for each given parameter: [0.63, 0.69] mas for the polar angular radius, [0.0, 0.02] for the limb-darkening coefficient, [0.85, 0.99] for the fraction of the critical angular velocity, [0.08, 0.25] for the gravity darkening coefficient, [45.0, 90.0] degrees for inclination, [-180.0, -170.0] degrees for position angle, and [11, 13] hours for the rotation period. While we are limited again to a small amount of bootstraps due to large computation time, the errors incorporate to first degree any systematic and statistical errors within the data. We show the results of our

bootstraps in Figure 4.3 and the final parameters of Alderamin in Table 4.4. The final temperature map and image of Alderamin is shown in Figure 4.2.

The physical parameters calculated for the rapid rotator Alderamin in Table 4.4 are more complex than a spherical star. The equatorial angular radius for Alderamin was calculated on the critical angular velocity and is ultimately reliant on Equation 2.3. The physical radii are based on the physical distance from van Leeuwen (2007) and the effective temperatures are obtained from the imaging results where the polar effective temperature was based on Zhao et al. (2009) as a starting temperature. The equatorial velocity is calculated from our calculation of the physical polar radius, the physical equatorial radius, and the rotation period. The oblateness mass here was calculated using our physical polar and equatorial radii, rotation period, and the fraction of the critical angular velocity values.

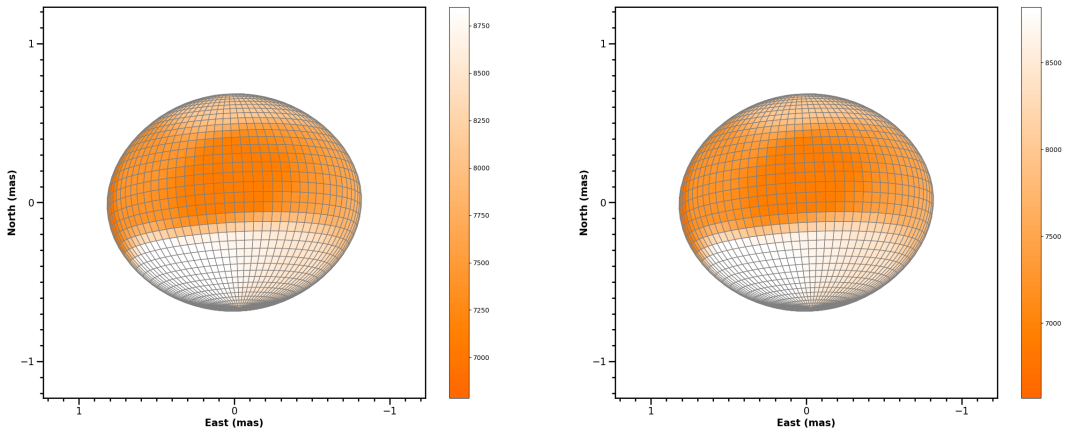

Figure 4.2 We show the surface temperature profile (left) and an image (right) of Alderamin. The temperature map is in Kelvin while the image is displayed with relative intensity to the given limb-darkening. We note that the intensity image does not deviate largely from the temperature map since our results favored a low limb-darkening coefficient.

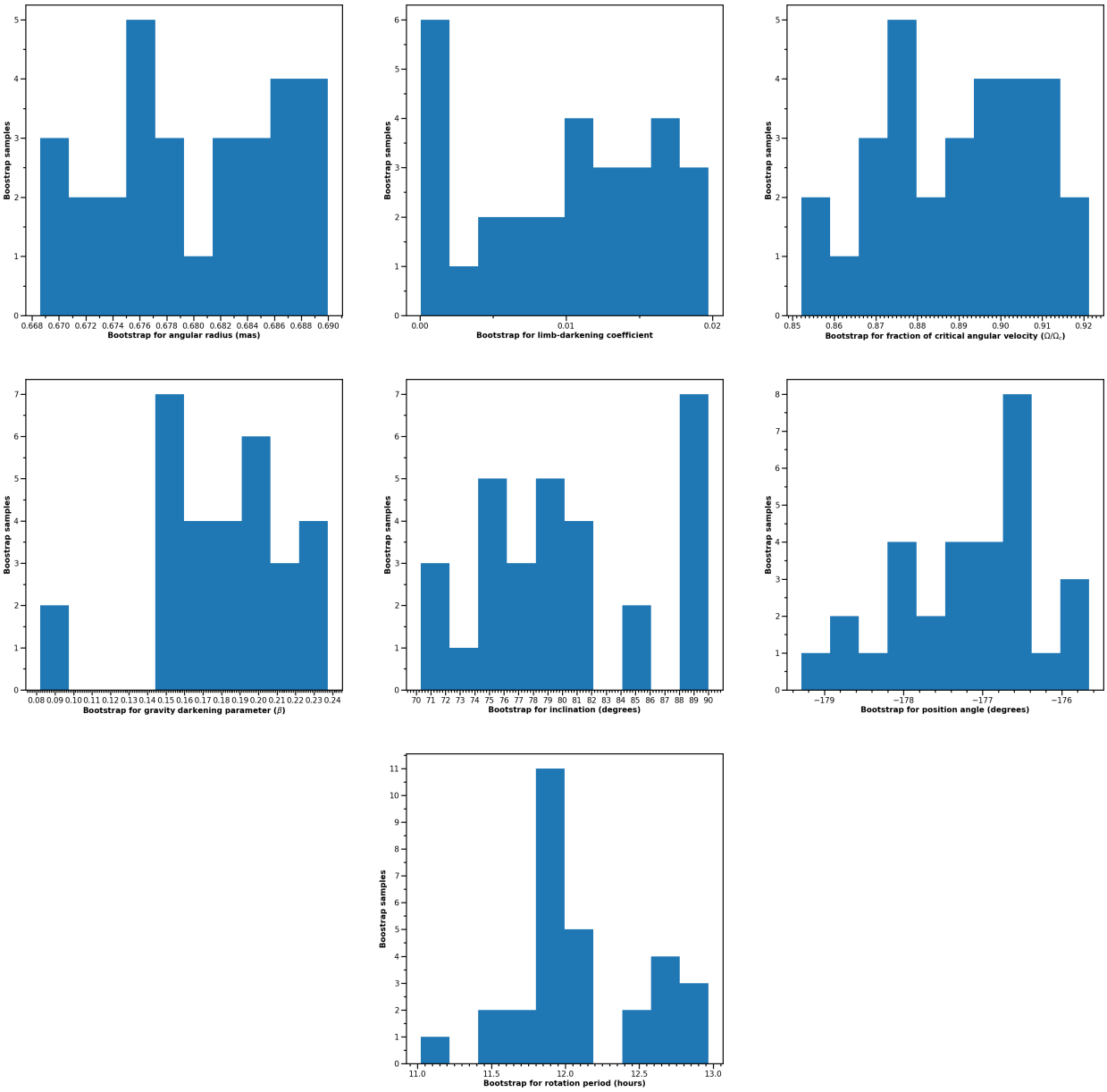

Figure 4.3 We show the results of using the bootstrap method varying angular radius, the limb-darkening coefficient, fraction of the critical angular velocity, the gravity darkening parameter, inclination, and position angle. We use 30 bootstraps in order to calculate the final parameters of Alderamin and bin them into 10 different bins. The x-axis here shows the range of the parameters from all the bootstraps and the y-axis show the number of bootstraps within each bin. While we plot calculated values for each bootstrap, we note that that the full range for each parameter are the following: [0.63, 0.69] mas for the polar angular radius, [0.0, 0.02] for the limb-darkening coefficient, [0.85, 0.99] for the fraction of the critical angular velocity, [0.08, 0.25] for the gravity darkening coefficient, [45.0, 90.0] degrees for inclination, [-180.0, -170.0] degrees for position angle, and [11, 13] hours for the rotation period. The final parameters are calculated from taking the average of each respective parameter with their associated errors calculated from the standard deviation of the bootstrap results.

Table 4.4. Final Alderamin Parameters

Observed Parameters	Value	Source	Values from Literature	Literature Reference
$R_{\star,\mathrm{p}}$ (mas)	0.680 ± 0.006	This work	$0.6753^{+0.0119}_{-0.0135}$	van Belle et al. (2006)
			0.672 ± 0.034	Zhao et al. (2009)
$R_{\star,\mathrm{e}}$ (mas)	0.820 ± 0.014	This work	$0.8767^{+0.0293}_{-0.0183}$	van Belle et al. (2006)
			0.852 ± 0.035	Zhao et al. (2009)
Limb-darkening coefficient	0.010 ± 0.006	This work	–	–
ω_c	0.891 ± 0.018	This work	$0.9585^{+0.0197}_{-0.0116}$	van Belle et al. (2006)
			0.941 ± 0.020	Zhao et al. (2009)
β	0.181 ± 0.037	This work	$0.084^{+0.026}_{-0.049}$	van Belle et al. (2006)
			0.216 ± 0.021	Zhao et al. (2009)
Inclination (deg)	80.35 ± 6.15	This work	$88.2^{+1.8}_{-13.3}$	van Belle et al. (2006)
			55.70 ± 6.23	Zhao et al. (2009)
Position Angle (deg)	-177.20 ± 0.87	This work	$17.2^{+3.2}_{-4.3}$	van Belle et al. (2006)
			-178.84 ± 4.28	Zhao et al. (2009)
Rotation Period (hours)	12.09 ± 0.47	This work	12.11 ± 0.26	van Belle et al. (2006)
Physical parameters				
$R_{\star,\mathrm{p}}$ ($R_\odot$)	2.199 ± 0.021	This work	2.175 ± 0.046	van Belle et al. (2006)

Table 4.4 (cont'd)

Observed Parameters	Value	Source	Values from Literature	Literature Reference
			2.162 ± 0.036	Zhao et al. (2009)
$R_{\star,\mathrm{e}}$ ($R_\odot$)	2.652 ± 0.046	This work	2.823 ± 0.097	van Belle et al. (2006)
			2.740 ± 0.044	Zhao et al. (2009)
$T_{\mathrm{eff,p}}$ (K)	8849 ± 300	Zhao et al. (2009) as prior	8440^{+430}_{-700}	van Belle et al. (2006)
			8588 ± 300	Zhao et al. (2009)
$T_{\mathrm{eff,e}}$ (K)	6785 ± 360	This work	~ 7600	van Belle et al. (2006)
			6574 ± 200	Zhao et al. (2009)
v_{e} (km s^{-1})	266 ± 11	This work	283 ± 19	van Belle et al. (2006)
$v \sin i$ (km s^{-1})	263 ± 12	This work	283 ± 19	van Belle et al. (2006)
			265	Abt & Moyd (1973)
			196	Royer et al. (2007)
$M_\star$ ($M_\odot$)	2.39 ± 0.25	This work	2.0 ± 0.15	van Belle et al. (2006), model mass
			1.92 ± 0.04	Zhao et al. (2009), model mass
$L_{\star,\mathrm{bol}}$ ($L_\odot$)	24.2 ± 3.5	This work	18.1 ± 1.8	Zhao et al. (2009)
[Fe/H]	0.09	Gray et al. (2003)	–	–
distance (pc)	15.04 ± 0.02	van Leeuwen (2007)	–	–

Note. — The equatorial angular radius was calculated based on the fraction of the critical angular velocity. The physical polar and equatorial radii are based on our angular measurements from this work and the distance from van Leeuwen (2007). The mass here (the oblateness mass) was calculated based on the rotation period, the equatorial and polar physical radii, the fraction of the critical angular velocity.

4.4.2 *Imaging Analysis*

The imaging results presented are mostly consistent with the SIMTOI priors, with the exception of the angular radius, the limb-darkening coefficient, and the gravity darkening parameter. The model preferred by SIMTOI suggests that Alderamin has very little to no limb-darkening, which is unrealistic since all stars at least exhibit a small amount of limb-darkening. Our imaging results favored a limb-darkening coefficient that is a factor of 10 greater than the SIMTOI model, and as expected, favored a higher angular diameter. The gravity darkening parameter for the imaging is lower than our model, but we believe this could be tied to the adjustment of the limb-darkening coefficient and angular diameter.

Our interferometric image of Alderamin mostly agrees with literature results, with some slight deviations. The ω_c reported from our reconstruction produced a lower break-up velocity compared to van Belle et al. (2006) and Zhao et al. (2009), however our results are in agreement with the Espinosa Lara-Rieutord law (see Section 4.5). Additionally, we find that our β value is again in agreement with the Espinosa Lara-Rieutord law and from Zhao et al. (2009), who reports a slight overestimate of the real value. The inclination value is in agreement with that of van Belle et al. (2006), but is more than 4 standard deviations (4σ) from that in Zhao et al. (2009). Perhaps this is a hint that the true value of the inclination is between that of previous works and within 1σ of our result. The position angle is in partial agreement with that of van Belle et al. (2006) as their first reported value from an ellipsoidal fit was 3° (here the position angle was defined differently than our work as noted by Zhao et al. 2009), but their final Roche model deviated from this value (as shown in Table 4.4). However, our value of position angle is in good agreement with Zhao et al. (2009). We believe these discrepancies could be a consequence of the calibration within data reduction as both squared visibilities and, more importantly, the closure phase is sensitive to the viewing angle of Alderamin. Lastly, our $v \sin i$ is in agreement with van Belle et al. (2006) but remains in partial agreement with spectroscopic results (e.g., Abt & Moyd 1973; Abt & Morrell 1995; Royer et al. 2007) as these results have historically spanned a large range of values.

The mass of Alderamin has been previously calculated through theoretical models and has been found to be approximately two times the mass of the Sun. Our work derives the mass through a different scheme by relying on the star's rotation rate (to obtain the equatorial linear velocity), its physical size, and the fraction of the critical angular velocity. This oblateness mass method has been previously used by Che et al. (2011), has been shown to be within 1σ compared to a mass obtained through theoretical evolutionary codes. Therefore, we believe that our calculated oblateness mass for Alderamin, which value only differs from previous works by $\sim 1.5\sigma$, may be larger than the true value. This may stem from a lower ω_c and rotation period as our oblateness mass calculation is sensitive to small deviations for these parameters.

It is important to note that slightly different distance measurements were used between previous works and what we present here. van Belle et al. (2006) and Zhao et al. (2009) cite the original parallax measurement from Perryman et al. (1997) which obtained a parallax measurement of 66.84 ± 0.49 mas and yielded a distance of 14.96 ± 0.11 pc using the inverse parallax method. We use the updated *Hipparcos* parallax measurement from van Leeuwen (2007) of 66.50 ± 0.11 mas, which yields a distance of 15.04 ± 0.02 pc. This, in turn, shows that the physical polar radius in van Belle et al. (2006) and Zhao et al. (2009) are slightly larger than previously noted and is in better agreement with our value. The physical equatorial radius, as a consequence of a lower break-up velocity and as expected, is further deviated from previous works.

4.5 Comparing Observations to Gravity Darkening Models

The previous imaging campaigns by Monnier et al. (2007), Zhao et al. (2009), and Che et al. (2011) allowed for the gravity darkening parameter to be non-restricted and its value varied from star to star. It was determined by Che et al. (2011) that the best gravity darkening parameter was $\beta = 0.19$ for hotter rapid rotators. Comparing the effective temperature ratios to the fraction of the critical angular velocities of stars, one can see in Figure 4.4

that the Espinosa Lara-Rieutord law is in slightly better agreement with observational work compared to that of a constant $\beta = 0.19$. Specifically, the analysis by Vega in Monnier et al. (2012) showed the concordance model of $\beta = 0.231$ (which used a $v \sin i$ value from spectroscopy as a prior) is in better agreement with the Espinosa Lara-Rieutord law than the $\beta = 0.19$ model. It is also seen in Figure 4.4 that at lower rotation rates, the Espinosa Lara-Rieutord law turns into the standard $\beta = 0.25$ von Zeipel law (as proven within Espinosa Lara & Rieutord 2011). As a result, we aim to calculate a better method in adopting the best gravity darkening parameter for rapid rotators.

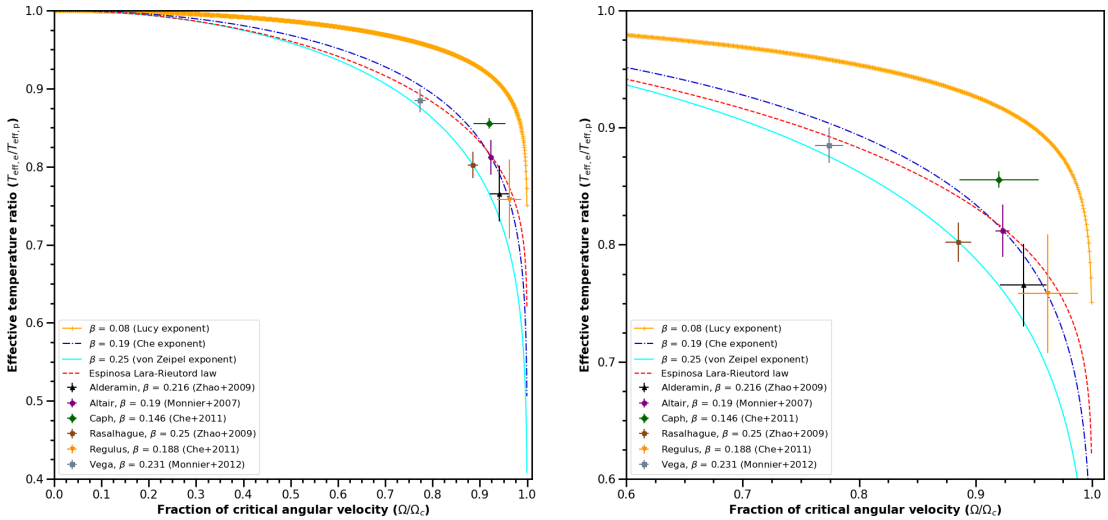

Figure 4.4 Both plots show the effective temperature ratio (equatorial to polar) of stars against different rotation rates for different laws. The standard von Zeipel law (von Zeipel 1924a,b) with $\beta = 0.25$ is plotted in the solid cyan line, the exponent recommended by Lucy (1967) of $\beta = 0.08$ is plotted in orange dashed cross lines, the recommended exponent by Che et al. (2011) of $\beta = 0.19$ is plotted in blue dashed dotted lines, and the Espinosa Lara-Rieutord law (Espinosa Lara & Rieutord 2011) is plotted in red dashed lines. We over plot the empirically derived β values of Altair (Monnier et al. 2007) as shown in the solid purple circle, Alderamin (Zhao et al. 2009) as shown in the black upwards triangle, Rasalhague (Zhao et al. 2009) as shown in the brown solid "X" symbol, Caph (Che et al. 2011) as shown in the solid green diamond, Regulus (Che et al. 2011) as shown in the solid downwards triangle, and Vega (Monnier et al. 2012) as shown in the solid gray square. The left plot show the full range of rotation, while right plot shows a zoomed in version of the left plot for detail.

To start calculating a new method to determine the best β, we start by using the temperature difference between the pole and the equator, as formulated by Aufdenberg et al. (2006),

$$T_{\rm eff,p} - T_{\rm eff,e} = T_{\rm eff,p}\left[1 - \left(\frac{\omega_c^2}{\eta^2} - \frac{8}{27}\eta\omega_c\right)^{\beta}\right] \tag{4.1}$$

where

$$\eta = 3\cos\left[\frac{\pi + \cos^{-1}(\omega_c)}{3}\right]. \tag{4.2}$$

We can rearrange Equation 4.1 as follows

$$\frac{T_{\rm eff,e}}{T_{\rm eff,p}} = \left(\frac{\omega_c^2}{\eta^2} - \frac{8}{27}\eta\omega_c\right)^{\beta} \tag{4.3}$$

as it allows us to start making a more direct comparison between the general von Zeipel law and the Espinosa Lara-Rieutord law. Using the solution from Equation 2.23 in Equation 2.19, we can form a solution for the effective temperature at the equator using the Espinosa Lara-Rieutord law,

$$T_{\rm eff,e} = \left(\frac{L_\star}{4\pi\sigma R_{\rm e}^2}\right)^{1/4}\left(1-\omega_k^2\right)^{1/12}. \tag{4.4}$$

Together using Equations 2.24 and 4.4, we make another comparison to the effective temperatures between the equator and the pole (Espinosa Lara & Rieutord 2011) as

$$\frac{T_{\rm eff,e}}{T_{\rm eff,p}} = \sqrt{\frac{2}{2+\omega_k^2}}\left(1-\omega_k^2\right)^{1/12}\exp\left(-\frac{4}{3}\frac{\omega_k^2}{\left(2+\omega_k^2\right)^3}\right). \tag{4.5}$$

Using both Equations 4.3 and 4.5, we can formulate a solution for the gravity darkening coefficient β dependent on the Espinosa Lara-Rieutord law as

$$\sqrt{\frac{2}{2+\omega_k^2}}\left(1-\omega_k^2\right)^{1/12}\exp\left(-\frac{4}{3}\frac{\omega_k^2}{\left(2+\omega_k^2\right)^3}\right) = \left(\frac{\omega_c^2}{\eta^2} - \frac{8}{27}\eta\omega_c\right)^{\beta} \tag{4.6}$$

Table 4.5. Recommended Values for β Based on Espinosa Lara-Rieutord Law

Object	ω_c (Literature value)	β (Literature value)	Recommended value for β	Literature Reference
Alderamin (α Cep)	0.941 ± 0.020	0.216 ± 0.021	0.183 ± 0.013	Zhao et al. (2009)
	0.891 ± 0.018	0.181 ± 0.037	0.195 ± 0.010	This work
Altair (α Aql)	0.923 ± 0.006	0.190 ± 0.012	0.189 ± 0.004	Monnier et al. (2007)
Caph (β Cas)	$0.920^{+0.024}_{-0.034}$	$0.146^{+0.013}_{-0.007}$	0.189 ± 0.020	Che et al. (2011)
Rasalhague (α Oph)	0.885 ± 0.011	0.25 (fixed)	0.197 ± 0.006	Zhao et al. (2009)
Regulus (α Leo)	$0.962^{+0.014}_{-0.026}$	$0.188^{+0.012}_{-0.029}$	0.175 ± 0.020	Che et al. (2011)
Vega (α Lyr)	0.774 ± 0.012	0.231 ± 0.028	0.218 ± 0.007	Monnier et al. (2012)

Note. — The errors for recommended value for β were derived through error propagation using the literature values of ω_c and its corresponding errors.

and after a simple rearrangement

$$\beta = \frac{\ln\left[\sqrt{\frac{2}{2+\omega_k^2}}\left(1-\omega_k^2\right)^{1/12}\exp\left(-\frac{4}{3}\frac{\omega_k^2}{\left(2+\omega_k^2\right)^3}\right)\right]}{\ln\left[\frac{\omega_c^2}{\eta^2}-\frac{8}{27}\eta\omega_c\right]}. \tag{4.7}$$

This leaves β solely dependent on the fraction of the critical angular velocity (since once can easily convert from ω_k and η to ω_c). We present the relation of Equation 4.7 in Figure 4.5 and list our recommended values of β against the literature values of the gravity darkening parameter in Table 4.5. We suggest that Equation 4.7 be used as a prior for future rapid rotator modeling/image if the fraction of the critical angular velocity is known a priori.

4.6 ESTER Modeling

We compare our empirically derived stellar parameters to those produced from ESTER. The major requirements as inputs for ESTER are the mass of the star and the mass fraction for hydrogen and metals. While there are various choices for which opacities and equations of state within ESTER, we ultimately choose OPAL opacities and equation of state (Rogers et al. 1996) to model both stars. In addition, we estimate that Alderamin is near solar

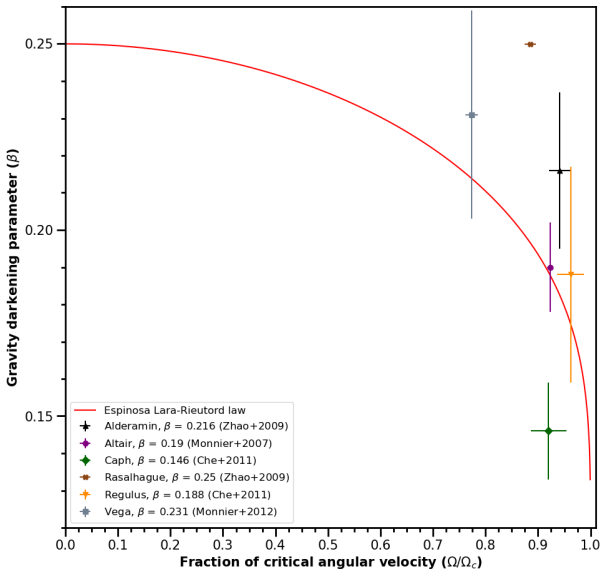

Figure 4.5 We plot the gravity darkening parameter β from the general von Zeipel law as a function of the critical angular velocity for the Espinosa Lara-Rieutord law.

metallicity such that the hydrogen mass fraction is $X = 0.70$ and the metal mass fraction is $Z = 0.02$.

We follow a general procedure for producing a model for Alderamin. First, we compute a homogeneous (one-dimensional) model with the appropriate mass of the star and mass fractions. Then we evolve this homogeneous model by changing the hydrogen content of the core. Finally, we rotate the evolved model to a given break-up velocity. We also follow the same procedure as Espinosa Lara & Rieutord (2013) and modify the mass, Keplerian angular velocity, and the mass fraction of hydrogen in the core until we come across the desired model. The final models, shown in Table 4.6, are chosen when the polar and equatorial radii, polar and equatorial effective temperatures, and the luminosity are close to 1σ of the observational data.

A first approach in finding a preferred ESTER model shows that it favors a 2.06 $M_{\odot}$ star and is approximately 1.5σ lower than our value of the oblateness mass. In order to make the polar and effective temperatures close to that of our images, we modified the angular velocity such that it rotates faster than our imaging results. There are two major deviations

Table 4.6. ESTER Results of Alderamin

Physical Parameters	Observations	Model
$M_\star$ ($M_\odot$)	2.39 ± 0.25	2.06
$X_{\rm core}/X_{\rm env}$		0.40
ω_k	0.642 ± 0.037	0.710
Corresponding ω_c	0.891 ± 0.018	0.926
$R_{\rm p}$ ($R_\odot$)	2.199 ± 0.021	2.207
$R_{\rm e}$ ($R_\odot$)	2.652 ± 0.046	2.774
$T_{\rm eff,p}$ (K)	8849 ± 300	8836
$T_{\rm eff,e}$ (K)	6785 ± 360	7094
$L_\star$ ($L_\odot$)	24.2 ± 3.5	22.5
$v_{\rm e}$ (km s^{-1})	266 ± 11	267
$P_{\rm p}$ (hours)		12.93
$P_{\rm e}$ (hours)		12.60

from the ESTER model and our imaging results. The first deviation is that the equatorial radius is, similar to the mass, 2σ away from the observational results. However, this is a result of a lower ω_c from our observations. The angular velocity needed within ESTER is higher compared to our results and was needed in order to balance the equatorial radius and the effective temperature values. This second deviation within ESTER model resulted in the angular velocity being 2σ larger than our results, but agree with the value from Zhao et al. (2009) which may indicate that this is closer to the true value of ω_c.

4.7 Discussion of Imaging Parameters

The observations using the upgraded MIRC-X instrument have shown that the imaging of Alderamin is in partial agreement with previous works. However, there are a few caveats that need to be addressed. The data were obtained during a time when MIRC-X was currently going through various upgrades (in 2017 and 2018, see Anugu et al. 2020), thus any observations were taken through an "at-risk" basis. The reduction pipeline has also not been fully developed until very recently (Le Bouquin 2020) and potentially could lead to some issues calibrating the raw visibilities. This will affect the squared visibilities, closure phases, and triple amplitudes that are needed to accurately determine the true nature of

Alderamin. Therefore, a more precise re-examination of our Alderamin data is required as the ω_c highly affects multiple values.

Another important investigation for this work is to distinguish the nature between gravity darkening and limb-darkening. Recent rapid rotator studies (i.e., Monnier et al. 2007; Zhao et al. 2009; Che et al. 2011; Monnier et al. 2012) have applied atmospheric models to account for the limb-darkening of rapid rotators and have been successful in producing their full parameterization, however they do not provide a quantitative measure of the atmospheric limb-darkening. As one of the goals of this work is to make distinct measurements of both the limb-darkening coefficient (using the power-law) and the gravity darkening parameter, we find for Alderamin that there is a tendency towards lower ω_c compared to previous works and a small amount of limb-darkening.

Lastly, if the rotation of a star is known or estimated, then the gravity darkening parameter can be estimated to first degree (from Equation 4.7). A further examination from future imaging or surface temperature variation studies will determine if the Espinosa-Lara Rieutord law provides a reliable estimate of the latitudinal temperature variation for stars.

Chapter 5
FREE-SPACE BEAM PROPAGATION

Our final project in this manuscript slightly deviates from direct interferometric modeling and imaging. As current interferometers have limited (u, v) coverage based on the geographical location of their telescopes, the sparse frequency coverage results in poorer imaging quality. While an interferometric observer can stay on the same object all night, this may not be ideal for objects that are highly variable (i.e., appearance changes temperature or shape within the span of a few days). We describe the initial results of our optical test bench project which aims to simulate open-air beam propagation. The motivation for this section is to lay the groundwork for movable/mobile telescopes at any optical interferometer in the world that can be used actively during a night and ultimately provide greater (u, v) coverage, which will result in better imaging quality. We note that CHARA has since been funded to implement such a system.

5.1 Imaging Simulation of a Movable Telescope

In order to find how effective a moving telescope would be to implement, we make simulations of a seventh telescope at the CHARA Array using OITOOLS. We place this new telescope approximately 370 meters southwest from the center of the Array creating a longer baseline with CHARA's E1 telescope at 579 meters. We simulate that this telescope is moving at a rate of 1.41 meters per minute (2.36 cm per second) directly away from the S1 telescope on a rail system that lets the telescope travel 33.94 meters.

In addition to placing a new telescope, we simulate a star that is 3 mas in diameter with three spots on its surface with varying intensities. The first and largest spot has an intensity difference of 25% compared to the photosphere, the second differs by 50%, and the third and smallest spot differs by 75%. We use the power law for limb-darkening with a coefficient of 0.15. Our simulated observations of this spotted star assume the same right ascension and declination as λ And, with four snapshot observations. Each snapshot integration lasts 21

minutes with data taken every three minutes within a bracket. The start of the four brackets is separated by exactly one hour in time. We present the (u, v) coverage of the current 6 telescope CHARA setup and the new 7 telescope CHARA setup in Figure 5.1. Having a movable telescope allows for a faster sweep of the (u, v) plane for any baselines that are tied to this new telescope, whereas the stationary telescope sample a smaller range of the (u, v) plane.

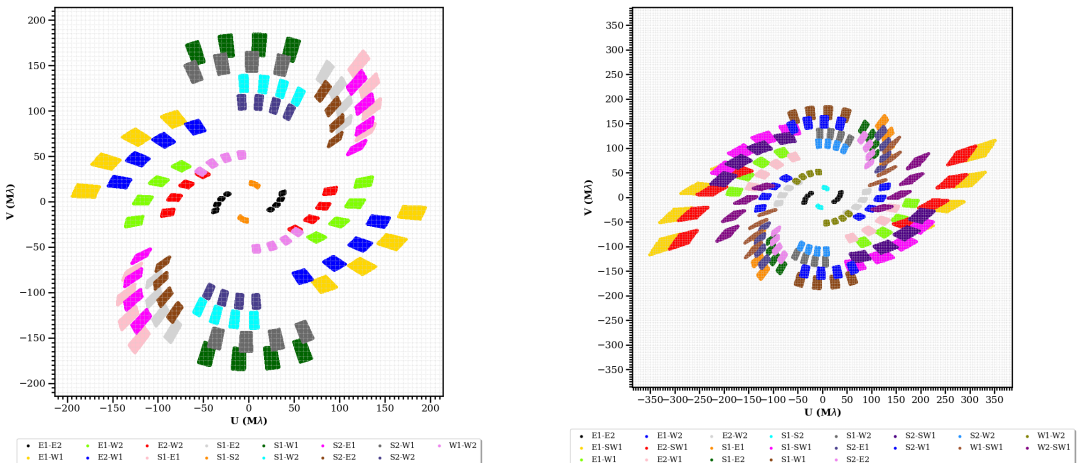

Figure 5.1 Left: (u, v) coverage of CHARA's current 6 telescope configuration with four observing brackets. Right: (u, v) coverage of CHARA with a simulated 7th movable telescope for two observing brackets.

We do 2D image reconstructions of the simulated spotted star with both the current and new simulated CHARA telescope configurations. Our images are 128×128 pixels in size with a pixel size of 0.046875 mas per pixel. Total variation is used as the regularization function and we use l-curve method to find the optimum hyperparameter. The hyperparameters used for the current and new simulated CHARA telescope configuration are 1×10^6 and 2×10^6, respectively. We show the model and reconstructed images along with difference images in Figure 5.2. The difference images show that by having a seventh movable telescope at a larger distance, the smaller spots are starting to be more resolved. This is in contrast to the current CHARA configuration where the smaller spot intensities tend to be more dispersed across the photosphere.

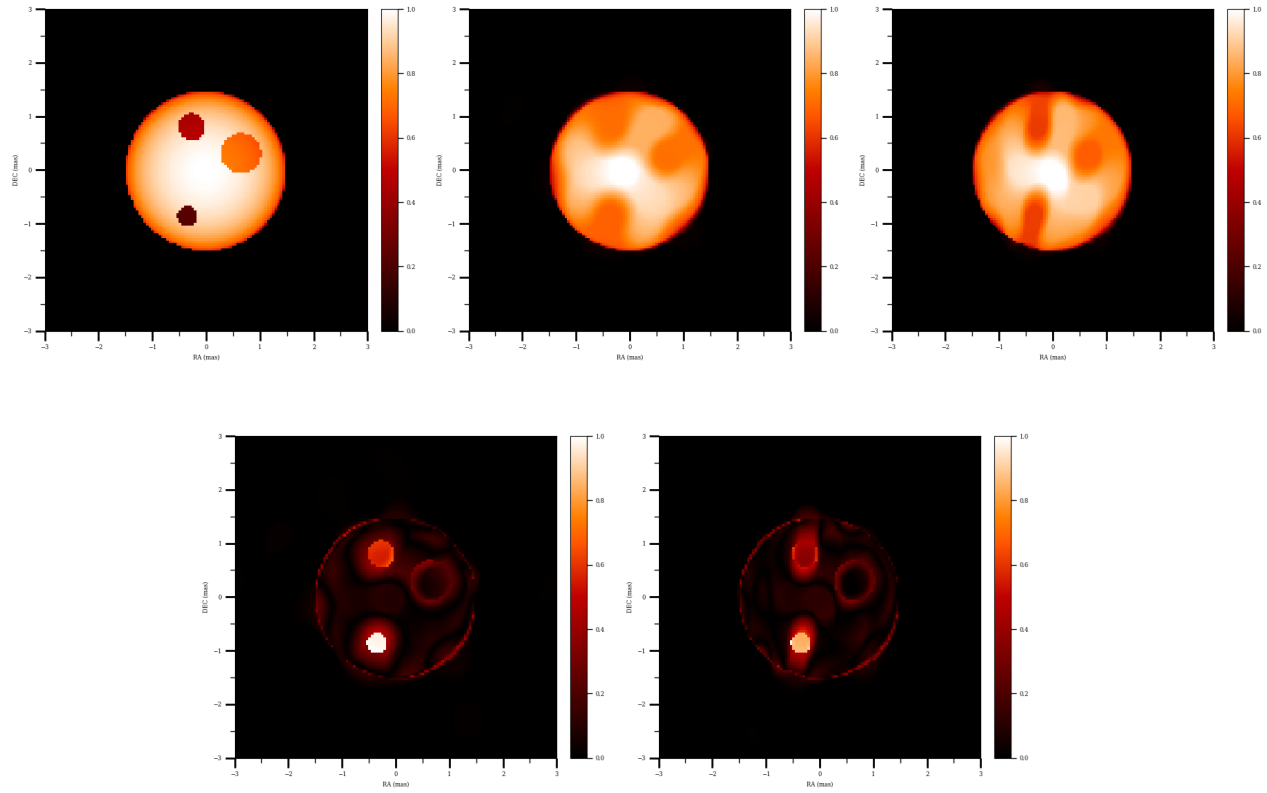

Figure 5.2 Top left: Model of a 3 mas star with three spots where the largest to smallest spots have a 25%, 50%, and 75% difference in intensity compared to the photosphere. Top middle: An image reconstruction of the 3 mas spotted star with CHARA's current 6 telescope configuration. Top right: An image reconstruction of the 3 mas spotted star with the new simulated 7th movable telescope added to the current configuration. Bottom left: Difference image between CHARA 6T and the model. Bottom right: Difference image between CHARA 7T and model.

5.2 Explanation of Instruments

Given our imaging simulations, we move to build a turbulence simulator. The ultimate goal for the following setup is to simulate or replicate atmospheric conditions at a given observing site so that a movable telescope can be placed at any given interferometer, with the potential immediate application at the CHARA Array. For our specific setup, we use a pair of spatial light modulators (SLMs) to mimic atmospheric turbulence and AO systems to correct for the turbulence. Our SLMs from Meadowlark Optics have 1920×1152 elements with a range of 0 to 2π in phase and are calibrated at 635 nm. The adaptive optics system we use consists

of a deformable mirror (DM) and a Shack-Hartmann wavefront sensor (WFS). The DMs we use from ALPAO, specifically the DM-97 (which has 97 actuators, with 11 actuators across its diameter), has a tip/tilt peak-to-valley range of 60 μm, can achieve the best active flat of 7 nm RMS, and has a 13.5 mm pupil diameter. The Shack-Hartmann WFS, also from ALPAO, has a 50 $\times$ 50 lenslet array and can run up to 118 Hz.

5.3 Instrumental Setup

We start with a laser at 637 nm as our light source and expand it out into a collimated beam. The collimated beam feeds two circular apertures producing two beams of a diameter of 10 mm; this is the start of our two telescope interferometric system. The layout for each leg of the interferometer is identical, so we will only describe one leg. We use a 4f system with a magnification of 1 to image the entrance aperture onto an SLM with a magnification of one. We use a half-wave plate right after our laser source to align the linearly polarized light from the laser with the SLM's polarization axis.

After the light is reflected from the SLM, the SLM is imaged onto the DM using another 4f system. Here the beam is expanded from 10 mm to 13 mm to match the 97 actuator DM's active area. After the reflection off of the DM, the beam on each leg is brought through a 50/50 beam splitter where half of the beam's intensity is sent to the Shack-Hartmann WFS. The other half of the intensity is directed to a beam splitter, where we combine the beams from the two legs to form interference fringes. We show the layout of the beam path for our system in Figure 5.3.

5.4 Phase Screens

This project's ultimate goal is to simulate the propagation of light from an astronomical source down to the entrance aperture of a telescope (where the light is corrected with an AO system) before being diverted to travel through a horizontal column of turbulence to a beam combiner facility. Here, the light is corrected with a second AO system before it

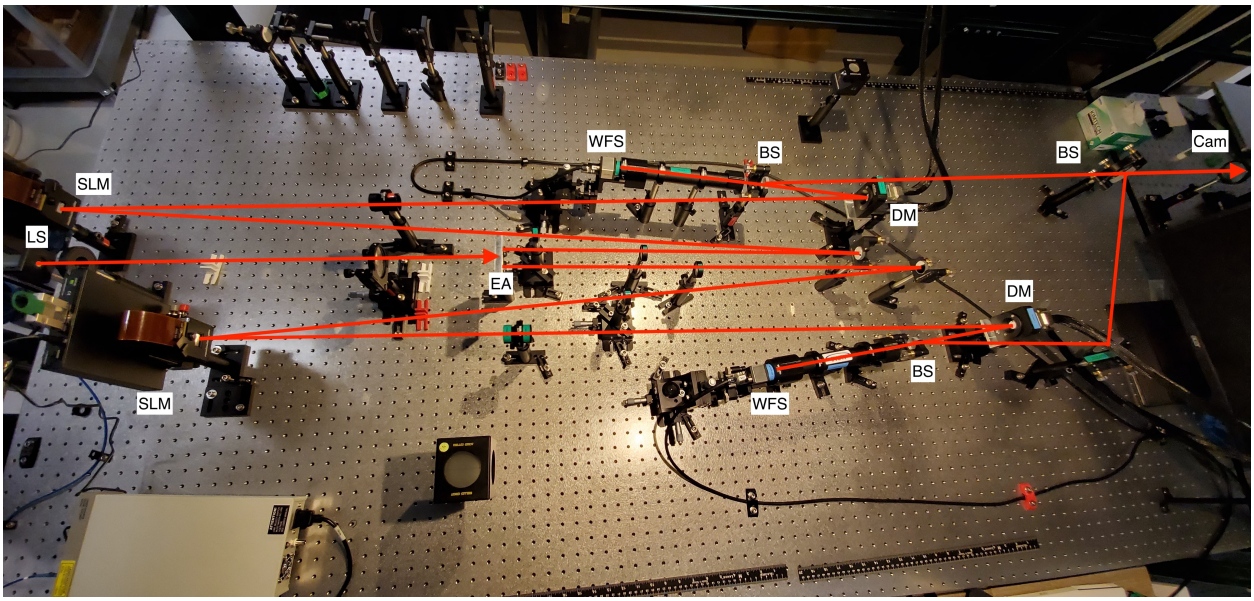

Figure 5.3 We show a top-down view of our optical setup. The red lines reflect the beam path propagated throughout our system until it is ultimately combined at the very end to form fringes. The light path starts on the left (marked as LS) before being "split up" into two beams to simulate two telescopes. We have 3 different 50/50 beam splitters in our setup. The first two beam splitters are put in each leg such that part of the beam is used for the wavefront sensor and the other half is reflected to make fringes on the backend (as indicated by "Cam"). Abbreviations: LS - Laser source, SLM - spatial light modulator, EA - entrance aperture, BS - beam splitter, DM - deformable mirror, Cam - Camera.

is combined with a beam from a second telescope to provide interference fringes. However, in this manuscript, we consider the vertical and horizontal components of turbulence separately. As a test for the experiment, we use Kolmogorov phase screens to simulate vertical turbulence from Earth's atmosphere. We specifically use the split-step beam propagation method (Schmidt 2010) and model the distributed turbulence along the propagation path using a number of discrete, infinitely thin, phase screens. The variation in the phase across each screen represents the fluctuations induced by changes of the refractive index in the atmosphere over the volume of space halfway to adjacent screens.

Our phase screen code takes the initial wavefront and propagates it through a vacuum until it reaches a phase screen and repeats this process for the entire propagation path until every phase screen has perturbed the wavefront. The propagation between the phase screens gives rise to amplitude fluctuations in the wavefront due to diffraction. The level of

turbulence in each phase screen is defined by the refractive index structure parameter (C_n^2). Since we are simulating vertical propagation, the C_n^2 will change at every phase screen. We calculate C_n^2 using the Hufnagel-Valley approximation (Mohr et al. 2010) from Equation 1.17.

We select the values of the coefficients such that the C_n^2 profile simulates the conditions at a typical observatory. We slightly modify the coefficients to obtain the desired Fried parameter. At the end of the propagation process the wavefront is in the aperture plane of the optical system and the values are wrapped between 0 and 2π. To unwrap the phase we use the Goldstein branch cut phase unwrapping algorithm (Goldstein et al. 1988). For our experiment, we replicate the conditions for Mount Wilson and CHARA's 1-meter telescopes. We additionally restrict ourselves to monochromatic light and simulate phases with a wavelength of 637 nm, using a propagation distance of 30 kilometers, and assume that our source is at zenith.

We apply different phases screens with Fried parameters of $r_0 \approx 20$ cm, or $\mathrm{D}/r_0 \approx 5$ (where D here is the diameter of the aperture), to each of our respective SLMs for our experiments (see Figure 5.4) in order to replicate good seeing conditions at CHARA. Based on the approximate beam location on our phase screens, the original phase screens have its D/r_0 reduced to $\approx$4. The D/r_0 calculations are based on the variance of the phase,

$$\sigma^2 = 1.0299 \left(\frac{\mathrm{D}}{r_0}\right)^{5/3}. \tag{5.1}$$

These phase screens can additionally be used as a rough estimation for horizontal turbulence as well since the majority of the atmospheric turbulence comes from the ground layer (more realistic phase screens for horizontal turbulence would be generated from a constant C_n^2 profile). The beams in the vacuum tubes at CHARA have a diameter of 12.5 cm and we, therefore, assume this beam size for our horizontal simulated turbulence. Nightly reports from CHARA have shown that the lower bound of seeing conditions correspond to a

range of r_0 from ∼1-3 cm. Therefore, we use the same phase screens to simulate ground seeing conditions that are $r_0 \approx 3.2$ cm based on the 12.5 cm beam size at CHARA that is propagated through their vacuum pipes at a 1742 meter elevation.

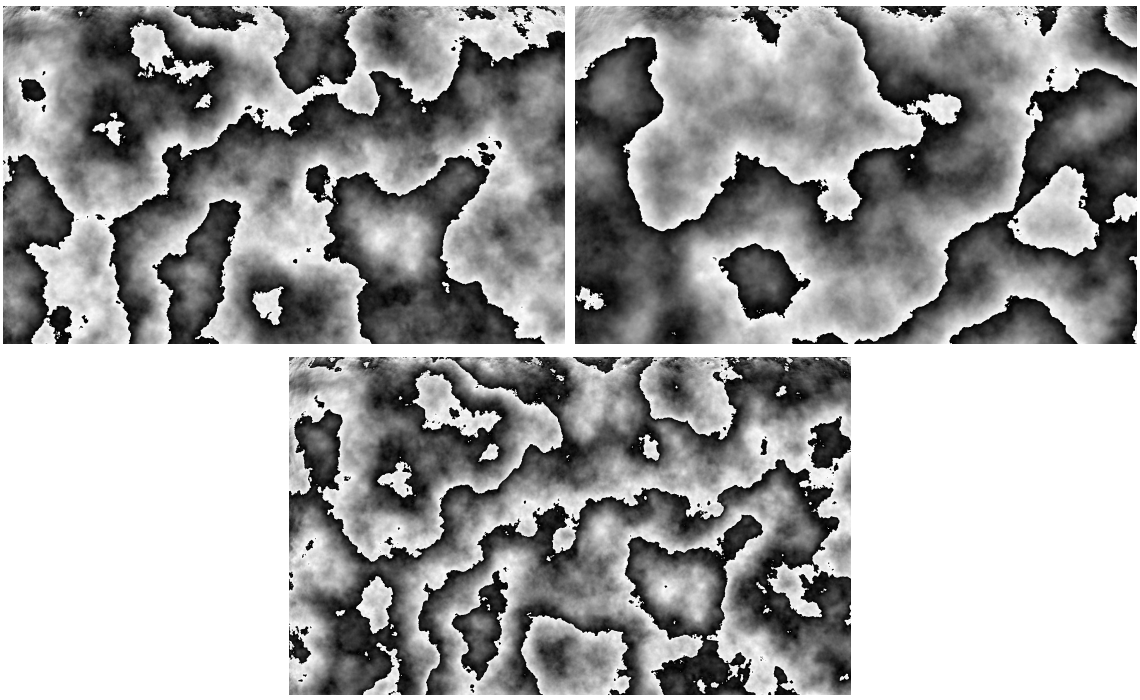

Figure 5.4 Each phase was loaded on each SLM to ensure we are sampling different independent turbulence. Top: Two phase screens that were generated for $D/r_0 \approx 4$ for each SLM. Bottom: An example of one of the re-scaled phase screens. This specific phase screen has a $D/r_0 \approx 6.25$ or $r_0 \approx 2$ cm.

Using one of our original phase screens of $D/r_0 \approx 4$, we scale the corresponding phases (using Equation 5.1) such that the area where the circular beam located on the SLM reflects the desired turbulence conditions. The pupil image is approximately 900 pixels in height and length on the SLM. We obtain seven new phase screens for horizontal turbulence using a 12.5 cm beam size and solve such that $r_0 \approx 0.5$, 1, 2, 3, 5, 6, and 7 cm.

5.5 Looking at the PSF

A first check that our simulator is working is provided by looking at the point spread functions (PSFs) generated in each leg for a flat wavefront, a perturbed wavefront, and a perturbed

wavefront corrected with AO. For this experiment, we only take PSF measurements for one leg with varying phase and leave the second leg unperturbed for this test.

The DM in our experiment corrects for any perturbations of the beam caused by the SLM. Our procedure starts by having a flat SLM (flat to $\lambda/6$), closing the AO loop, and recording the PSF. This determines the best possible PSF we can expect from our system. The RMS wavefront errors recorded on the WFSs are 20 nm. Then, we open the AO loop, insert the $r_0 \approx$ 0.5-7cm phase screens on the SLMs, and record the resulting PSFs. We find that RMS decreases down to approximately 20 nm in all cases. We show the images of our tests in Figure 5.5.

Our calculations of Strehl ratios are calculated by taking a flat SLM, closing the AO system, and comparing the resulting peak PSF value of our flat system to each wavefront that is loaded onto the SLM. The exposure times for each observation are different and therefore we scale the intensities of the images so that all images are on equal scales. The values of the Strehl ratios are listed in Table 5.1. We find that there is an improvement upon the PSF and the Strehl from visual inspection in Figure 5.5 and numerically from Table 5.1 down to a 3 cm wavefront. Phases with r_0 of 2 cm or lower worsen the quality of the PSF where it visually has the PSF start to disperse the light and the values of the Strehl ratio decrease when closing the AO loop. This could be a result of the incoming wavefront from the SLM containing too many phase tears in proximity with each other (i.e., the density of phase tears in a given area is high; see Figure 5.4). Therefore, our WFS and DM-97 combination cannot deal with any wavefront that has high-density phase tears of 2 cm or lower.

5.6 First Results of Fringes

When looking for the fringes we start with flat wavefronts on both SLMs (similar to the PSF) and close the AO loop in both ends to get the best static wavefront for our fringe experiments. To ensure we are looking at the center of the fringe packet, we first put a linear

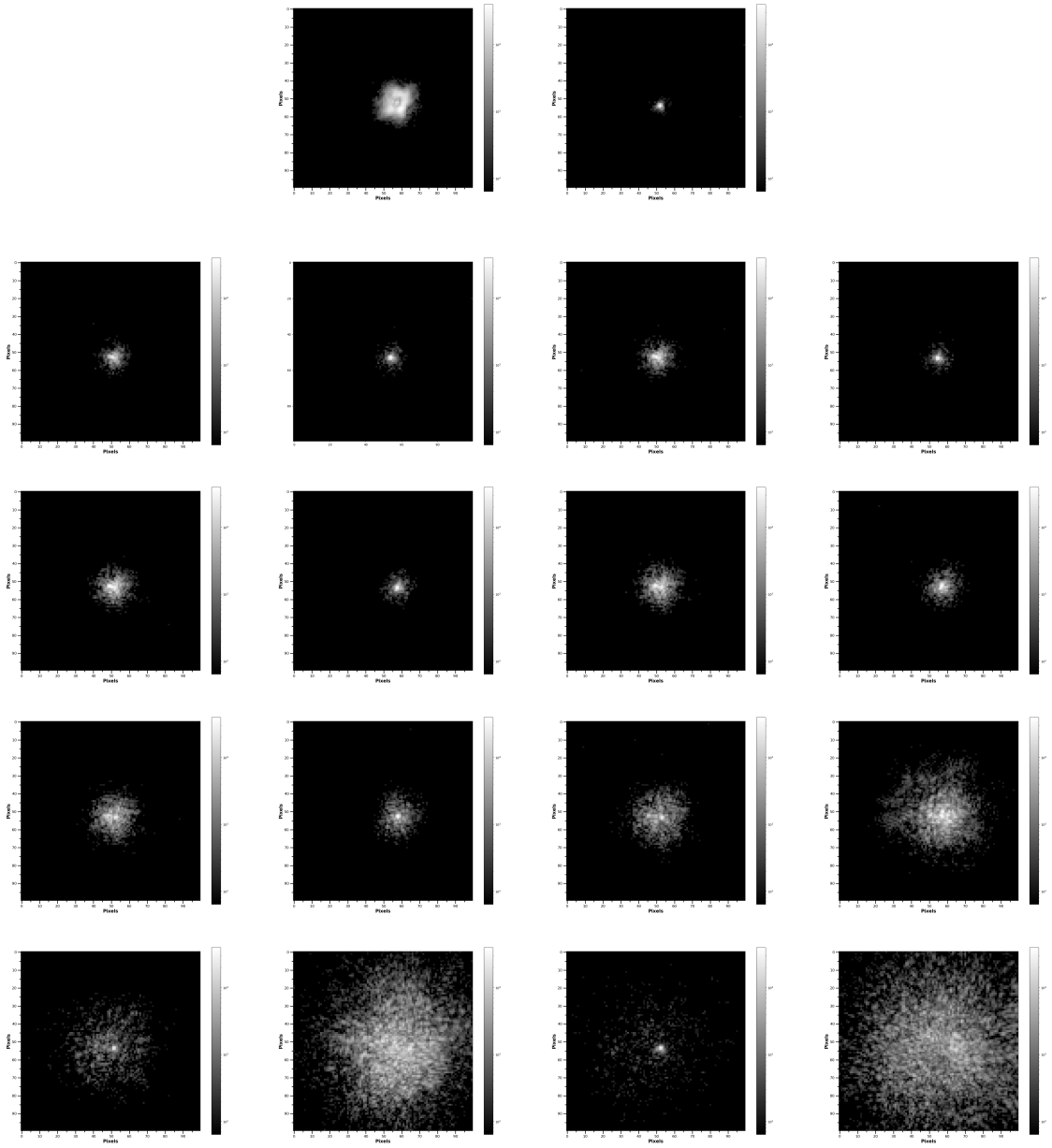

Figure 5.5 Here we show 18 different PSFs of from our experiment from one beam that is used for testing our AO system. The intensity of each PSF is shown in raw counts and is in a logarithmic scale. Top center: The PSF of a flat AO uncorrected wavefront (left) and AO corrected wavefront (right). Each row contains two pairs of PSFs of different r_0 with the uncorrected wavefront being displayed and the corrected wavefront directly to its right. First row with a set of four images: PSF of an uncorrected wavefront with $r_0 \approx 7$ cm (far left), PSF of a corrected wavefront with $r_0 \approx 7$ cm (middle left), PSF of an uncorrected wavefront with $r_0 \approx 6$ cm (middle right), PSF of a corrected wavefront with $r_0 \approx 6$ cm (far right). The pattern is repeated for the following rows where the second row has PSFs of a wavefront with $r_0 \approx 5$ & 4 cm, the third row has PSFs of a wavefront with $r_0 \approx 3$ & 2 cm, the last row has PSFs of a wavefront with $r_0 \approx 1$ & 0.5 cm.

Table 5.1. Strehl Ratio Results

r_0 of Phase (cm)	Exposure Time (s)	Peak Intensity (Counts)	AO System	Strehl Ratio Value
0 (Flat System)	1/19231	37312	off	0.018
0 (Flat System)	1/1000000	39552	on	–
7	1/250000	27584	off	0.174
7	1/333333	55168	on	0.465
6	1/125000	32384	off	0.102
6	1/333333	39168	on	0.330
5	1/62500	36800	off	0.058
5	1/250000	33984	on	0.215
4	1/52632	39104	off	0.052
4	1/142857	44928	on	0.162
3	1/52632	24448	off	0.032
3	1/125000	38592	on	0.122
2	1/52632	28800	off	0.038
2	1/38462	35584	on	0.035
1	1/52632	18880	off	0.025
1	1/5714	25536	on	0.004
0.5	1/52632	23808	off	0.032
0.5	1/5714	15808	on	0.002

stage on the mirror on the first leg between the two beam splitters. We adjust the stage accordingly until we can, by visual inspection, determine that we are observing the center lobe. After we are convinced that our fringes are first lobe measurements (by measuring the intensity variations of fringe contrasts), we follow the same procedure as in Section 5.5. After measuring fringes with flat wavefronts, we load our phase screens from Figure 5.4 to our SLMs and measure our perturbed fringes. We continue our procedure using the $r_0 \approx 4$ phase and close the AO loop in both legs.

From visual inspection, we find that our fringes are perturbed (bent) slightly given a flat wavefront using our AO system but are only visually recognizable near the edge of the beam. When we apply our $D/r_0 \approx 4$ phase screens on our SLMs, our fringes are hardly recognizable even with AO correction. The AO correction unable to correct for the $D/r_0 \approx 4$ phase wrapped phase screens may be due to the wrapped phase screens producing variations in the intensity near the phase tears. While this may not affect the PSF and the AO system

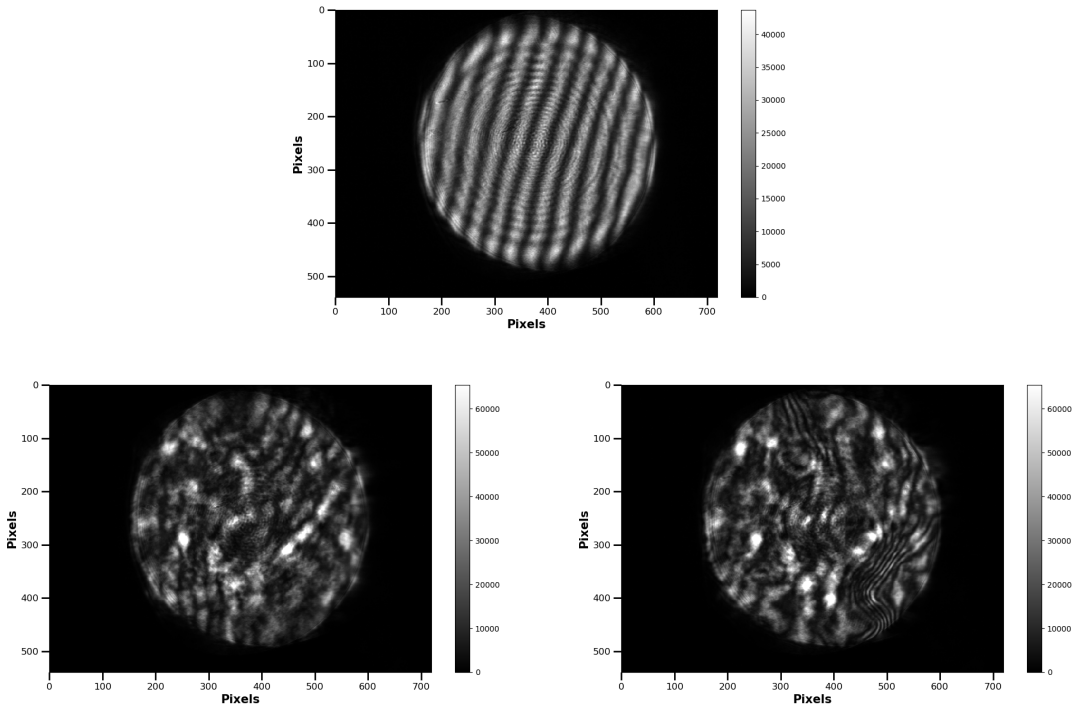

Figure 5.6 The intensity of all of these images are shown in raw counts. Top center: Fringes of a flat wavefront (i.e., no phase loaded on our SLM and a flat DM). Bottom left: Fringes from an uncorrected wavefront of $D/r_0 \approx 4$ on each respective SLM. Bottom right: Fringes from a corrected wavefront of $D/r_0 \approx 4$ on each respective SLM.

is working as expected in the image plane, the AO system we have as-is does not work well in the pupil plane. We show the images of our fringes for these preliminary results in Figure 5.6.

5.7 Discussion

In order to see how how results compare with theoretical results, we use both the equation within Noll (1976) to find the variance of the phase and the Maréchal approximation (Maréchal 1947) to calculate the Strehl ratio. The variance of the phase can be approximated as

$$\sigma^2 \approx 0.2944 J^{-\sqrt{3}/2} \left(\frac{D}{r_0}\right)^{5/3} \tag{5.2}$$

where J is the number of modes that are corrected where this approximation is only valid for $J > 10$ modes. The Maréchal approximation of the Strehl ratio can be found as

$$S \approx \exp\left(-\sigma^2\right) \tag{5.3}$$

where this approximation starts to break down at lower Strehl ratios (e.g., S < 0.3).

For our DM-97 system, we correct 80 modes after piston and therefore expect to get a Strehl ratio of 0.87 given that we use a beam size of 12.5 cm and $r_0 = 2$ cm. Any higher r_0 values, or calmer turbulence conditions, are higher than 0.87 and can be assumed to be diffraction-limited since any Strehl ratio values above 0.8 are considered to be diffraction-limited. The Strehl ratios for the $r_0 = 1$ cm and 0.5 cm phase screens are 0.64 and 0.25, respectively. Our results from Table 5.1 show that our experimental values of the Strehl ratios are much lower than these expected theoretical values. We believe that these lower experimental values are caused by two factors. Since the SLM is only flat by $\lambda/6$ and, at 637 nm, that leaves about 106 nm in error that the WFS needs to additionally correct, along with any potentially small aberrations caused by the optics along the beam path.

However, we have a DM241 for future use within the experiment and should theoretically be able to correct for $r_0 \approx 1$ cm since the corresponding Strehl ratio would be 0.82 even just correcting up to the first 200 modes beyond piston. However, this new DM241 would not be able to do obtain diffraction-limited results with $r_0 \approx 0.5$ cm phase screen but this may be able to correct the worst of seeing conditions at CHARA. We make a note that any piston errors within the phase can be corrected by changing the optical path difference (akin to something similar to delay lines at an interferometer).

Chapter 6
CONCLUSION AND FUTURE DIRECTION

6.1 Summary of Results

We produce a three-dimensional interferometric model-dependent imaging code with robust capabilities to generate surface maps of spotted stars and Roche objects. We describe the layout of our code and how we develop the geometry of the object and convert it to interferometric visibilities so that they can be directly compared to observational data. Then, we discuss how we use the Nelder-Mead algorithm within the NLopt package to produce errors that incorporate both systematic and statistical errors. Finally, we make use of the OptimPack algorithm to produce surface maps of our objects.

We do interferometric modeling and imaging on λ And for the 2010 and 2011 epochs. First, we use SIMTOI in order to find which model is most probable for finding the best parameters. Then we use the parameters from SIMTOI and use them for imaging in ROTIR. Using the parameters from the best SIMTOI model as a prior, we apply the bootstrap method to get the final physical parameters for λ And. We find that our images from ROTIR fairly agree with the images produced to the other image reconstruction code, SURFING, and our physical parameters are also fairly consistent of previous works with the exception of the inclination.

Once we produce static images of the primary star in the system, we test to see if we find any evidence for differential rotation and detect the secondary companion. We start with a simulation of differential rotation and compare those results to the 2011 interferometric data set. Our results remain inconclusive as we cannot detect any sheer within the 2011 data set largely due to λ And being a slow rotator. In our search for the companion, we do a grid search by fitting various models for the companion (i.e., varying the angular radius of the secondary and flux ratio of the system). While the flux ratio was consistent with the approximated value, the angular radius was largely inconsistent with our estimated

calculation, therefore, concluding that we were unable to detect the secondary (Martinez et al. 2021).

We apply the same modeling and imaging method from the λ And work to Alderamin. Our imaging is fairly consistent compared to previous works, however, there are disagreements with various physical parameters. The most notable discrepancy is the fraction of the critical angular velocity, which we find a difference in $\sim$5% lower than that of Zhao et al. (2009). In turn, our lower ω_c yields a slightly higher oblateness mass than expected, which is confirmed by our modeling with the theoretical radiative transfer model ESTER.

In addition to imaging Alderamin, we provide a new surface temperature distribution law, which we call the Espinosa Lara-Rieutord law, and can be compared to the nearly century-old von Zeipel law. As many studies are still reliant on the general von Zeipel law, we provide an easier method to obtain a recommended gravity darkening parameter (original displayed within Espinosa Lara & Rieutord 2011, but not explicitly shown as a complete expression). We find that the Espinosa Lara-Rieutord law is in better agreement with observational data than of a constant gravity darkening parameter $\beta = 0.19$.

Finally, we describe a multi-beam atmospheric turbulence simulator that can be used for research in free-space beam propagation for interferometry. As the first test of our simulator, we simulate atmospheric turbulence with $D/r_0 \approx 25$ to 1.8 ($r_0 \approx 0.5$ cm to 7 cm). The Strehl ratios show that there is an improvement upon the PSF when turning on the AO system down to around $r_0 \approx 3$ cm. The $D/r_0 \approx 4$ is the level of turbulence that we can expect both in the vertical and horizontal propagation directions. We find that AO system is unable to correct for phase wrapped phase screens (Martinez et al. 2020).

6.2 Looking into the Future of Imaging

Our ROTIR code is not just limited to interferometric imaging but is also capable of light-curve inversion. Future work will plan on using the multi-band photometry in Parks et al. (2021) and compare those resulting images with the interferometric images from this work.

These plans also include using the photometric data as a bridge for the 2010 and 2011 interferometric epochs in order to detail how λ And is evolving over the course of a year. There is currently work implementing additional numerical techniques to ROTIR (Abbott et al. in prep) in order to improve light-curve inversion quality with the use of ADMM (Chan et al. 2011). An additional goal of ROTIR is the eventual implementation of Doppler imaging and Zeeman-Doppler imaging, since the ultimate goal of ROTIR is to have an all-in-one imaging tool for the three major imaging techniques (light-curve inversion, Doppler imaging, and interferometric imaging).

A second reduction of Alderamin data is warranted as the calibration routines from the MIRC-X pipeline may not be fully completed (since it is still being refined during the writing of this manuscript). A new calibration could either confirm our re-parameterization Alderamin or the parameterization of the previous imaging works. We have data for other rapid rotators (see Appendix A) which can be used to further investigate the link between the gravity darkening parameter and the fraction of the critical angular velocity. Future imaging campaigns of rapid rotators can incorporate the beam combiners at both CHARA and NPOI using the current MIRC-X and VISION instruments. Furthermore, contemporaneous data collection within different wavelength regimes (K-band and R-band) will soon become possible as the MYSTIC (Monnier et al. 2018) and SPICA (Mourard et al. 2017; Mourard et al. 2018) instruments will come online, and further upgrades to MIRC-X will expand 6T observations to J-band.

Other studies, such as Zorec et al. (2017), have modified the Espinosa Lara-Rieutord law in order to take into account surface differential rotation. Since our code takes in a solar-like differential law, we plan to implement this newly modified law into ROTIR for rapidly rotating stars. As our code is currently limited to spherical and Roche-shaped object imaging, an implementation of other geometries is needed. However, this is only limited to systems that have a direct model (e.g., Be stars, stars with disks) since our code is model-dependent.

Our preliminary results look promising for free-space beam propagation. Even though there is a possibility that the experiment may not work at simulating a moving telescope because the true ground layer turbulence conditions are much worse than expected (i.e., our system may not be able to correct turbulence from $r_0 \approx 3$ cm or lower). However, if we find that we can eventually correct down to $r_0 \approx 0.5$ cm, then this experiment can be used at CHARA (assuming that this is the worst ground turbulence at CHARA). Practically, if this concept were taken to CHARA, other issues may arise. How would we accommodate a return beam or the return signal from the WFS near the beam combining lab to the DM at the telescope? Perhaps one suggestion would be to use a radio signal to send the DM for wavefront corrections. Would we need to worry about amplitude variations at CHARA? While it may seem that at short distances (a few meters) may not suffer from amplitude variations, at larger distances there may be some amplitude variations or loss but it is currently unknown at which distances this may start.

We note that the level of horizontal turbulence used in this work is optimistic as the ground layer turbulence at the CHARA Array could be as low as $r_0 = 0.5$ - 1 cm. Several tests will need to follow this preliminary work. First, carefully re-imaging the pupil from the SLM to the DM will need to be done in order to remove the circular ring pattern on the background of our fringes. We have another set of SLMs and a set DM241s not implemented in this experiment. To study higher levels of horizontal turbulence, we plan to use the DM97-15 deformable mirrors and SLMs in combination with each other in a woofer and tweeter manner. The DMs will be used for the high amplitude but low-spatial frequency components of the wavefront phase, while the SLMs will be used for the high spatial frequency, low amplitude components. We plan to simulate a wider range of horizontal phases from $r_0 \approx 7$ cm down to 0.5 cm ($D/r_0 \approx 1.8$ - 25) with constant C_n^2 profiles and find the limiting seeing conditions for when we can find stable fringes. We also plan to implement the third leg, to simulate a three-telescope interferometer.

Finally, to chart the possible degradation of seeing conditions at Mount Wilson (Teare et al. 2000), an investigation of site conditions (by taking measurements at CHARA to investigate the ground layer seeing conditions) is warranted in order more accurately simulate seeing conditions within the lab simulator. Future experiments could include work similar to those done by Gibson (Gibson & Hammel 2014) to calculate the C_n^2 profile of the ground layer where our horizontal beam propagation will occur.

References

Abbott, C. G., Baron, F., & Martinez, A. O. in prep

Abney, W. D. W. 1877, MNRAS, 37, 278, doi: 10.1093/mnras/37.5.278

Abt, H. A., & Morrell, N. I. 1995, ApJS, 99, 135, doi: 10.1086/192182

Abt, H. A., & Moyd, K. I. 1973, ApJ, 182, 809, doi: 10.1086/152184

Anugu, N., Le Bouquin, J.-B., Monnier, J. D., et al. 2018, in Society of Photo-Optical Instrumentation Engineers (SPIE) Conference Series, Vol. 10701, Optical and Infrared Interferometry and Imaging VI, ed. M. J. Creech-Eakman, P. G. Tuthill, & A. Mérand, 1070124, doi: 10.1117/12.2313036

Anugu, N., Le Bouquin, J.-B., Monnier, J. D., et al. 2020, AJ, 160, 158, doi: 10.3847/1538-3881/aba957

Armstrong, J. T., Mozurkewich, D., Rickard, L. J., et al. 1998, ApJ, 496, 550, doi: 10.1086/305365

Aufdenberg, J. P., Mérand, A., Coudé du Foresto, V., et al. 2006, ApJ, 645, 664, doi: 10.1086/504149

Baglin, A., Michel, E., Auvergne, M., & COROT Team. 2006a, in ESA Special Publication, Vol. 624, Proceedings of SOHO 18/GONG 2006/HELAS I, Beyond the spherical Sun, 34

Baglin, A., Auvergne, M., Boisnard, L., et al. 2006b, in COSPAR Meeting, Vol. 36, 36th COSPAR Scientific Assembly

Baldwin, J. E., Haniff, C. A., Mackay, C. D., & Warner, P. J. 1986, Nature, 320, 595, doi: 10.1038/320595a0

Baliunas, S. L., & Dupree, A. K. 1979, ApJ, 227, 870, doi: 10.1086/156797

—. 1982, ApJ, 252, 668, doi: 10.1086/159593

Barnes, T. G., Evans, D. S., & Moffett, T. J. 1978, MNRAS, 183, 285, doi: 10.1093/mnras/183.3.285

Baron, F. 2016, in Astronomy at High Angular Resolution, ed. Boffin, H. M. J. and Hussain, G. and Berger, J.-P. and Schmidtobreick, L., Vol. 439, 75, doi: 10.1007/978-3-319-39739-9

Baron, F., & Martinez, A. O. 2018, ROTIR: Interferometric imaging and light curve inversion on rotating spheroids. https://github.com/fabienbaron/ROTIR.jl

—. in prep

Baron, F., Monnier, J. D., & Kloppenborg, B. 2010, in Society of Photo-Optical Instrumentation Engineers (SPIE) Conference Series, Vol. 7734, Optical and Infrared Interferometry II, ed. W. C. Danchi, F. Delplancke, & J. K. Rajagopal, 77342I, doi: 10.1117/12.857364

Baron, F., Norris, R. P., & Martinez, A. O. 2019, OITOOLS: the All-in-One Tool Package for Optical Interferometry. https://github.com/fabienbaron/OITOOLS.jl

Baron, F., Monnier, J. D., Pedretti, E., et al. 2012, ApJ, 752, 20, doi: 10.1088/0004-637X/752/1/20

Baron, F. R. 2020, in Society of Photo-Optical Instrumentation Engineers (SPIE) Conference Series, Vol. 11446, Society of Photo-Optical Instrumentation Engineers (SPIE) Conference Series, 114461N, doi: 10.1117/12.2561582

Basri, G. S., & Linsky, J. L. 1979, ApJ, 234, 1023, doi: 10.1086/157586

Berdyugina, S. V. 1998, A&A, 338, 97

—. 2005, Living Reviews in Solar Physics, 2, 8, doi: 10.12942/lrsp-2005-8

Bonneau, D., Clausse, J. M., Delfosse, X., et al. 2006, A&A, 456, 789, doi: 10.1051/0004-6361:20054469

Bopp, B. W., & Noah, P. V. 1980, PASP, 92, 717, doi: 10.1086/130736

Borucki, W. J., Koch, D., Basri, G., et al. 2010, Science, 327, 977, doi: 10.1126/science.1185402

Bos, J. P., & Roggemann, M. C. 2012, Optical Engineering, 51, 101704, doi: 10.1117/1.OE.51.10.101704

Box, M. J. 1965, The Computer Journal, 8, 42, doi: 10.1093/comjnl/8.1.42

Boyajian, T. S., McAlister, H. A., van Belle, G., et al. 2012, ApJ, 746, 101, doi: 10.1088/0004-637X/746/1/101

Boyd, R. W., Eaton, J. A., Hall, D. S., et al. 1983, Ap&SS, 90, 197, doi: 10.1007/BF00651560

Brent, R. P. 1973, SIAM Journal on Numerical Analysis, 10, 327

Broyden, C. G. 1965, Mathematics of Computation, 19, 577. http://www.jstor.org/stable/2003941

Buscher, D. F., & Longair, F. b. M. 2015, Practical Optical Interferometry

Calder, W. A. 1938, Harvard College Observatory Bulletin, 907, 20

Cameron, E., & Pettitt, A. 2014, Statistical Science, 29, 397 , doi: 10.1214/13-STS465

Catala, C., Donati, J. F., Shkolnik, E., Bohlender, D., & Alecian, E. 2007, MNRAS, 374, L42, doi: 10.1111/j.1745-3933.2006.00261.x

Chael, A. A., Johnson, M. D., Bouman, K. L., et al. 2018, ApJ, 857, 23, doi: 10.3847/1538-4357/aab6a8

Chan, S. H., Khoshabeh, R., Gibson, K. B., Gill, P. E., & Nguyen, T. Q. 2011, IEEE Transactions on Image Processing, 20, 3097. https://videoprocessing.ucsd.edu/~stanleychan/deconvtv

Charbonneau, P. 1995, ApJS, 101, 309, doi: 10.1086/192242

Che, X., Monnier, J. D., Zhao, M., et al. 2011, ApJ, 732, 68, doi: 10.1088/0004-637X/732/2/68

Che, X., Monnier, J. D., Tycner, C., et al. 2012, ApJ, 757, 29, doi: 10.1088/0004-637X/757/1/29

Chopin, N., & Robert, C. P. 2010, Biometrika, 97, 741, doi: 10.1093/biomet/asq021

Chu, F.-L., & Huang, C.-F. 1989, Journal of Physics A: Mathematical and General, 22, L671, doi: 10.1088/0305-4470/22/14/003

Collins, George W., I. 1963, ApJ, 138, 1134, doi: 10.1086/147712

Collins, George W., I., & Harrington, J. P. 1966, ApJ, 146, 152, doi: 10.1086/148866

Corley, M., Santiago, F., T., M., & Agrawal, B. 2011, Horizontal Propagation Deep Turbulence Testbed, Calhoun. https://calhoun.nps.edu/handle/10945/34525

Davenport, J. R. A., Hebb, L., & Hawley, S. L. 2015, ApJ, 806, 212, doi: 10.1088/0004-637X/806/2/212

Domiciano de Souza, A., Kervella, P., Jankov, S., et al. 2003, A&A, 407, L47, doi: 10.1051/0004-6361:20030786

Donati, J.-F., Henry, G. W., & Hall, D. S. 1995, A&A, 293, 107

Drake, J. J., Ball, B., Eldridge, J. J., Ness, J.-U., & Stancliffe, R. J. 2011, AJ, 142, 144, doi: 10.1088/0004-6256/142/5/144

Ducati, J. R. 2002, VizieR Online Data Catalog

Eggleton, P. P. 1983, ApJ, 268, 368, doi: 10.1086/160960

Eker, Z., Ak, N. F., Bilir, S., et al. 2008, MNRAS, 389, 1722, doi: 10.1111/j.1365-2966.2008.13670.x

Elston, R., Zeilik, M., Henson, G., Schmolke, P., & Smith, P. 1982, Information Bulletin on Variable Stars, 2150, 1

Elvey, C. T. 1930, ApJ, 71, 221, doi: 10.1086/143249

Espinosa Lara, F., & Rieutord, M. 2011, A&A, 533, A43, doi: 10.1051/0004-6361/201117252

—. 2013, A&A, 552, A35, doi: 10.1051/0004-6361/201220844

Feroz, F., & Hobson, M. P. 2008, MNRAS, 384, 449, doi: 10.1111/j.1365-2966.2007.12353.x

Feroz, F., Hobson, M. P., & Bridges, M. 2009, MNRAS, 398, 1601, doi: 10.1111/j.1365-2966.2009.14548.x

Feroz, F., Hobson, M. P., Cameron, E., & Pettitt, A. N. 2019, The Open Journal of Astrophysics, 2, 10, doi: 10.21105/astro.1306.2144

Fizeau, H. 1868, Comptes Rendus de l'Académie des Sciences, 66, 932

Frasca, A., Biazzo, K., Taş, G., Evren, S., & Lanzafame, A. C. 2008, A&A, 479, 557, doi: 10.1051/0004-6361:20077915

Frasca, A., Fröhlich, H. E., Bonanno, A., et al. 2011, A&A, 532, A81, doi: 10.1051/0004-6361/201116980

Fried, D. L. 1965, Journal of the Optical Society of America (1917-1983), 55, 1427

—. 1966, Journal of the Optical Society of America (1917-1983), 56, 1372

Fröhlich, H. E., Frasca, A., Catanzaro, G., et al. 2012, A&A, 543, A146, doi: 10.1051/0004-6361/201219167

Gallenne, A., Mérand, A., Kervella, P., et al. 2015, A&A, 579, A68, doi: 10.1051/0004-6361/201525917

Gibson, K. B., & Hammel, S. M. 2014, in Society of Photo-Optical Instrumentation Engineers (SPIE) Conference Series, Vol. 9224, Proc. SPIE, 92240V, doi: 10.1117/12.2064288

Goldstein, R., Zebker, H., & Werner, C. 1988, Radio Science, 23, doi: 10.1029/RS023i004p00713

Goncharskii, A. V., Stepanov, V. V., Kokhlova, V. L., & Yagola, A. G. 1977, Soviet Astronomy Letters, 3, 147

Górski, K. M., Hivon, E., Banday, A. J., et al. 2005, ApJ, 622, 759, doi: 10.1086/427976

Gratton, L. 1950, ApJ, 111, 31, doi: 10.1086/145236

Gray, R. O., Corbally, C. J., Garrison, R. F., McFadden, M. T., & Robinson, P. E. 2003, AJ, 126, 2048, doi: 10.1086/378365

Hall, D. S. 1976, Astrophysics and Space Science Library, Vol. 60, The RS CVn Binaries and Binaries with Similar PROPERTIÉS, ed. W. S. Fitch, 287, doi: 10.1007/978-94-010-1175-4_15

Hall, D. S., & Henry, G. W. 1994, International Amateur-Professional Photoelectric Photometry Communications, 55, 51

Hall, D. S., Henry, G. W., Bohme, D., et al. 1991, Journal of Astrophysics and Astronomy, 12, 281, doi: 10.1007/BF02702317

Hanbury Brown, R., Davis, J., & Allen, L. R. 1974, MNRAS, 167, 121, doi: 10.1093/mnras/167.1.121

Haniff, C. A., Mackay, C. D., Titterington, D. J., Sivia, D., & Baldwin, J. E. 1987, Nature, 328, 694, doi: 10.1038/328694a0

Harmon, R. O., & Crews, L. J. 2000, AJ, 120, 3274, doi: 10.1086/316882

Henry, G. W., Eaton, J. A., Hamer, J., & Hall, D. S. 1995, ApJS, 97, 513, doi: 10.1086/192149

Hernandez, J., Rincón, J., Ballesteros, A., Tíjaro, O., & Torres, Y. 2020, Optics Communications, 458, 124870, doi: 10.1016/j.optcom.2019.124870

Hestroffer, D. 1997, A&A, 327, 199

Hussain, G. A. J. 2002, Astronomische Nachrichten, 323, 349

Jennison, R. C. 1958, MNRAS, 118, 276, doi: 10.1093/mnras/118.3.276

Johnson, S. G. 2007, The NLopt nonlinear-optimization package. https://github.com/stevengj/nlopt

Kashyap, V. L., Drake, J. J., & Saar, S. H. 2008, ApJ, 687, 1339, doi: 10.1086/591922

Kővári, Z., Kriskovics, L., Künstler, A., et al. 2015, A&A, 573, A98, doi: 10.1051/0004-6361/201424138

Kloppenborg, B., & Baron, F. 2012a, LibOI: The OpenCL Interferometry Library, Version 1.0.0. https://github.com/bkloppenborg/liboi

—. 2012b, SIMTOI: SImulation and Modeling Tool for Optical Interferometry, Version 1.1.1. https://github.com/bkloppenborg/simtoi

Kloppenborg, B. K., Stencel, R. E., Monnier, J. D., et al. 2015, ApJS, 220, 14, doi: 10.1088/0067-0049/220/1/14

Koch, D. G., Borucki, W. J., Basri, G., et al. 2010, ApJ, 713, L79, doi: 10.1088/2041-8205/713/2/L79

Kolmogorov, A. N. 1961 (Interscience Publishers Inc., New York), 151–161

Kopal, Z. 1959, Close binary systems

Korhonen, H., & Elstner, D. 2011, A&A, 532, A106, doi: 10.1051/0004-6361/201117016

Kraus, S., Monnier, J. D., Anugu, N., et al. 2018, in Society of Photo-Optical Instrumentation Engineers (SPIE) Conference Series, Vol. 10701, Optical and Infrared Interferometry and Imaging VI, ed. M. J. Creech-Eakman, P. G. Tuthill, & A. Mérand, 1070123, doi: 10.1117/12.2311706

Kron, G. E. 1947, PASP, 59, 261, doi: 10.1086/125964

Labeyrie, A., Lipson, S. G., & Nisenson, P. 2006, An Introduction to Optical Stellar Interferometry, doi: 10.2277/0521828724

Lanza, A. F. 2008, A&A, 487, 1163, doi: 10.1051/0004-6361:200809753

Le Bouquin, J.-B. 2020, MIRC-X data reduction pipeline. https://gitlab.chara.gsu.edu/lebouquj/mircx_pipeline

Leahy, D. A., & Leahy, J. C. 2015, Computational Astrophysics and Cosmology, 2, 4, doi: 10.1186/s40668-015-0008-8

Lee, S.-W., & Mittra, R. 1983, IEEE Transactions on Antennas and Propagation, 31, 99, doi: 10.1109/TAP.1983.1142981

Ligi, R., Creevey, O., Mourard, D., et al. 2016, A&A, 586, A94, doi: 10.1051/0004-6361/201527054

Limber, D. N. 1963, ApJ, 138, 1112, doi: 10.1086/147711

Linsky, J. L., Ayres, T. R., Basri, G. S., et al. 1978, Nature, 275, 389, doi: 10.1038/275389a0

Lucy, L. B. 1967, ZAp, 65, 89

Maeder, A., & Meynet, G. 2010, New A Rev., 54, 32, doi: 10.1016/j.newar.2010.09.017

Maldonado, J., Affer, L., Micela, G., et al. 2015, A&A, 577, A132, doi: 10.1051/0004-6361/201525797

Maréchal, A. 1947, Revue d'Optique

Martinez, A. O., Abbott, C. G., Jefferies, S. M., ten Brummelaar, T. A., & Baron, F. R. 2020, in Society of Photo-Optical Instrumentation Engineers (SPIE) Conference Series, Vol. 11446, Society of Photo-Optical Instrumentation Engineers (SPIE) Conference Series, 114461B, doi: 10.1117/12.2561666

Martinez, A. O., Baron, F. R., Monnier, J. D., Roettenbacher, R. M., & Parks, J. R. 2021, arXiv e-prints, arXiv:2107.06366. https://arxiv.org/abs/2107.06366

McAlister, H. A., ten Brummelaar, T. A., Gies, D. R., et al. 2005, ApJ, 628, 439, doi: 10.1086/430730

McInturff, K., & Simon, P. S. 1991, IEEE Transactions on Antennas and Propagation, 39, 1441, doi: 10.1109/8.99058

McLaughlin, D. B. 1924, ApJ, 60, 22, doi: 10.1086/142826

Meftah, M., Irbah, A., Hauchecorne, A., et al. 2015, Sol. Phys., 290, 673, doi: 10.1007/s11207-015-0655-6

Meynet, G., & Maeder, A. 2000, A&A, 361, 101. https://arxiv.org/abs/astro-ph/0006404

Michelson, A. A. 1891a, PASP, 3, 217, doi: 10.1086/120291

—. 1891b, PASP, 3, 274, doi: 10.1086/120327

—. 1891c, Nature, 45, 160, doi: 10.1038/045160a0

—. 1920, ApJ, 51, 257, doi: 10.1086/142550

Michelson, A. A., & Pease, F. G. 1921, ApJ, 53, 249, doi: 10.1086/142603

Mohr, J., Johnston, R., & Cottrell, P. 2010, Publications of the Astronomical Society of Australia, 27, 347, doi: 10.1071/AS10008

Monnier, J. D. 2003, Reports on Progress in Physics, 66, 789, doi: 10.1088/0034-4885/66/5/203

Monnier, J. D., Berger, J.-P., Millan-Gabet, R., & ten Brummelaar, T. A. 2004, in Proc. SPIE, Vol. 5491, New Frontiers in Stellar Interferometry, ed. W. A. Traub, 1370, doi: 10.1117/12.550804

Monnier, J. D., Zhao, M., Pedretti, E., et al. 2007, Science, 317, 342, doi: 10.1126/science.1143205

Monnier, J. D., Anderson, M., Baron, F., et al. 2010, in Society of Photo-Optical Instrumentation Engineers (SPIE) Conference Series, Vol. 7734, Optical and Infrared Interferometry II, ed. W. C. Danchi, F. Delplancke, & J. K. Rajagopal, 77340G, doi: 10.1117/12.858286

Monnier, J. D., Che, X., Zhao, M., et al. 2012, ApJ, 761, L3, doi: 10.1088/2041-8205/761/1/L3

Monnier, J. D., Le Bouquin, J.-B., Anugu, N., et al. 2018, in Society of Photo-Optical Instrumentation Engineers (SPIE) Conference Series, Vol. 10701, Optical and Infrared Interferometry and Imaging VI, ed. M. J. Creech-Eakman, P. G. Tuthill, & A. Mérand, 1070122, doi: 10.1117/12.2312762

Mourard, D., Monnier, J. D., Meilland, A., et al. 2015, A&A, 577, A51, doi: 10.1051/0004-6361/201425141

Mourard, D., Bério, P., Perraut, K., et al. 2017, J. Opt. Soc. Am. A, 34, A37, doi: 10.1364/JOSAA.34.000A37

Mourard, D., Nardetto, N., ten Brummelaar, T., et al. 2018, in Society of Photo-Optical Instrumentation Engineers (SPIE) Conference Series, Vol. 10701, Optical and Infrared Interferometry and Imaging VI, ed. M. J. Creech-Eakman, P. G. Tuthill, & A. Mérand, 1070120, doi: 10.1117/12.2311869

Nelder, J., & Mead, R. 1965, Comput. J., 7, 308

Nielsen, M. B., Gizon, L., Cameron, R. H., & Miesch, M. 2019, A&A, 622, A85, doi: 10.1051/0004-6361/201834373

Noll, R. J. 1976, J. Opt. Soc. Am., 66, 207, doi: 10.1364/JOSA.66.000207

Nordgren, T. E., Germain, M. E., Benson, J. A., et al. 1999, AJ, 118, 3032, doi: 10.1086/301114

Ohishi, N., Nordgren, T. E., & Hutter, D. J. 2004, ApJ, 612, 463, doi: 10.1086/422422

Parks, J. R., White, R. J., Baron, F., et al. 2021, ApJ, 913, 54, doi: 10.3847/1538-4357/abb670

Pasinetti Fracassini, L. E., Pastori, L., Covino, S., & Pozzi, A. 2001, A&A, 367, 521, doi: 10.1051/0004-6361:20000451

Pathania, A., & Medupe, T. 2012, Ap&SS, 338, 127, doi: 10.1007/s10509-011-0928-y

Perryman, M. A. C., Lindegren, L., Kovalevsky, J., et al. 1997, A&A, 500, 501

Pinsonneault, M. 1997, ARA&A, 35, 557, doi: 10.1146/annurev.astro.35.1.557

Piskunov, N. E., & Wehlau, W. H. 1990, A&A, 233, 497

Poe, C. H., & Eaton, J. A. 1985, ApJ, 289, 644, doi: 10.1086/162928

Readhead, A. C. S., Nakajima, T. S., Pearson, T. J., et al. 1988, AJ, 95, 1278, doi: 10.1086/114724

Renard, S., Thiébaut, E., & Malbet, F. 2011, A&A, 533, A64, doi: 10.1051/0004-6361/201016263

Rice, J., Wehlau, W., Khokhlova, V. L., & Piskunov, N. E. 1981, in Liege International Astrophysical Colloquia, Vol. 23, Liege International Astrophysical Colloquia, 265–270

Richardson, J. A., & Kuester, J. L. 1973, Commun. ACM, 16, 487–489, doi: 10.1145/355609.362324

Rieutord, M. 2006, A&A, 451, 1025, doi: 10.1051/0004-6361:20054433

Rieutord, M., Espinosa Lara, F., & Putigny, B. 2016, Journal of Computational Physics, 318, 277, doi: 10.1016/j.jcp.2016.05.011

Roche, E. A. 1837, Mém. de l'Acad. de Montpellier (Section des Sciences), Vol. 8, 235

Roddier, F. 1988, Phys. Rep., 170, 97, doi: 10.1016/0370-1573(88)90045-2

Roettenbacher, R. M., Harmon, R. O., Vutisalchavakul, N., & Henry, G. W. 2011, AJ, 141, 138, doi: 10.1088/0004-6256/141/4/138

Roettenbacher, R. M., Kane, S. R., Monnier, J. D., & Harmon, R. O. 2016a, ApJ, 832, 207, doi: 10.3847/0004-637X/832/2/207

Roettenbacher, R. M., Monnier, J. D., Harmon, R. O., Barclay, T., & Still, M. 2013, ApJ, 767, 60, doi: 10.1088/0004-637X/767/1/60

Roettenbacher, R. M., Monnier, J. D., Korhonen, H., et al. 2016b, Nature, 533, 217, doi: 10.1038/nature17444

—. 2017, ApJ, 849, 120, doi: 10.3847/1538-4357/aa8ef7

Rogers, F. J., Swenson, F. J., & Iglesias, C. A. 1996, ApJ, 456, 902, doi: 10.1086/176705

Rogstad, D. H. 1968, Appl. Opt., 7, 585, doi: 10.1364/AO.7.000585

Rossiter, R. A. 1924, ApJ, 60, 15, doi: 10.1086/142825

Royer, F., Zorec, J., & Gómez, A. E. 2007, A&A, 463, 671, doi: 10.1051/0004-6361:20065224

Santos, A. R. G., García, R. A., Mathur, S., et al. 2019, ApJS, 244, 21, doi: 10.3847/1538-4365/ab3b56

Schaefer, G. H., Brummelaar, T. T., Gies, D. R., et al. 2014, Nature, 515, 234, doi: 10.1038/nature13834

Schlesinger, F. 1909, Publications of the Allegheny Observatory of the University of Pittsburgh, 1

—. 1911, MNRAS, 71, 719, doi: 10.1093/mnras/71.9.719

Schmidt, J. D. 2010, Numerical Simulation of Optical Wave Propagation using MATLAB (SPIE Press). https://doi.org/10.1117/3.866274

Schöller, M. 2007, New A Rev., 51, 628, doi: 10.1016/j.newar.2007.06.008

Sepinsky, J. F., Willems, B., & Kalogera, V. 2007, ApJ, 660, 1624, doi: 10.1086/513736

Shajn, G., & Struve, O. 1929, MNRAS, 89, 222, doi: 10.1093/mnras/89.3.222

Shkolnik, E., Walker, G. A. H., & Bohlender, D. A. 2003, ApJ, 597, 1092, doi: 10.1086/378583

Sivia, D. S., & Skilling, J. 2006, Data Analysis: A Bayesian Tutorial

Skilling, J. 2004, in American Institute of Physics Conference Series, Vol. 735, Bayesian Inference and Maximum Entropy Methods in Science and Engineering: 24th International Workshop on Bayesian Inference and Maximum Entropy Methods in Science and Engineering, ed. R. Fischer, R. Preuss, & U. V. Toussaint, 395–405, doi: 10.1063/1.1835238

Skilling, J. 2006, Bayesian Analysis, 1, 833 , doi: 10.1214/06-BA127

Slettebak, A. 1949, ApJ, 110, 498, doi: 10.1086/145226

—. 1955, ApJ, 121, 653, doi: 10.1086/146031

Somers, G., & Pinsonneault, M. H. 2015, ApJ, 807, 174, doi: 10.1088/0004-637X/807/2/174

Strassmeier, K. G. 1999, A&A, 347, 225

—. 2009, A&A Rev., 17, 251, doi: 10.1007/s00159-009-0020-6

Strassmeier, K. G., Hall, D. S., & Henry, G. W. 1994, A&A, 282, 535

Struve, O., & Elvey, C. T. 1931, MNRAS, 91, 663, doi: 10.1093/mnras/91.6.663

Tas, G., & Evren, S. 2000, Information Bulletin on Variable Stars, 4992, 1

Tatarskii, V. I. 1961, Wave Propagation in Turbulent Medium

Taylor, G. I. 1938, Proceedings of the Royal Society of London Series A, 164, 476, doi: 10.1098/rspa.1938.0032

Teare, S. W., Thompson, L. A., Gino, M. C., & Palmer, K. A. 2000, PASP, 112, 1496, doi: 10.1086/317701

Temple, R. 1986, The genius of China: 3000 years of science, discovery, and invention (New York: Simon and Schuster)

ten Brummelaar, T. A., McAlister, H. A., Ridgway, S. T., et al. 2005, ApJ, 628, 453, doi: 10.1086/430729

Thiebaut, E. 2002, in Astronomical Data Analysis II, ed. J.-L. Starck & F. D. Murtagh, Vol. 4847, International Society for Optics and Photonics (SPIE), 174 – 183, doi: 10.1117/12.461151

van Belle, G. T. 2012, A&A Rev., 20, 51, doi: 10.1007/s00159-012-0051-2

van Belle, G. T., Ciardi, D. R., Thompson, R. R., Akeson, R. L., & Lada, E. A. 2001, ApJ, 559, 1155, doi: 10.1086/322340

van Belle, G. T., Ciardi, D. R., ten Brummelaar, T., et al. 2006, ApJ, 637, 494, doi: 10.1086/498334

van Cittert, P. H. 1934, Physica, 1, 201, doi: 10.1016/S0031-8914(34)90026-4

van Leeuwen, F. 2007, A&A, 474, 653, doi: 10.1051/0004-6361:20078357

Vaquero, J. M. 2007, Journal of the British Astronomical Association, 117, 346

Vaughan, Arthur H., J. 1967, Leaflet of the Astronomical Society of the Pacific, 10, 57

Vogel, H. C. 1877, Astronomische Nachrichten, 90, 71, doi: 10.1002/asna.18770900503

Vogt, S. S., Penrod, G. D., & Hatzes, A. P. 1987, ApJ, 321, 496, doi: 10.1086/165647

von Zeipel, H. 1924a, MNRAS, 84, 684, doi: 10.1093/mnras/84.9.684

—. 1924b, MNRAS, 84, 665, doi: 10.1093/mnras/84.9.665

Vorontsov, M., Carhart, G., Gudimetla, R., et al. 2010, in Advanced Maui Optical and Space Surveillance Technologies Conference, E18

Walker, E. C. 1944, JRASC, 38, 249

Westgate, C. 1933a, ApJ, 77, 141, doi: 10.1086/143454

—. 1933b, ApJ, 78, 46, doi: 10.1086/143483

—. 1934, ApJ, 79, 357, doi: 10.1086/143542

Wild, W. J. 1989, PASP, 101, 844, doi: 10.1086/132505

Zernike, F. 1938, Physica, 5, 785, doi: 10.1016/S0031-8914(38)80203-2

Zhao, M., Gies, D., Monnier, J. D., et al. 2008, ApJ, 684, L95, doi: 10.1086/592146

Zhao, M., Monnier, J. D., Pedretti, E., et al. 2009, ApJ, 701, 209, doi: 10.1088/0004-637X/701/1/209

Zhao, M., Monnier, J. D., Che, X., et al. 2011, PASP, 123, 964, doi: 10.1086/661762

Zorec, J., Rieutord, M., Espinosa Lara, F., et al. 2017, A&A, 606, A32, doi: 10.1051/0004-6361/201730818

Appendix A
FULL MIRC-X/CHARA OBSERVATION LOG

Table A.1. CHARA Array observations from 2017 to 2020

Object	UT date	Baselines	Mode	Calibrators	Notes
–	2017 Oct 25				(1)
Caph	2017 Oct 26	W1-S1-S2-E1-E2-W2	H-PRISM	7 And, ζ Cas	
Cursa (β Eri)	2017 Oct 26	W1-S1-S2-E1-E2-W2	H-PRISM	HD 19994, HD 33256	
28 Mon	2017 Oct 26	W1-S1-S2-E1-E2-W2	H-PRISM	HD 55185	
Caph	2017 Oct 27	W1-S1-S2-E1-E2-W2	H-PRISM	7 And, ζ Cas	
Cursa	2017 Oct 27	W1-S1-S2-E1-E2-W2	H-PRISM	HD 25490, HD 33256	
Caph	2017 Oct 28	W1-S1-S2-E1-E2-W2	H-PRISM	7 And, θ Cas	
Cursa	2017 Oct 28	W1-S1-S2-E1-E2-W2	H-PRISM	HD 25490, HD 33256	
28 Mon	2017 Oct 28	W1-S1-S2-E1-E2-W2	H-PRISM	HD 55185	
–	2018 Mar 26				(2)
–	2018 Mar 27				(2,3)
Rasalhague	2018 Mar 28	W1-S1-S2-W2	H-PRISM	γ Ser	(4)
Zosma (δ Leo)	2018 Mar 29	W1-S1-S2-E1-E2-W2	H-PRISM	η Leo, β Com	(5)
31 Com	2018 Mar 29	W1-S1-S2-E1-E2-W2	H-PRISM	β Com, HD 119035	(5)
Rasalhague	2018 Mar 29	W1-S1-S2-W2	H-PRISM	γ Ser, HD 173667	(5)
–	2018 May 25				(2)
–	2018 May 26				(2)
–	2018 May 27				(2,3)
Caph	2018 Sep 21	E1-W2-W1-S2-E2	H-PRISM	ζ Cas, θ Cas	(4)
Cursa	2018 Sep 21	E1-W2-W1-S2-S1-E2	H-PRISM	HD 25490, HD 50281	(4)
Caph	2018 Sep 22	E1-W2-W1-S2-E2	H-PRISM	ζ Cas, θ Cas	(5)
Cursa	2018 Sep 22	E1-W2-W1-S2-S1-E2	H-PRISM	HD 22713, HD 33256, HD 50281	(4)
–	2018 Oct 03				(2,6)
–	2018 Oct 04				(2,6)
–	2018 Oct 05				(2,7)
Caph	2018 Nov 03	E1-W2-W1-S1-E2	H-PRISM	7 And	(7)
Caph	2018 Nov 04	E1-W2-W1-S1-E2	H-PRISM	7 And, ζ Cas	(7)
Alderamin	2018 Nov 04	E1-W2-W1-E2	H-PRISM	HD 210855, 16 Cep	(7)
Cursa	2018 Nov 04	E1-W2-W1-S1-E2	H-PRISM	HD 25621, HD 33256	(7)
28 Mon	2018 Nov 04	E1-W2-W1-S1-E2	H-PRISM	HD 55185, HD 77250	(7)
Caph	2018 Nov 05	E1-W2-W1-S1-E2	H-PRISM	7 And, ζ Cas	(7)
Alderamin	2018 Nov 05	E1-W2-W1-E2	H-PRISM	HD 210855, 16 Cep	(7)
Cursa	2018 Nov 05	E1-W2-W1-S1-E2	H-PRISM	HD 33256	(7)

Table A.1 (cont'd)

Object	UT date	Baselines	Mode	Calibrators	Notes
Alderamin	2018 Nov 06[a]	E1-W2-W1-E2	H-PRISM	HD 210855, 16 Cep	(5)
Cursa	2018 Nov 06[a]	E1-W2-W1-S1-E2	H-PRISM	HD 25621, HD 33256	
28 Mon	2018 Nov 06[a]	E1-W2-W1-S1-E2	H-PRISM	HD 55185, HD 77250	
Caph	2018 Nov 07[a]	E1-W2-W1-S1-E2	H-PRISM	7 And, ζ Cas, θ Cas	
Alderamin	2018 Nov 07[a]	E1-W2-W1-E2	H-PRISM	HD 210855, 16 Cep	
Cursa	2018 Nov 07[a]	E1-W2-W1-S1-E2	H-PRISM	HD 25621, HD 33256	
28 Mon	2018 Nov 07[a]	E1-W2-W1-S1-E2	H-PRISM	HD 55185, HD 77250	
Zosma	2019 Apr 02	E1-W2-W1-S2-S1-E2	H-GRISM	HD 97633	(7,8)
–	2019 Apr 03				(2,7)
–	2019 Apr 04				(2,7)
–	2019 Apr 05				(2,6,7)
–	2019 Apr 06				(2,6,7)
–	2019 May 16				(6,7)
–	2019 May 17				(6,7)
Altair	2019 May 18	E1-W2-W1-S2-S1	H-GRISM	31 Aql, HD 194937	(2,3)
–	2019 May 19				(6,7)
–	2019 May 20				(2,6,7)
–	2019 May 21				(2,7)
–	2019 May 22				(2,3)
Caph	2019 Aug 09	E1-W2-W1-S2-S1-E2	H-GRISM	7 And, ζ Cas, θ Cas	
Alderamin	2019 Aug 09	E1-W2-W1-E2	H-GRISM	16 Cep	
Altair	2019 Aug 10	E1-W2-W1-S2-S1-E2	H-GRISM	31 Aql, HD 185018	(5)
Alderamin	2019 Aug 10	E1-W2-W1-S2-E2	H-GRISM	HD 195820, 16 Cep, HD 210855	
Caph	2019 Aug 10	E1-W2-W1-S2-E2	H-GRISM	ζ Cas, θ Cas	
Altair	2019 Aug 11	E1-W2-W1-S2-S1-E2	H-GRISM	31 Aql, HD 185018, HD 194937	
Alderamin	2019 Aug 11	E1-W2-W1-S2-E2	H-GRISM	16 Cep, HD 210855	
Caph	2019 Aug 11	E1-W2-W1-S2-S1-E2	H-GRISM	7 And, ζ Cas, θ Cas	
Caph	2019 Aug 12	E1-W2-W1-S2-S1-E2	H-GRISM	7 And, ζ Cas	
Alderamin	2019 Aug 12	E1-W2-W1-E2	H-GRISM	16 Cep, HD 210855	
–	2019 Nov 17				(3)
28 Mon	2019 Nov 19	E1-W2-W1-S2-E2	H-GRISM	HD 55185, HD 77250	
–	2020 Mar 11				(6,7)
–	2020 Mar 12				(2)

Table A.1 (cont'd)

Object	UT date	Baselines	Mode	Calibrators	Notes
–	2020 Mar 14				(6,7)
–	2020 Mar 15				(6,7)
–	2020 Mar 16				(6,7)
–	2020 Mar 17				(6,7,8)
–	2020 Mar 18				(8)
–	2020 Mar 19				(8)
–	2020 May 01				(9)
–	2020 May 02				(9)
–	2020 May 03				(9)
–	2020 Jun 01				(7)
Vega	2020 Jun 02	E1-W2-W1-E2	H-GRISM	HD 168322, HD 167304, HD 182694	(7)
–	2020 Jun 07				(2,3)
–	2020 Jun 08				(3)
Alderamin	2020 Aug 02	E1-W2-W1-S2-E2	H-GRISM	HD 195820, 16 Cep, HD 210855	
Caph	2020 Aug 02	E1-W2-W1-S2-S1-E2	H-GRISM	7 And, ζ Cas, θ Cas	
–	2020 Aug 03				(10)
Alderamin	2020 Aug 04	E1-W2-W1-S2-E2	H-GRISM	ι Cyg, HD 195820, 16 Cep	(10)
Caph	2020 Aug 04	E1-W2-W1-S2-S1-E2	H-GRISM	7 And, ζ Cas, θ Cas	(10)
Vega	2020 Aug 05	E1-W2-W1-S2-S1-E2	H-GRISM	HD 168322, HD 182694	
Caph	2020 Aug 05	E1-W2-W1-S2-S1-E2	H-GRISM	7 And, ζ Cas, θ Cas	
Vega	2020 Aug 06	E1-W2-W1-S2-S1-E2	H-GRISM	HD 168322, HD 182694	
Caph	2020 Aug 06	E1-W2-W1-S2-S1-E2	H-GRISM	7 And, ζ Cas, θ Cas	(4)
–	2020 Sep 08				(1)
–	2020 Sep 09				(1)
–	2020 Sep 10				(1)

[a]This time was given in addition to the scheduled observing time during CHARA observing engineering time.

Note. — We note that observations were hindered by the following: (1) forest fires near the CHARA Array; (2) high humidity; (3) high winds (jet stream); (4) poor seeing of $r_0 \leq 7$ cm; (5) tech issues with MIRC-X; (6) rain; (7) clouds; (8) snow/hail; (9) a global pandemic; and (10) ash/winds. The PRISM mode used in our observations has a spectral resolution of R = 50 while the GRISM mode has a spectral resolution of R = 190. The baselines are listed in their respective beam order for each observing night.

Appendix B
EXTRA IMAGES AND PLOTS

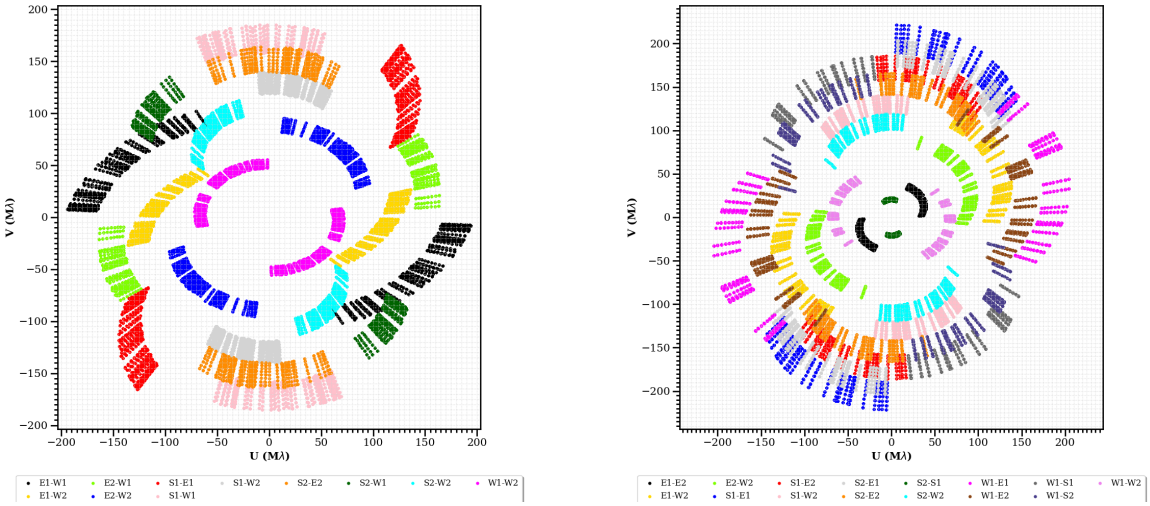

Figure B.1 We show the (u, v) coverage for both λ And epochs (in 2010 and 2011). The plot on the left shows the 2010 epoch with 4T observations and the plot on the right shows the 2011 epoch using a 6T arrangement.

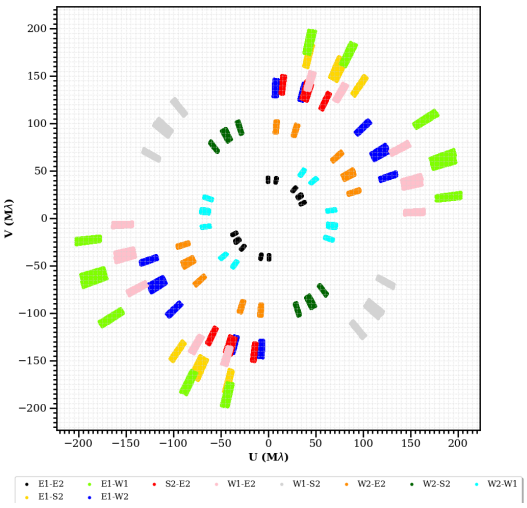

Figure B.2 We show the (u, v) coverage for Alderamin for the 2019 epoch using a 5T arrangement.

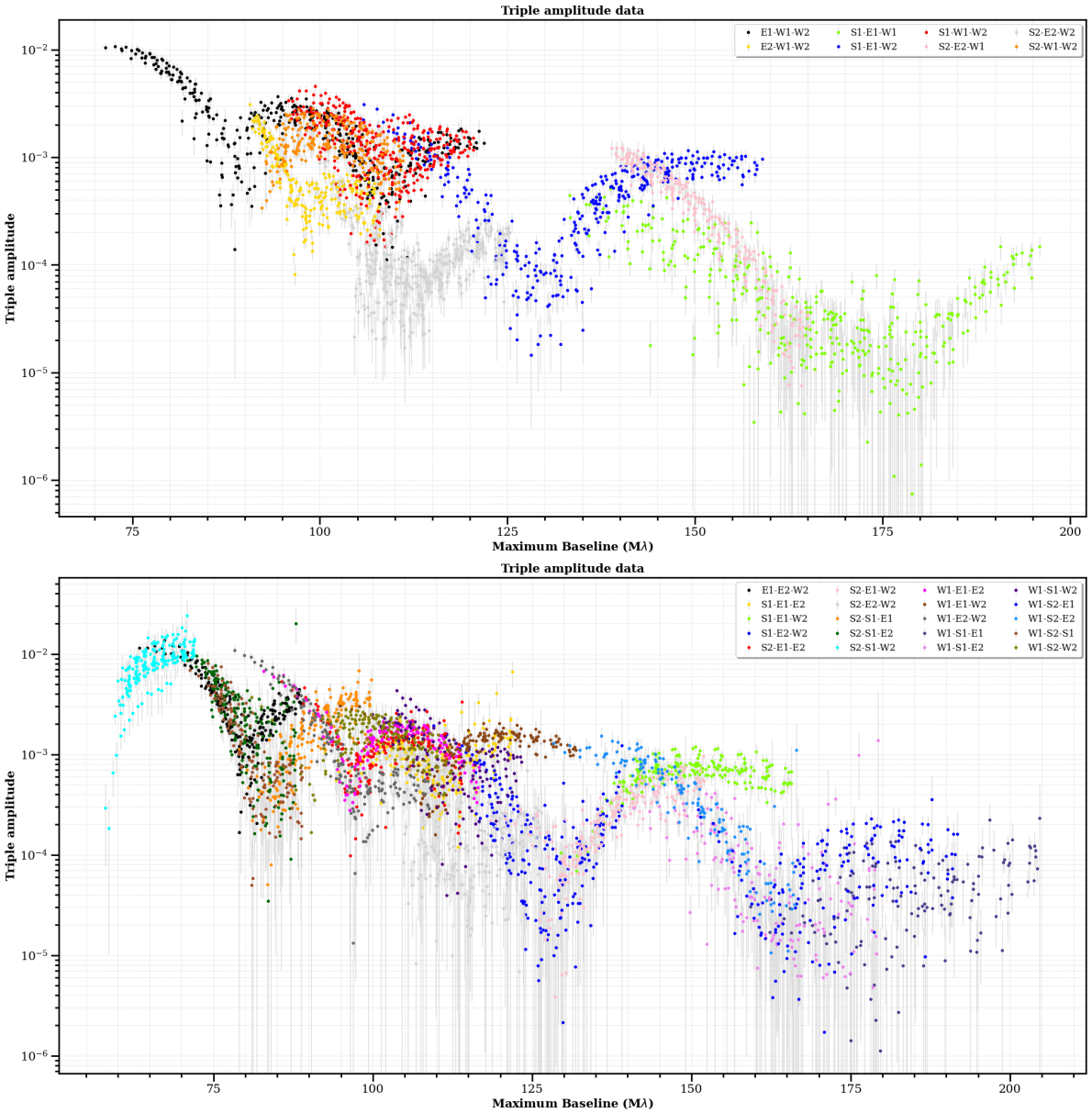

Figure B.3 We show the triple amplitudes for both λ And epochs (in 2010 and 2011). The plot on the top shows the 2010 epoch with 4T observations and the plot on the bottom shows the 2011 epoch using a 6T arrangement.

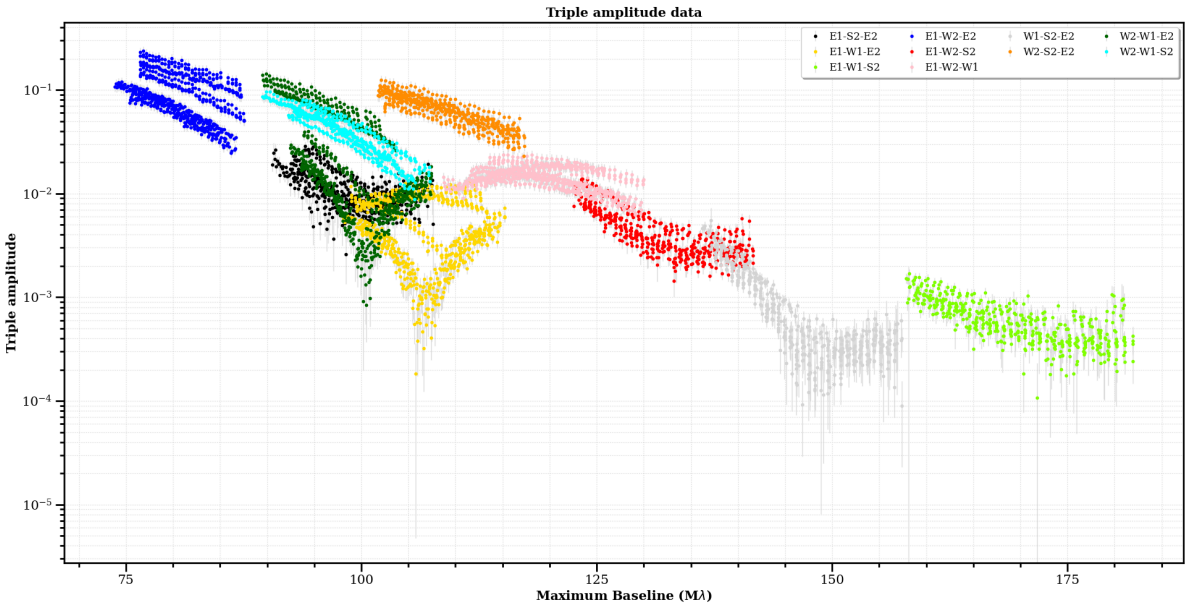

Figure B.4 We show the triple amplitudes of the Alderamin data taken in 2019 using a 5T arrangement.

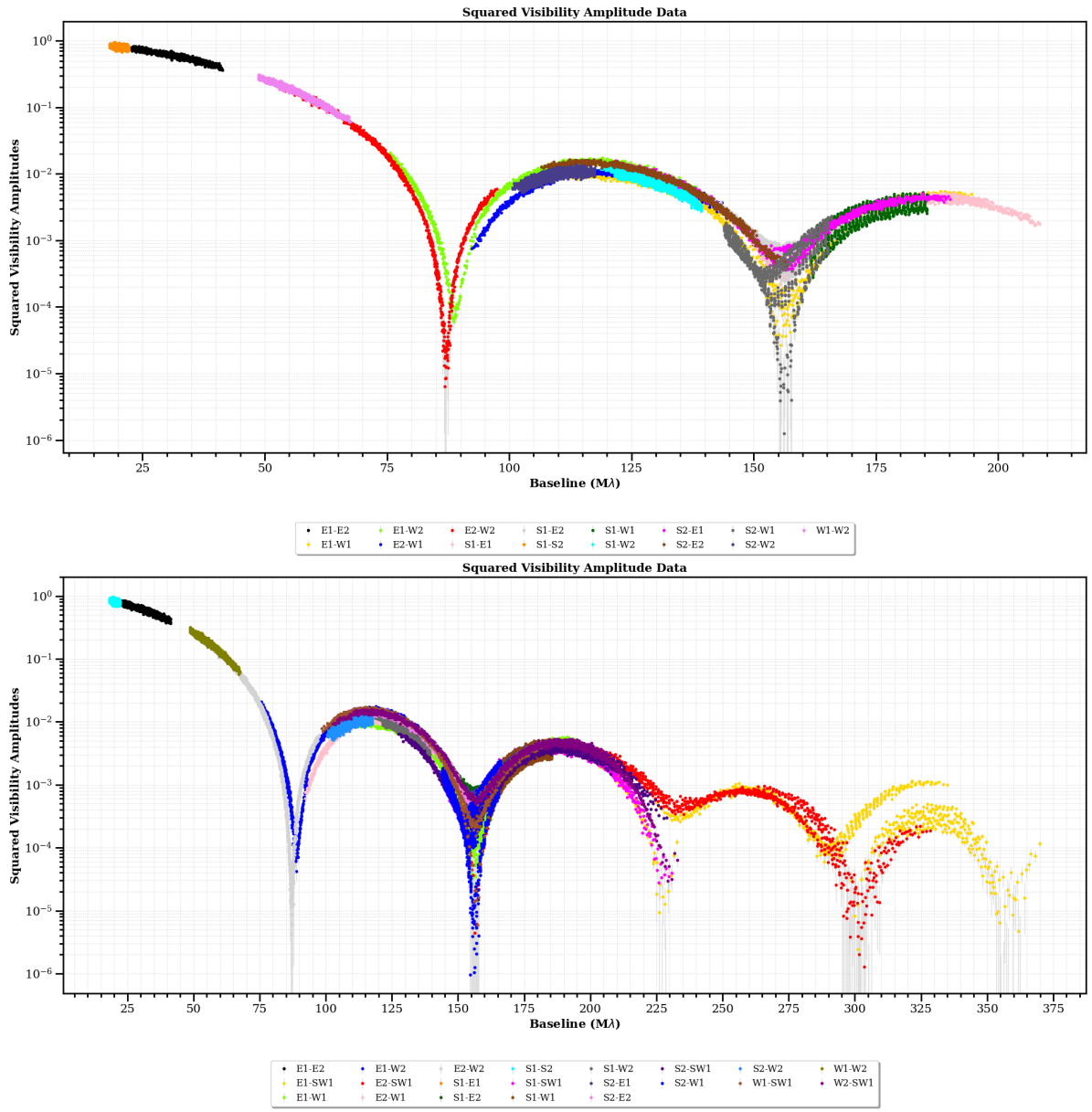

Figure B.5 Top: The squared visibilities of a simulated spotted star with CHARA's current 6T configuration. Bottom: The squared visibilies of a simulated spotted star with a potential active movable 7th telescope added to the current CHARA 6T configuration.

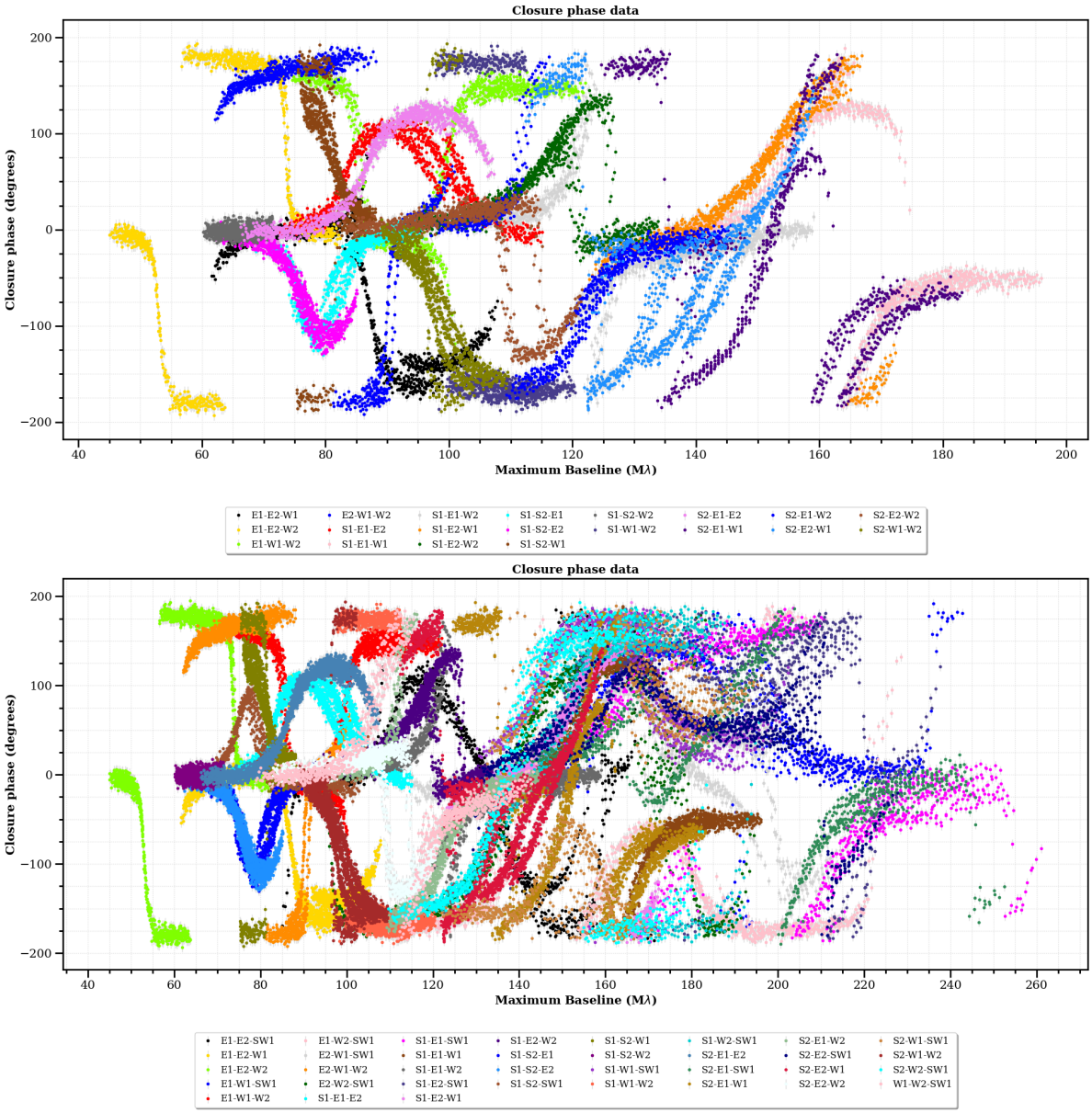

Figure B.6 Top: The closure phases of a simulated spotted star with CHARA's current 6T configuration. Bottom: The closure phases of a simulated spotted star with a potential active movable 7th telescope added to the current CHARA 6T configuration.